Mineral stability and porosity dynamics in Halite- and Kainite-bearing rocks after hydrogen batch reaction test: a case study of Realmonte mine, Sicily (Italy)

Anzelmo, G.[*1], Rossi, M.[1], Colella, A.[1], Edlmann, K.[2], Kilpatrick, A.[2], Maniscalco, R.[3], Pellegrino, A.G.[3], Rizzi, R.[4], Cella, G.M.[5], Visconti, L.[5], Di Benedetto, C.[1], Portarapillo, M.[6], Di Benedetto, A.[6] & Iacopini, D [1].

Affiliations: [1] *Dept. of Earth, Environmental and Resources Sciences of the University of Naples Federico II (Italy)*

[2] *School of Geosciences, University of Edinburgh, Grant Institute (Scotland)*

[3] *Dept. of Biological, Geological and Environmental Sciences of the University of Catania (Italy)*

[4] *Institute of Crystallography, Consiglio Nazionale delle Ricerche, Bari (Italy).*

[5] *ENI S.p.A, San Donato Milanese (Italy)*

[6] *Dept. of Chem. Engineering, Materials and Industrial Production, University of Naples Federico II (Italy)*

*Corresponding author. E-mail address: giuseppa.anzelmo@unina.it

Keywords: Underground hydrogen storage; Energy Storage, Salt Caverns, Salt Mine; Kainite; Evaporites; Pore network; Permeability.

Abstract

Underground hydrogen storage in salt caverns is among the most mature geological storage options, yet the behaviour of potash-salt lithologies under hydrogen exposure remains entirely uncharacterised. This study presents a multi-technique characterisation, performed on selected representative samples, of Messinian halite and kainite-bearing evaporites from the Realmonte mine (Sicily) subjected to static hydrogen exposure (10 MPa H_2, 120 h) and to cyclic loading under constant hydrogen pressure (0.789 MPa) with confining stress cycled between 3.8 and 19.2 MPa, at room temperature. Samples were analysed before and after H_2 exposure using X-ray powder diffraction, whole-rock and trace-element geochemistry, optical and scanning electron microscopy, laboratory and synchrotron micro-CT, mercury intrusion porosimetry and PHREEQC thermodynamic modelling. No mineralogical reactions or neoformation of phases were detected in either halite or kainite, but localised microstructural reorganisation, including dissolution-reprecipitation of halite and kainite, brine migration, and pore-size redistribution, is observed in post-exposure samples. These results extend to a hydrated sulphate-chloride double salt the geochemical-stability evidence previously documented for Zechstein, Lotsberg, and Eocene halites. Micro-CT three-dimensional imaging reveals that pore architecture is governed by mineralogical heterogeneity: pure halite hosts a connected grain-boundary fracture network ($\varphi\_CT = 2.13\%$) and the kainite-halite assemblage hosts a nanometre-scale grain-boundary pore system ($\varphi\_CT = 0.106\%$; MIP modal diameter 5.5 nm). Post-exposure MIP data show systematic pore-size redistribution driven by brine migration and grain-

boundary rearrangement without significant changes in bulk porosity. Cyclic hydrogen injection tests on an impure halite-kainite sample yield permeabilities of $K = 3.48 \times 10^{-21}$ m^2 (seasonal cycling) and $K = 2.46 \times 10^{-20}$ m^2 (monthly cycling) within or slightly above the range reported for intact rock salt and three to four orders of magnitude below tightness thresholds proposed for gas-storage caverns. These results provide the first experimental evidence that hydrogen acts as a physical stress agent rather than a chemical reactant, suggesting a similar behaviour to pure halite evaporites.

1. Introduction

The large-scale deployment of hydrogen as an energy vector requires subsurface storage systems capable of buffering the intermittency of renewable electricity generation. Among the geological options under consideration, salt caverns are the most technically mature (TRL 7-8), with over five decades of operational experience at facilities in Texas (Clemens Dome, Moss Bluff, Spindletop) and Teesside, UK (Crotogino et al., 2018; Tarkowski, 2019). A new generation of projects, Bad Lauchstädt (Germany), HyStock (Netherlands), HyPSTER (France), ACES Delta (Utah), are now advancing toward green-hydrogen commissioning (Tackie-Otoo and Haq, 2024). Rock salt offers exceptionally low matrix permeability (10^{-23} to 10^{-21} m²), self-healing of microfractures through viscoplastic creep, low cushion-gas requirements and rapid cycling capacity (Bérest and Brouard, 2003; Heinemann et al., 2021).

Recent experimental work consistently demonstrates that halite is geochemically inert under hydrogen exposure. Fatah et al. (2024), Kovács et al. (2025) and Emmel et al. (2025) exposed halite ± anhydrite to H_2 at pressures of 10-250 bar and temperatures of 60-75 °C without detecting mineralogical alteration, while Yuan et al. (2025a, b) confirmed that non-reductive dissolution dominates in impure salt with predicted H_2 loss below 0.1 % over two years. Nassan et al. (2025) measured H_2 permeability of rock salt at approximately 10^{-23} m², confirming near-impermeable behaviour. On the transport side, AbuAisha and Billiotte (2021) provided a comprehensive analysis of hydrogen migration mechanisms in saturated rock salt (viscous flow, diffusion and dissolution) demonstrating that cumulative H_2 losses by diffusion are negligible even under conservative assumptions. On the geomechanical side, Grgic et al. (2022) showed that competing viscoplastic and microcracking mechanisms effectively prevent net permeability evolution under cyclic loading, and Wang et al. (2022) tracked progressive pore damage during fatigue tests using NMR. However, these studies focus almost exclusively on halite-dominated lithologies, despite the fact that many evaporite successions contain significant proportions of potash-bearing salts. In natural evaporite sequences, halite commonly occurs interbedded with potassium-magnesium evaporites such as carnallite, sylvite, polyhalite and kieserite, particularly within the upper stages of marine evaporitic cycles.

K-Mg salts (carnallite, sylvite, polyhalite, kieserite and kainite), which occur as interbeds or discrete layers in many evaporitic successions worldwide, including the Permian Zechstein of the North Sea and East Yorkshire (e.g. Fordon Evaporite at Aldborough and Atwick, Kemp et al., 2016; Pichat et al., 2025;), the Devonian Prairie Evaporite of western Canada (Wardlaw, 1968), the Permian Salado Formation of the Delaware Basin (Lowenstein, 1988), the Cretaceous Maha Sarakham Formation of Thailand and Laos (El Tabakh et al., 1999), the Aptian evaporites of the South Atlantic (Szatmari et al., 2021), and the Ediacaran-Cambrian Hormuz Formation of Iran (Talbot et al., 2009), differ fundamentally from halite in crystal structure, hydration state, solubility and mechanical behaviour,

suggesting that their response to hydrogen exposure cannot be assumed to follow the same geochemical and transport behavior observed in halite. Martin-Clave et al. (2021) demonstrated that high second-phase content (up to 55%, predominantly anhydrite and polyhalite) weakens rock salt and generates new porosity around accessory mineral crystals under cyclic loading; Luangthip et al. (2017) showed that compressive strength decreases exponentially with increasing carnallite content. A particularly notable gap concerns kainite ($KMg(SO_4)Cl \cdot 2.75H_2O$), a hydrated potassium-magnesium sulphate-chloride double salt that occurs in late-stage evaporitic assemblages and in potash-bearing salt sequences. Unlike halite, kainite possesses a monoclinic crystal structure and incorporates structural water, giving it markedly different thermal stability and dehydration behaviour (Borisov et al., 2022) precluding extrapolation from halite. The only mention of kainite in a H_2 context is the prediction by Emmel et al. (2025) that it may precipitate from polyhalite dissolution, but no experimental verification of its response to H_2 exposure has been attempted.

The Realmonte salt mine (Agrigento, Sicily) exposes the Messinian evaporitic sequence of the Caltanissetta Basin, comprising about 300 m of folded halite-dominated layers, including nearly pure and pure halite intervals (>99%) alternating with kainite-bearing layers up to 18 m thick, accompanied by accessory anhydrite, carnallite, leonite and polyhalite (Decima and Wezel, 1971; Lugli et al., 1999; Butler et al., 2014; Yoshimura et al., 2016). Speranza et al. (2019) characterised the petrophysical properties of Realmonte halite but explicitly excluded kainite layers. The co-occurrence of halite-dominated and volumetrically significant kainite interbeds within a single, well-exposed mine section makes Realmonte an ideal natural laboratory for evaluating mixed evaporitic lithologies under hydrogen exposure. The present study adopts a comparative design focusing on two evaporitic end-members, in which halite-dominated samples serve as the reference and kainite-bearing samples represent the compositionally complex, previously untested counterpart. Halite geochemical inertness to hydrogen has now been demonstrated across Zechstein, Lotsberg and Eocene formations (Fatah et al., 2024; Kovács et al., 2025; Emmel et al., 2025; Yuan et al., 2025), and its pore-network and transport properties under storage conditions are increasingly well constrained. By contrast, no equivalent dataset exists for the Messinian evaporitic units, and specifically data for kainite or for any other K-Mg salt are absent from the literature. Framing the halite samples as a well-documented baseline against which the kainite-bearing assemblage can be evaluated allows the study to isolate specific effects of mineralogical heterogeneity on pore architecture, geochemical stability and transport behaviour.

Therefore, three specific knowledge gaps motivate the present study: (i) no experimental data exist on the geochemical interaction between molecular hydrogen and kainite-bearing evaporites; (ii) the pore architecture and transport properties of kainite-halite assemblages have never been characterised at any scale by imaging or porosimetric techniques; and (iii) the permeability response of Messinian heterogeneous potash-salt formations to cyclic pressure loading has not been attempted. This study provides the first experimental dataset on a kainite-halite sample under H_2 exposure, comparing its response to that of halite-dominated samples from the same Messinian succession. The aim is to identify whether first-order differences exist in geochemical stability and pore-network response, while quantifying pore-network architecture and its modification upon hydrogen exposure and measuring permeability under cyclic injection conditions. The comparison is designed to flag mineralogically driven contrasts and to provide the first integrated baseline for kainite-bearing evaporites, against which future studies can characterise variability across the lithology.

2. Materials and Methods

The samples are from the Messinian salt succession at Realmonte which is characterised by pronounced lithological heterogeneity arising from variations in depositional environment, brine chemistry, and syn- to post-sedimentary processes. Typical sequences comprise intercalated halite, sulphates and potassium-magnesium salts arranged in complex cyclic patterns (Decima and Wezel, 1971; Schreiber and Hsü, 1980; Lugli et al., 1999; Roveri et al., 2008). Accessory phases, including anhydrite ($CaSO_4$), celestine ($SrSO_4$), polyhalite ($K_2Ca_2Mg(SO_4)_4 \cdot 2(H_2O)$), clay minerals. In specific horizons, carnallite ($KMgCl_3 \cdot 6(H_2O)$) and leonite ($K_2Mg(SO_4)_2 \cdot 4(H_2O)$), may occur as irregular lenses, microscopic aggregates or dispersed inclusions, resulting in substantial mineralogical variability even within a single stratigraphic level (Lugli et al., 2002; Schreiber and Lugli, 2019). The sampling strategy was designed to achieve representative lithological coverage of the mine's accessible extent, both vertically (from approximately -55 to -200 m relative to sea level) and laterally across four mine galleries at different stratigraphic levels (Fig. 1). In each gallery, at each sampling station, multiple cores were collected from the different salt compositions present at that location, to capture local compositional variability. This approach generated an inventory from which the subset analysed in this study was selected, focusing on halite-dominated and kainite-bearing end-members. The mine is excavated entirely within the upper portion of the Messinian salt succession, specifically within Unit C (halite-dominated) and the uppermost part of Unit B (containing the kainite-bearing horizons), as defined by Yoshimura et al. (2016) and Lugli et al. (1999). Sampling within Unit C targeted nearly pure halite and was then extended to the kainite mining area at approximately -170 m, where the kainite lens at the top of Unit B was sampled both within the kainite-dominated composition and at the halite-kainite transition zone (Fig. 1).

From this inventory, sixteen evaporitic cores were selected for the present study, comprising eleven halite-dominated cores (RS series: RS1, RS2, RS3, RS4, RS10, RS12, RS13, RS14, RS15, RS17, RS18; see Table 1 for the analytical matrix), of which seven have NaCl content ≥ 95 wt%, a compositional threshold conventionally adopted in operational and geomechanical assessments of rock salt suitability for underground gas storage (Caglayan et al., 2020; Cyran, 2021), including two (RS10, RS14) that reach pure-halite composition (>99 wt% NaCl), and five kainite-bearing rocks (KS series: KS1, KS2, KS3, KS4, KS5). Most cores were extracted directly from the mine walls using a portable drill cooled by water, coring device equipped with a 25 mm diameter drill bit; saturated NaCl brine (~26%) collected from the mine workings was employed as cutting fluid to minimise mechanical damage and fracture propagation. Sample KS5, intended for the high-pressure hydrogen injection test, was cored at 35 mm diameter from a block collected in the mine and subsequently shaped into a cylinder of 35 mm × 40 mm. Following extraction, cores were surface-dried with absorbent paper in the mine and placed in sample bags together with silica gel desiccant sachets. Once outside the mine, the desiccant sachets were replaced with fresh ones and left in contact with the cores for approximately 24 hours to remove residual moisture. The cores were then wrapped in a double layer of plastic film and an outer layer of aluminium foil, after which the desiccant was removed and samples were stored in sealed laboratory bags at approximately 18 °C, consistent with in situ mine conditions, to prevent thermal fluctuations and potential phase changes prior to laboratory analysis. Powder sub-samples were obtained by cutting each core along a central cross-section, providing statistically representative material while preserving the remaining core length for subsequent thin-section preparation and batch experiments.

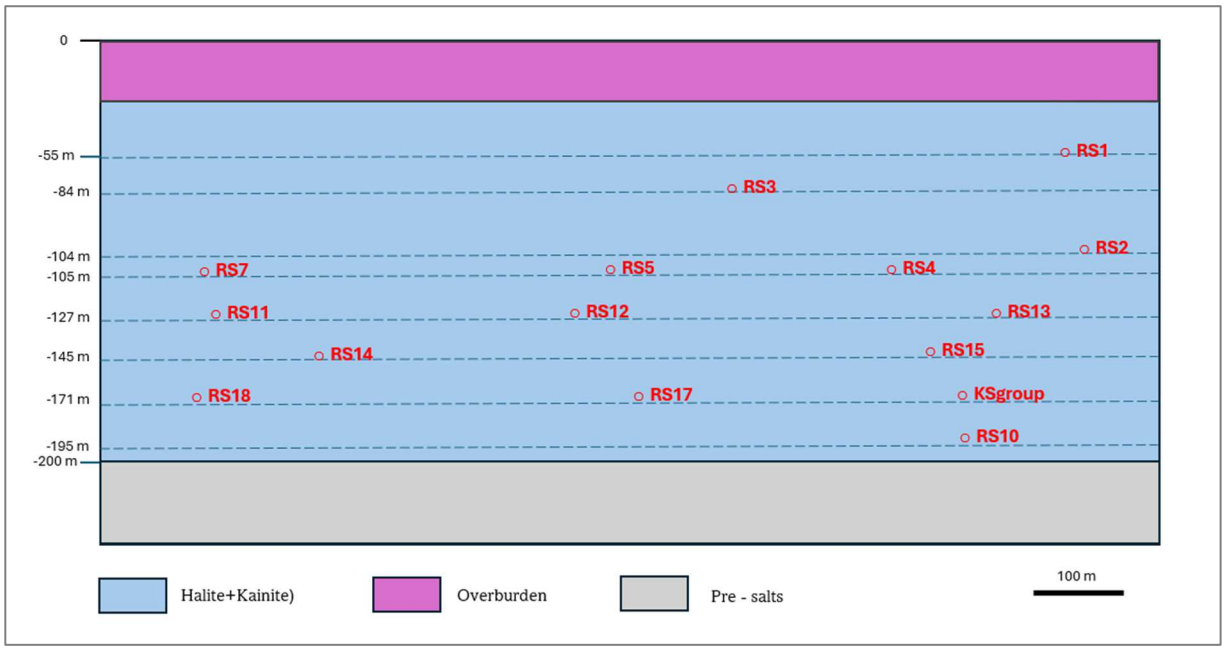

Fig.1 Simplified vertical section of the Realmonte mine halite-kainite succession showing sampling locations and depths (-55 to -200 m a.s.l.). RS = rock salt series; KS = kainite series (KS2-KS3-KS5). The simplified vertical section deformation is not considered. Dashed lines represent depth, not stratigraphic interval.

The samples underwent a comprehensive analytical workflow (Fig. 2; Table 1) consisting of four main stages: (i) sample preparation (25 mm-diameter cores, a single 35 mm-diameter core for the injection test, bulk-rock powders and thin sections); (ii) preliminary characterisation of halite and kainite lithologies; (iii) exposure to hydrogen through cyclic high-pressure injection and static batch tests; and (iv) post-exposure analyses to assess any changes occurred. Pre- and post-exposure characterisation was carried out through a holistic approach combining the geochemistry of bulk solid phase with chemical and minero- petrographical investigations, porosity analyses, advanced X-ray imaging techniques, supplemented by PHREEQC thermodynamic modelling. Table 1 summarises sample labels and the analytical techniques applied to each.

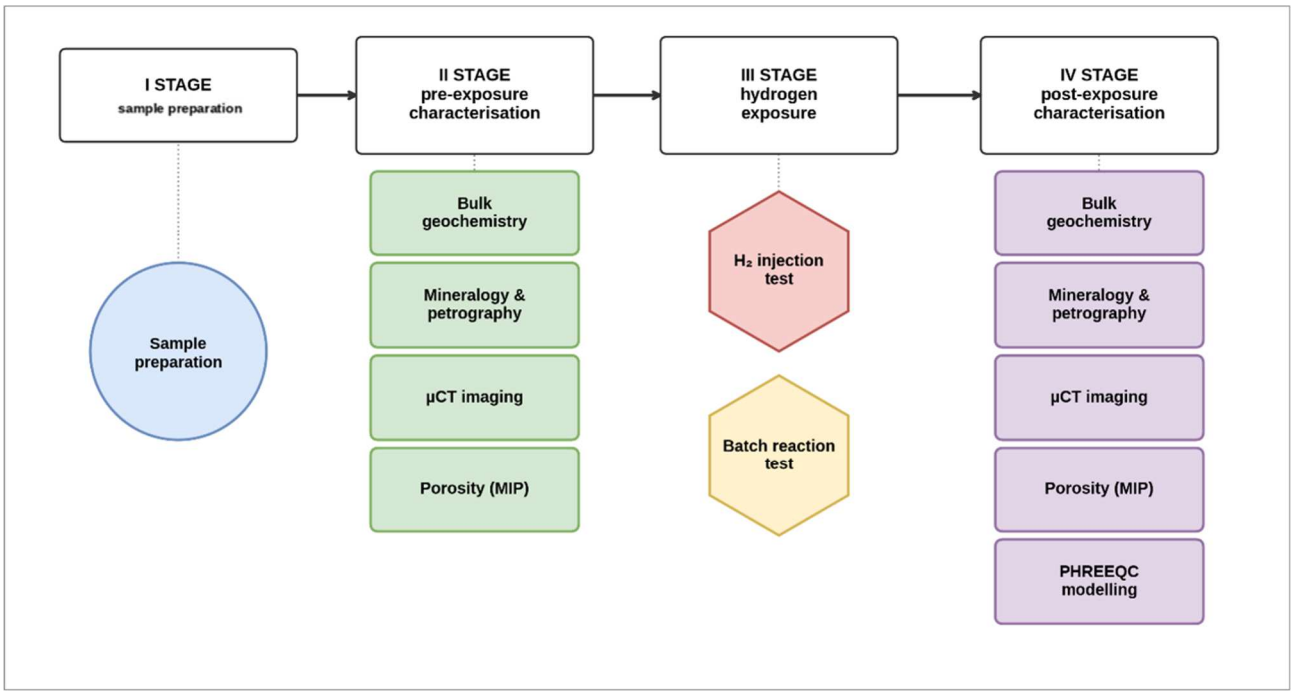

Fig. 2. Experimental and analytical workflow. Stage I: sample preparation; Stage II: pre-exposure characterisation; Stage III: hydrogen exposure (cyclic injection + static batch); Stage IV: post-exposure characterisation.

Table 1. Analytical techniques applied to each sample collected. Batch and cyclic injection samples are listed separately. OM = optical microscopy; SEM-EDS = scanning electron microscopy with energy-dispersive spectroscopy; XRPD = X-ray powder diffraction; Geochem. = bulk geochemistry (ICP-OES, INAA, ICP-MS, XRF); µCT = micro-computed tomography; MIP = mercury intrusion porosimetry. Mineral proportions for each sample are reported in Table 3.

Sample	OM	SEM-EDS	XRPD	Geochem.	µCT	MIP	Batch	Cyclic inj.
RS1	×	×	×	×	×	×		
RS2					×	×		
RS3	×			×		×		
RS3_batch	×		×	×		×	×	
RS4	×	×	×	×	×	×		
RS4_batch	×		×	×		×	×	
RS10	×	×	×	×	×	×		
RS11				×	×	×		
RS12				×		×		
RS13					×	×		
RS14	×	×	×	×		×		
RS15				×		×		
RS17						×		
RS18	×					×		
KS1						×		
KS2	×					×		
KS3	×					×		
KS4						×		
KS5	×	×	×	×		×		
KS5_batch	×		×	×	×	×	×	×

2.1. High-pressure hydrogen exposure

Two complementary experiments were conducted to assess the response of the Realmonte evaporites to hydrogen under storage-relevant conditions: (a) a cyclic high-pressure injection test simulating dynamic cavern operation, and (b) a static batch test isolating intrinsic gas-rock chemical reactivity under prolonged exposure.

2.1a. Cyclic hydrogen injection test. A dynamic hydrogen injection experiment was conducted at the Grant Institute, University of Edinburgh, using a custom-built vertical high-pressure flow cell (volume 1000 ml; Edlmann et al., 2016). The apparatus comprises a Hassler-type pressure vessel with a rubber sleeve isolating the specimen from the oil phase delivering a radial confining pressure, top and bottom steel pistons serving as end-caps, pressure sensors for continuous monitoring of both the differential hydrogen pressure across the sample and the confining pressures, with hydrogen flow delivered through a regulated high-pressure hydrogen cylinder as gas supply. Sample KS5 (35 mm diameter × 40 mm height; $A = 9.621 \times 10^{-4}$ m², $V = 3.85 \times 10^{-5}$ m³) was positioned between the two pistons with its lateral surface wrapped in insulating tape and aluminium foil to ensure gas tightness, while the upper and lower faces remained exposed to hydrogen flow (Fig. 3a-e). Confining pressures were derived from geostatic conditions estimated from the 3D geological model of the Realmonte site and conservatively reduced by 20%. The cycling protocols were designed to apply the pressure

variation to the confining stress (P_1/P_2) rather than to the hydrogen pressure, in order to reproduce the stress regime experienced by the cavern walls during real storage operations: injection raises the internal cavern pressure and increases the radial stress on the walls, while withdrawal lowers it, generating a cyclic stress field on the wall rock. Hydrogen pressure was maintained at a low constant value (~ 0.789 MPa, well within the ideal-gas regime, Z ~ 1.00) throughout the test, in order to (i) probe gas penetration through the matrix under conditions in which non-ideal compressibility corrections to permeability and diffusivity are negligible, and (ii) establish a conservative baseline for a mineralogically complex, previously uncharacterised kainite-halite assemblage, allowing detection of even minor changes in transport behaviour before higher-pressure testing in future studies.

Three protocols were applied in sequence:

(i) Seasonal-cycle simulation: 1 cycle of 4 hours, comprising 2 h loading at P_confining = 19.2 MPa followed by 2 h unloading to 3.8 MPa. Hydrogen pressure P_{H_2} ~7.89 bar; upstream-downstream pressure difference ΔP = 0.22 bar; T~ 20 °C.

(ii) Monthly-cycle simulation: 12 cycles of 34 minutes each, comprising 17 min at 19 MPa under hydrogen injection and 17 min at 3.8 MPa without injection. Same P_{H_2} and ΔP as above (Fig. 3g).

(iii) Constant-pressure baseline: 2 h at steady-state pressure, providing a reference measurement for subsequent permeability estimation.

Hydrogen was maintained at approximately 7.89 bar during all loading phases; no gas was injected during unloading. Temperature was at approximately 20 °C throughout (Fig. 3f). No relaxation phases were included between cycles, resulting in higher mechanical and chemical stresses than those expected in operational caverns and thus providing a conservative assessment of system behaviour.

Permeability estimation. Apparent permeability was derived from the transient downstream pressure decay using a pulse-decay approach. (Edlmann et al., 2016), since the theoretical volumetric flow rate Q is of the order of 10^{-13}-10^{-12} m^3/s (≤0.2 picolitres/s), well below the detection limit of conventional flow meters. The Darcy law for compressible gas flow was applied:

$$K = \frac{Q \cdot \mu \cdot L}{A \cdot \Delta P}$$

where Q is the estimated volumetric flow ($m^3\ s^{-1}$), μ the dynamic viscosity of hydrogen at 20 °C (8.80×10^{-6} Pa·s), L the sample height (0.040 m), A the cross-sectional area (9.621×10^{-4} m^2), and ΔP the upstream–downstream pressure difference (0.22 bar = 2.2×10^4 Pa). Apparent permeability values were subsequently corrected for gas slippage effects using the Klinkenberg correction to obtain intrinsic permeability K_∞, following established protocols for low-permeability evaporitic rocks (Grgic et al., 2022; Nassan et al., 2025).

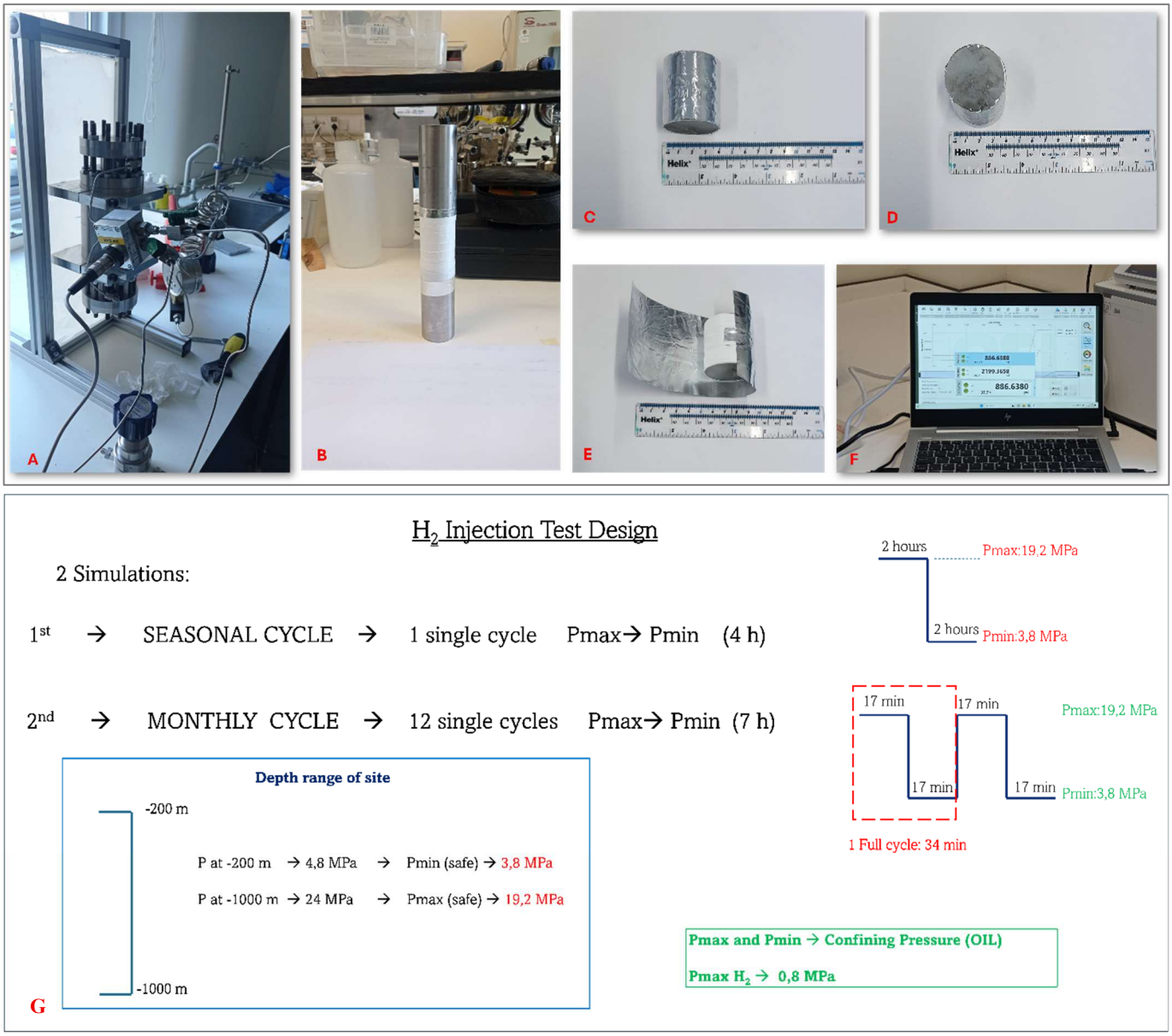

Fig. 3. Cyclic hydrogen injection test. (a) High-pressure autoclave apparatus at the Grant Institute, University of Edinburgh; (b) sample KS5 positioned inside the liner between two steel pistons; (c–e) sample preparation and dimensions (35 mm × 40 mm); (f) monitoring of physical parameters: confining pressure (P_max, P_min), hydrogen pressure (P_H₂) and temperature (T) during the three test protocols (seasonal cycle, monthly cycles, constant-pressure baseline); (g) injection test design.

2.1b. Static batch test. Static batch test. A complementary static experiment was conducted at the SaRAH Lab, Department of Chemical, Materials and Production Engineering, University of Naples Federico II, using a 1 L stainless steel autoclave. The reactor was sealed and flushed with nitrogen to displace atmospheric gases (O_2, CO_2 and water vapour) from the vessel, ensuring that the samples were exposed to a hydrogen-only atmosphere. The autoclave was subsequently pressurised with ultra-high-purity hydrogen (99.999%) to 10 MPa using a gas-feeding system that controlled purge and outflow conditions to remain below the lower flammability limit (LFL). The temperature was maintained at approximately 20 °C for a total duration of 120 hours (five days). Neither brine nor confining pressure was applied; the static configuration minimises mechanically induced effects and isolates intrinsic gas-rock reactivity from pressure- and flow-induced processes, simulating prolonged

gas exposure at the cavern wall under static conditions. The two halite-dominated cores (RS3, RS4; 25 mm diameter) and the kainite-bearing core (KS5; 35 mm diameter, previously subjected to the cyclic injection test), all designated 'batch' in Table 1, were positioned within the vessel with approximately 5 cm spacing to prevent physical contact (Fig. 4).

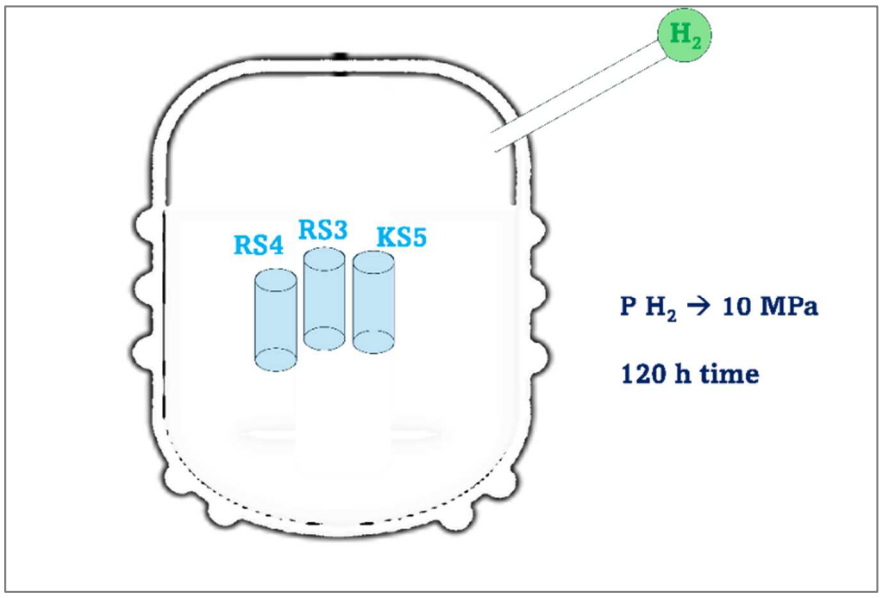

Fig. 4. Static batch test apparatus (University of Naples Federico II). The 1 L stainless steel autoclave was charged with H_2 at 10 MPa and 20 °C for 120 h. Samples were spaced ~5 cm apart within the reactor vessel.

The static configuration was specifically designed to isolate intrinsic gas-rock reactivity from pressure- or flow-induced effects, by removing confining stress and bulk fluid flow from the experimental variables. Although operational caverns are de-brined after solution mining, a residual sump brine, typically 10^3-10^4 m^3, remains at the cavern base and contacts a fraction of the cavern wall (Crotogino et al., 2018); under operational conditions, both unsaturated and brine-saturated wall-rock domains coexist. The present batch experiment represents the chemistry of the unsaturated wall-rock fraction; the chemistry of brine-saturated domains is addressed indirectly through the PHREEQC modelling of halite-kainite-brine-H_2 systems (Section 2.5).

2.2. Mineralogical-petrographic and textural characterisation

Mineralogical, petrographic and textural analyses were performed on pre- and post-exposure samples to document baseline conditions and to detect any hydrogen-induced changes. The analytical programme combined optical microscopy (OM), scanning electron microscopy with energy-dispersive spectroscopy (SEM-EDS) and X-ray powder diffraction (XRPD).
All thin-section preparations followed protocols adapted for soluble evaporitic minerals, as described below. Petrographic thin section analysis and SEM-EDS observations are used primarily to constrain textural relationships and pore-hosting phases rather than to define bulk mineralogical composition.

2.2.1. Optical microscopy

Thin-section petrography was performed using a Zeiss Axio Imager A1m polarised-light microscope and a Zeiss Axio Zoom V16 stereomicroscope at the Centro Musei delle Scienze Naturali e Fisiche, University of Naples Federico II. Images were acquired with a Zeiss AxioCam ICc5 camera and processed using AxioVision SE64 (v. 4.9.1), equipped with the AutoMeasure, Extended Focus and Z-Stack modules. Observations were carried out in both plane-polarised and cross-polarised transmitted light. Two preparation protocols were used for thin-section preparation, depending on the sample type. For the 25 mm-diameter pre-exposure cores (RS and KS series), thin sections approximately 150-200 µm thick were prepared by an external laboratory from hand specimens collected in the mine. A low-speed saw with white mineral oil was used as lubricant to minimise frictional heating and mechanically induced deformation. Both faces were coated with glass coverslips to prevent alteration of the hygroscopic salt minerals. For the post-exposure batch samples, sections approximately 10 mm thick were cut directly from the 25 mm-diameter cores, and both surfaces were ground and polished dry using progressive abrasive papers (1000, 2500 and 4000 grit) to a final thickness of < 0.5 mm. Both surfaces were re-polished with 4000-grit paper prior to each observation session. These preparations were used for both optical microscopy and SEM-EDS analysis. The samples examined included halite-dominated samples (RS1, RS3, RS10 and RS14 as pure halite, ≥99 wt% NaCl; RS4 as nearly pure halite, 97.15 wt% NaCl; and RS18), kainite-bearing rocks (KS2, KS3, KS5) and post-exposure batch samples (KS5_batch, RS3_batch, RS4_batch). Pre-exposure thin sections are presented in Supplementary Material S7.1 (Figs. S6-S15); post-exposure thin sections are in S7.2 (Figs. S20-S22).

2.2.2. Scanning electron microscopy with energy-dispersive spectroscopy (SEM-EDS)

Detailed chemical and morphological investigations were conducted on a subset of samples (RS1, RS4, RS10, RS14, KS5) selected based on the optical microscopy results. Analyses were performed at DiSTAR facilities, using a Zeiss Merlin VP Compact field-emission SEM equipped with an Oxford Instruments X-Max 50 EDS detector and a charge compensation system. For quantitative mineral chemistry, polished sections were coated with graphite using a sputter coater. In both cases, preparation and analysis were completed within the same day to avoid atmospheric alteration of the hygroscopic salt surfaces. Quantitative EDS data are reported in Supplementary Material S9 (Table S3).

2.2.3. X-ray powder diffraction

X-ray powder diffraction (XRPD) measurements were performed using a Rigaku RINT2500 laboratory diffractometer (18 kW), equipped with a rotating copper anode. The instrument operates in Debye-Scherrer transmission geometry and is fitted with an asymmetric Johansson Ge (111) monochromator and a silicon strip detector (D/TeX Ultra). Each sample was gently ground, and the resulting powder was used to fill a 0.5 mm Lindemann glass capillary, mounted along the diffractometer axis and continuously rotated during data acquisition. All X-ray diffraction patterns were collected at 50 kV and 200 mA (10 kW). Data were acquired over an angular range of 5-120° (2θ), with a step size of 0.02° (2θ) and a scanning speed of 5° min^{-1}. Qualitative phase identification

and semi-qualitative analysis were performed using the QUALX 2.0 software (Altomare et al., 2015), which utilizes the freely available POW_COD database.
The samples analysed included halite-dominated samples (RS1, RS10, RS14: pure halite; RS4: nearly pure halite), kainite-bearing rock (KS5) and post-exposure batch samples (RS3-batch, RS4-batch, KS5-batch). Pre-exposure diffractograms are presented in Supplementary Material S8.1 (Figs. S23-S27); post-exposure diffractograms in S8.2 (Figs. S28-S30).

2.3. Geochemical characterisation of bulk rock

Major- and trace-element compositions were determined on a broad set of samples to characterise the compositional variability of the deposit. All geochemical analyses were performed on bulk-rock powders obtained by total dissolution; soluble and insoluble fractions were not analysed separately.
Halite-dominated samples (RS1, RS3, RS10, RS14: pure halite; RS4, RS12, RS15: nearly pure halite), kainite-bearing rock (KS5) and post-exposure batch samples (RS3-batch, RS4-batch, KS5-batch) were analysed using the following techniques:
(i) Bulk chemistry: inductively coupled plasma optical emission spectrometry (FUS-ICP-OES) for major elements; instrumental neutron activation analysis (INAA) for Cl; ICP-MS after lithium borate fusion for rare earth elements (REEs). All bulk analyses were performed at Activation Laboratories (Ontario, Canada).
(ii) Total carbon and sulphur: combustion analysis using a LECO CS844 analyser.
(iii) X-ray fluorescence (XRF): sequential wavelength-dispersive spectrometry (PANalytical Axios, DISTAR facilities) was used to confirm compositional variability. Analytical uncertainty is 1-2% for major elements and 5-10% for trace elements.

2.4. Porosity and pore-structure analysis

The pore architecture of the Realmonte evaporites was characterised using two complementary techniques: mercury intrusion porosimetry (MIP) and X-ray micro-computed tomography (µCT). MIP provides quantitative pore-throat size distributions and total connected porosity, while µCT enables three-dimensional visualisation of pore morphology and spatial connectivity. The integration of both methods allows multi-scale reconstruction of pore networks from nanometre-scale throats (MIP) to micrometre-scale voids and fractures (µCT).

2.4.1. Mercury intrusion porosimetry (MIP)

MIP analyses were carried out at DISTAR using Thermo Finnigan Pascal 140/440 high-pressure mercury intrusion porosimetry instruments (together covering up to 400 MPa). Each core was fragmented into 1-3 cm chips and vacuum-dried at 40 °C for 24 hours prior to analysis. Measurements covered a pore-diameter range from 4 nm to 100 µm, spanning the mesopore to macropore range sensu IUPAC (Thommes et al., 2015). Calculation of pore diameter was performed applying the Washburn equation and assuming cylindrical pores shape, a surface tension of 0.48 N/m, a mercury contact angle of 140°.
The total connected porosity (φ_Hg) reported in this study corresponds to the cumulative volume of mercury injected up to the maximum applied pressure, normalised by the sample bulk volume. The

full sample set comprised halite-dominated samples, kainite-bearing rock (KS5) and post-exposure batch samples.

2.4.2. X ray-CT & Synchrotron imaging and processing

Two samples were selected for X-ray micro-computed tomography (µCT) analysis. Sample RS1 is a natural, unaltered, nearly pure halite core representative of the dominant lithology in the Realmonte succession. RS1 was selected as the reference halite sample for µCT analysis because its voxel size (30.98 µm) allows the most meaningful comparison with the MIP microporosity window among the available scans. Sample KS5_batch is the only specimen in the present study subjected to cyclic hydrogen injection and withdrawal prior to imaging, and its inclusion therefore provides a direct basis for assessing whether H_2 cycling induces measurable structural modification in evaporitic rock. Additionally, KS5_batch was scanned at a synchrotron source, yielding a finer effective resolution relative to sample size than the laboratory-scanned core. µCT is used here to visualise the three-dimensional pore network rather than to quantify total porosity, which is determined by mercury intrusion porosimetry.

RS1 (25.4 mm diameter) was scanned on a laboratory Zeiss Xradia 520 Versa system (160 kV, 10 W, HE3 filter, 2× binning, 2401 projections at 1 s exposure per projection) using a three-section stitch protocol to cover the full core length. The reconstructed volume consists of 16-bit unsigned integer TIFF stacks (grey-value range 0-65535). A subset of 318 consecutive slices was extracted from the reconstructed volume, avoiding stitch boundaries where reconstruction artefacts concentrate. KS5_batch (35 mm diameter) was scanned at Diamond Light Source (DLS, UK) on beamline I13-2, yielding a reconstructed volume of 500^3 voxels at an isotropic voxel size of 22.0 µm, corresponding to a cubic field of view of 11 × 11 × 11 mm (~1.33 cm^3). The synchrotron source provided near-monochromatic beam conditions and a high contrast-to-noise ratio. Acquisition parameters for both samples are summarised in Table 2.

Table 2. Micro-CT acquisition parameters for samples RS1 and KS5_batch. DLS = Diamond Light Source.

Parameter	RS1	KS5_batch
Source / Instrument	Zeiss Xradia 520 Versa	DLS beamline I13-2
Sample diameter (mm)	25.4	35
Voxel size (µm)	30.98	22.0
Voltage / Power	160 kV / 10 W	Synchrotron
Filter / Binning	HE3 / 2×	0.5 mm Cu
Projections / Exposure	2401 / 1 s	3142
Acquisition mode	3-section stitch	Single volume
Slices analysed	318	500
H_2 cycling prior to scan	No	Yes

All image processing and segmentation were carried out in Avizo 2024.1 (Thermo Fisher Scientific). Each volume was pre-processed with an edge-preserving anisotropic diffusion filter to suppress acquisition noise while retaining phase-boundary sharpness. A binary sample mask was constructed for each dataset by arithmetic operations on the greyscale volume to restrict subsequent measurements to the physical core, excluding the surrounding air annulus and setting all external voxels to zero.

Segmentation principle and thresholding criteria

Phase segmentation was performed using the *Interactive Thresholding* module in Avizo, which assigns voxels to discrete phase labels based on user-defined grey-value (GV) intervals derived from the attenuation histogram. The approach relies on the fact that mineral and fluid phases exhibit characteristic X-ray attenuation ranges that translate into distinct GV populations within the reconstructed volume. Lower-density phases (air, brine) correspond to lower GV values, whereas denser phases (halite, anhydrite) occupy higher ranges.

For sample RS1, the histogram of the masked volume shows a multimodal distribution with four populations (Supplementary Material S5, Fig. S4a): (i) background and air-filled porosity (GV~0), (ii) an intermediate population representing brine-filled pores and partial-volume voxels at pore-matrix interfaces (GV~21000), (iii) the halite matrix (GV~39000), and (iv) anhydrite and dense accessory phases (GV~64000). Pore space was segmented using a threshold range of 18000-28000 GV, selected to isolate the intermediate-attenuation population between the background minimum (GV~11000) and the halite peak. At the current voxel resolution, air- and brine-filled pores cannot be separated by grey-value thresholding alone (see Supplementary Material S5).

For sample KS5_batch, the histogram differs because kainite and halite form a single composite matrix peak due to their similar densities ($\rho_{kainite}$ = 2.13 g cm^{-3}; ρ_{halite} = 2.16 g cm^{-3}). Pore segmentation was therefore adapted to the specific histogram morphology. Segmentation thresholds and phase-assignment criteria are summarised in Table S1.

The voxel size of the datasets (30.98 µm for RS1; 22.0 µm for KS5_batch) defines the lower detection limit for resolvable pore features. Pores smaller than ~2-3 voxels (62-93 µm for RS1; 44-66 µm for KS5_batch) are affected by partial-volume effects, producing intermediate GV values. To reduce noise-related artefacts, only connected components ≥8 voxels were retained, corresponding to minimum resolvable volumes of ~2.38×10^5 µm³ (RS1) and ~8.53×10^4 µm³ (KS5_batch). Smaller objects were discarded as they cannot be reliably distinguished from reconstruction noise or ring artefacts.

For visualisation purposes, an additional filter was applied to RS1 by removing objects smaller than 100 voxels (~2.97×10^6 µm³) from the rendering label field (Fig. 6d). This step was applied only for figure generation; quantitative analyses were performed on the unfiltered segmented volumes (≥8 voxels).

Pore objects were separated using watershed-based connected-component labelling and characterised through standard shape descriptors (equivalent spherical diameter, anisotropy, elongation, flatness). Porosity was calculated as the ratio between segmented pore volume and masked sample volume. For RS1, Avizo-derived porosity was cross-validated through a Python-based analysis of the exported label field (agreement within 0.013 percentage points; Supplementary Material S5). For KS5_batch, estimates were further validated by stereological point counting on 30 cross-sections and by three-dimensional connected-component analysis on a representative sub-volume.

μCT-derived porosity reflects only pores and fractures larger than the voxel size and therefore represents a lower-bound estimate of total porosity. Sub-resolution pore populations are captured by mercury intrusion porosimetry (MIP), and the integration of the two datasets is discussed in Section 4.

2.5. Geochemical modelling (PHREEQC)

Thermodynamic equilibrium modelling was performed using PHREEQC v.3.8.6 (Parkhurst and Appelo, 2013) to assess the stability of halite-kainite mineral assemblages in the presence of hydrogen and brine under conditions representative of subsurface storage caverns (Laban, 2020). Three scenarios were considered: (i) halite in contact with H_2 and saturated NaCl brine; (ii) a mixed halite kainite system exposed to H_2 and saturated brine; and (iii) a one-month dynamic evolution simulating halite in contact with undersaturated brine. The modelling was designed to complement the laboratory experiments by evaluating mineral stability under conditions (90 °C, 8.9 MPa) more representative of operational cavern depths than the laboratory batch test (20 °C, 10 MPa), thereby extending the experimental constraints to a broader range of storage-relevant scenarios.
All simulations were run using both the phreeqc.dat and pitzer.dat thermodynamic databases. The outputs provided quantitative constraints on mineral saturation indices, redox processes, hydrogen-brine interactions and precipitation-dissolution trends. Model input parameters and results are detailed in Supplementary Material S10 (Tables S5-S6).

3. Results

3.1. Pre-exposure characterisation

3.1.1. Petrographic and textural features

Halite-bearing samples (RS series).

Optical microscopy reveals a holocrystalline texture dominated by halite macrocrystals with euhedral, sub-euhedral and anhedral habits, occasionally elongated (Fig. 5a). Smaller euhedral crystals forming acicular radial aggregates with vivid interference colours (yellow to blue and pink) are identified as anhydrite.

Interstitial fluids are present at halite grain boundaries, appearing as dark-coloured, consistent with concentrated hypersaline brines trapped along grain boundaries. Organic compounds have been widely documented in Messinian halite fluid inclusions and crystal lattices, both at Realmonte (Isaji et al., 2019) and in the Crotone Basin (Cipriani et al., 2026), suggesting that organically enriched brines were a common feature of Messinian evaporite environments (Fig. 5b). Fluid inclusions are widespread, ranging from cubic to irregular elongated morphologies, and include two-phase (liquid-gas), solid-liquid and occasional three-phase types. Both primary and secondary inclusions occur with variable abundance. Clay material is frequently observed at halite crystal margins, often associated with sulphate minerals.

Kainite-bearing samples (KS series).

Samples KS2, KS3 and KS5 differ markedly from the RS series in both texture and mineralogy. They are dominated by equidimensional macro- and microcrystals of euhedral to sub-euhedral habit (Fig. 5c). Optical properties indicate kainite ($KMg(SO_4)Cl \cdot 3H_2O$) as the main phase, arranged in alternating layers of macrocrystals (~400 µm) and microcrystal aggregates (~80 µm). Halite, the second most abundant phase, occurs as anhedral infill between kainite grains or as layers in contact with kainite, reflecting late-stage intergranular precipitation. Accessory phases comprise small, elongated, low-interference crystals, likely carnallite and/or leonite, found within both kainite and halite.

Interstitial fluids occur along kainite grain boundaries, with dark colouration consistent with the organically enriched brines described above. Fluid inclusions in kainite are sub-circular to irregular, often solid-liquid biphasic (Fig. 5a-b); in halite, inclusions are cubic or elongated, predominantly liquid-gas biphasic. Primary and secondary inclusions are present in both phases. Optical microscopy of sample KS3 (Supplementary Material S7.1, Figs. 16-19) confirms that these textural features are not unique to KS5 but are shared across the KS series. KS2 exhibits the same layered arrangement of macro- and microcrystalline kainite domains, with anhedral halite as intergranular infill and dark interstitial fluids at grain boundaries. Visual estimation of the mineral proportions from cross-polarised images indicates approximately 60-70% kainite and 20-25% halite, broadly consistent with the XRPD-derived composition of KS5 (65.2% kainite, 28.8% halite). This compositional consistency and the fact that all KS cores were collected from the same horizon, supports the interpretation that KS5 is representative of the kainite-bearing composition at Realmonte. While KS5 provides a representative example of the kainite-bearing lithology based on petrographic, compositional and porosimetric consistency across the KS series, the limited number of dynamic injection tests means that variability in the mechanical and petrophysical response within the KS series remains an important uncertainty that should be addressed in future experimental campaigns. Pre-exposure thin-section images are presented in Supplementary Material S7.1 (Figs. S6-S15).

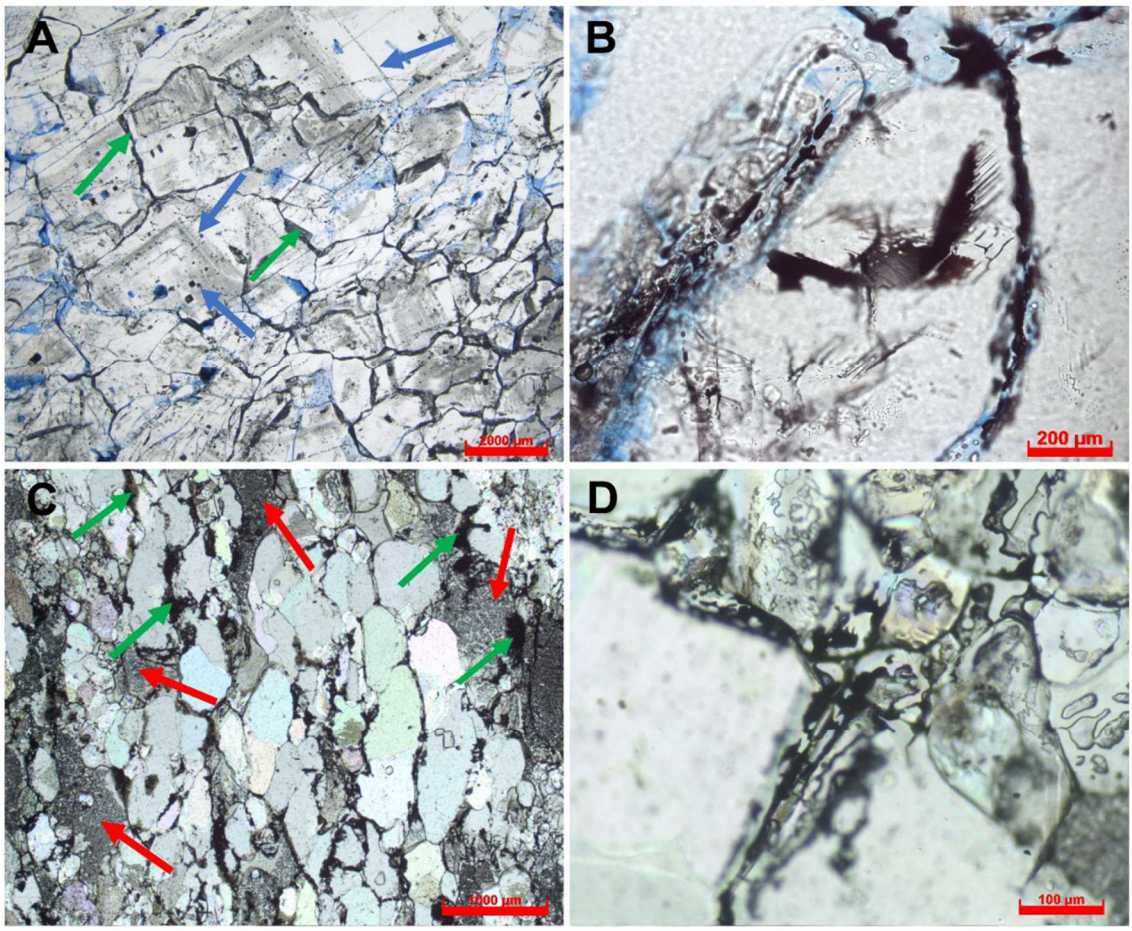

Fig 5 Thin-section images under plane-polarised light (PPL) showing textural features of the studied samples. (a) RS4: halite macrocrystals with interstitial fluids (green arrows) and fluid inclusions (blue arrows). (b) RS4: interstitial fluids and fluid inclusions hosted within halite. (c) KS2: interstitial fluids (green arrows) between kainite crystals and within anhedral halite (red arrows). (d) KS2: interstitial fluid and fluid inclusions within kainite crystals.

3.1.2. Chemical and mineralogical composition

Quantitative SEM-EDS analyses on thin sections of RS1, RS4, RS10, RS14 and KS5 confirmed marked mineralogical variability (Table S3). Calcium sulphate was detected as an accessory phase in RS1, RS10 and RS14 and celestine was identified in RS1 and RS10, typically in association with calcium sulphate in BSE images. RS14 also contains clay minerals and quartz intergrown with calcium sulphate. In KS5, leonite and polyhalite were detected.

Bulk geochemical data, combined with crystal-chemical and stoichiometric calculations, allowed estimation of the abundance of accessory mineral phases in each sample (Table 3). As regard the RS series, halite content ranges from 97.15 (RS4) to 99.92% (RS10). The most common accessory phases are anhydrite (0.13-0.63%), calcite (0.09-0.16%) and dolomite (up to 0.4% in RS4). The most frequent mineral association is calcite + anhydrite + halite, identified in RS1 and RS3. A clay fraction is invariably present, albeit in variable proportions.

Qualitative XRPD results for the RS powders are reported in Supplementary Material S8.1 (Figs. S23-S27). Semi-quantitative determination based on the same dataset revealed appreciable amounts of anhydrite in RS1 (3.8%), while all other samples (RS4, RS10, and RS14) are predominantly composed of pure halite.

For sample KS5, bulk geochemical data indicate a composition of 65.8% kainite, 18.1% halite, 12.2% carnallite, and 1.0% dolomite. XRPD results are broadly consistent, yielding 65.2% kainite, 28.8% halite, 3.8% carnallite, and 2.2% leonite. These proportions are consistent with the optical microscopy observations, which identify kainite as the dominant phase with halite occurring as anhedral intergranular infill and accessory carnallite and leonite forming small, elongated crystals distributed within both mineral hosts. The observed discrepancy in halite and carnallite proportions between the two analytical methods reflects the different sampling volumes, analytical sensitivities and the inherent textural heterogeneity of the kainite-halite assemblage. The bulk geochemical estimate is adopted as the reference for quantitative phase proportions, given its integration over a larger sample volume, while XRPD provides the primary mineralogical phase identification.

Table 3. Mineral phase abundances (wt%) estimated from bulk geochemical data (crystal-chemical recalculation) and semi-quantitative XRPD analysis (QUALX 2.0 software). Dol = dolomite; Cal = calcite; Anh = anhydrite; Cls = celestine; Hl = halite; Phy = polyhalite; Kn = kainite; Crn = carnallite; Leo = leonite. '–' = not detected.

Sample	Data	Dol	Cal	Anh	Cls	Hl	Phy	Kn	Crn	Leo	Total	Clays	Fluids	Total
RS1	Chem	–	0.09	0.26	–	99.59	–	–	–	–	99.93	0.64	0.30	100.87
	XRPD	–	–	3.80	–	96.20	–	–	–	–	100.00	–	–	100.00
RS3	Chem	–	0.09	0.13	–	99.25	–	–	–	–	99.46	0.59	0.23	100.28
RS3_batch	Chem	–	0.17	0.60	–	98.28	–	–	–	–	99.05	1.50	1.01	101.55
	XRPD	–	–	–	–	100.00	–	–	–	–	100.00	–	–	100.00
RS4	Chem	0.40	–	–	–	97.15	–	0.56	–	–	98.11	1.29	0.48	99.88
	XRPD	–	–	–	–	100.00	–	–	–	–	100.00	–	–	100.00
RS4_batch	Chem	0.23	–	–	–	96.60	–	0.44	–	–	97.27	1.74	0.71	99.71
	XRPD	–	–	–	–	100.00	–	–	–	–	100.00	–	–	100.00
RS10	Chem	–	–	–	–	99.92	–	–	–	–	99.92	0.49	0.10	100.51
	XRPD	–	–	–	–	100.00	–	–	–	–	100.00	–	–	100.00
RS12	Chem	–	0.16	0.63	–	98.48	–	–	–	–	99.27	1.25	0.95	101.48
RS14	Chem	–	–	–	–	99.85	–	–	–	–	99.85	0.46	0.07	100.38
	XRPD	–	–	–	–	100.00	–	–	–	–	100.00	–	–	100.00
RS15	Chem	–	–	–	–	98.79	–	–	–	–	98.79	0.95	0.46	100.20
KS5	Chem	1.01	–	–	–	18.14	–	65.79	12.15	–	97.09	2.58	2.27	101.94
	XRPD	–	–	–	–	28.80	–	65.20	3.80	2.20	100.00	–	–	100.00
KS5_batch	Chem	0.72	–	–	–	33.84	–	50.56	12.37	–	97.49	2.46	1.66	101.61
	XRPD	–	–	–	–	23.20	–	76.80	–	–	100.00	–	–	100.00

3.1.3. µCT pore structure and three-dimensional characterisation

Three-dimensional reconstruction of the segmented µCT volume for sample RS1 reveals a fracture-dominated pore architecture controlled by halite grain-boundary geometry. The µCT-derived porosity (φ_CT) is 2.13%. The pore population is overwhelmingly dominated by a single connected component that accounts for 78.8% of the total segmented pore volume, corresponding to a pervasive three-dimensional network of sub-planar fractures aligned along halite grain boundaries (Fig. 6a-b). The remaining 1 989 objects (≥ 8 voxels) are small and isolated, with a median equivalent spherical diameter of 151 µm. Shape descriptors confirm the fracture-dominated character of the pore space: the mean anisotropy is 0.86, the mean flatness 0.33, and 82% of resolved objects exhibit anisotropy values exceeding 0.7. Of all labelled objects, 9.2% are in contact with the volume boundary, suggesting possible connectivity with the sample boundary. Sparse high-attenuation domains occur along crystal margins and correspond to anhydrite (3.8% by XRPD), visible in 3D renderings as discontinuous clusters at grain boundaries.

The fidelity of the pore segmentation was verified by overlaying the segmented 3D pore network onto the original greyscale ortho slices at multiple positions along the vertical axis (Fig. 6d; Supplementary Material S6, Fig. S5). Blue segmented objects correspond consistently to dark, low-attenuation features in the greyscale data, confirming that the thresholding range captures real microstructural features rather than reconstruction noise. The filtered subvolume rendering reveals discrete, tabular to lamellar fracture bodies with lateral extents of several hundred micrometres, geometrically consistent with intergranular fractures along halite crystal contacts.

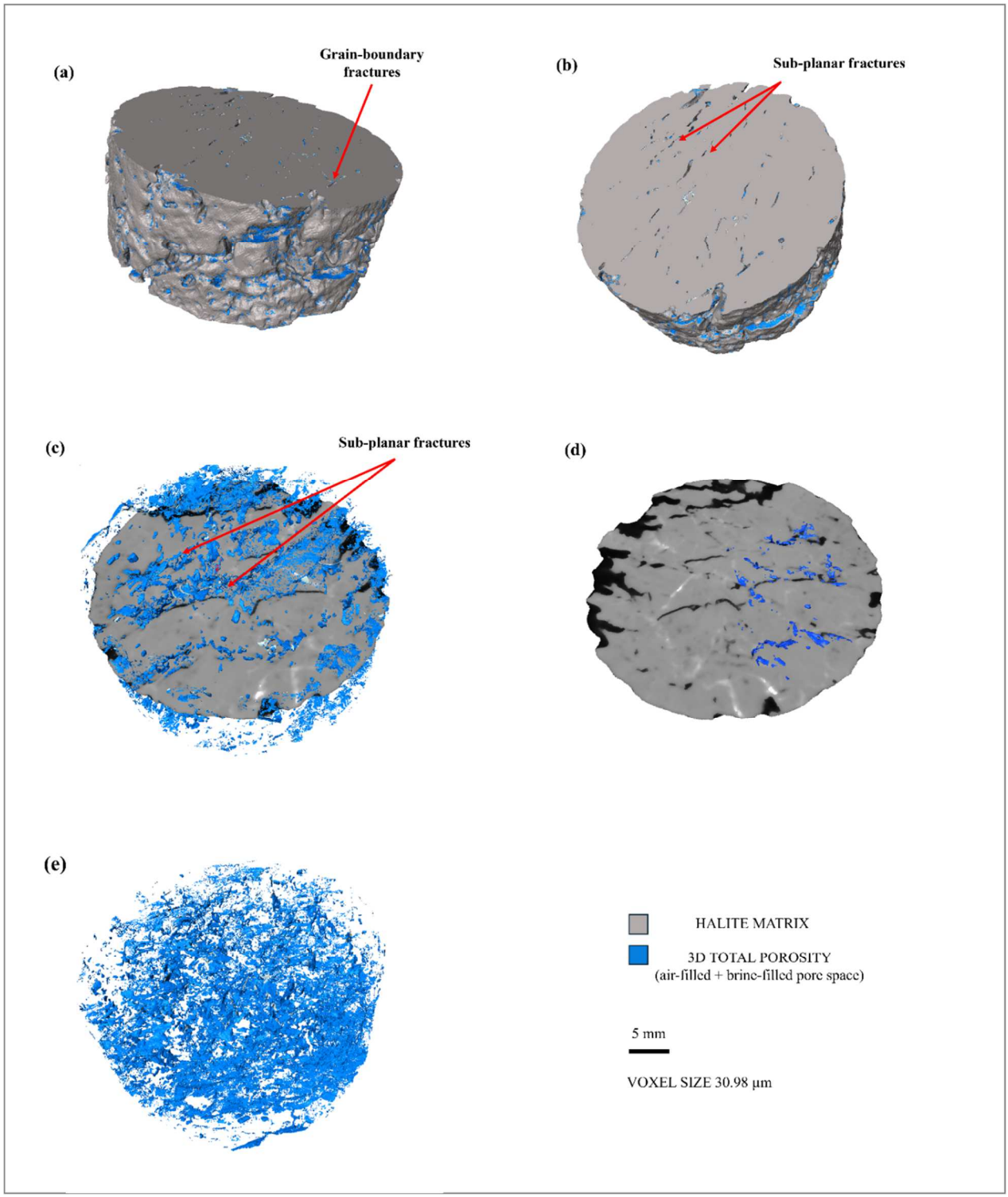

Figure 6. Three-dimensional µCT reconstruction of sample RS1. **(a)** Oblique view of the volume rendering showing the halite matrix (grey) and segmented porosity (blue) concentrated along grain boundaries. **(b)** Top view of the same volume, highlighting the sub-planar fracture geometry aligned along halite crystal contacts. **(c)** Halite matrix rendered semi-transparent to expose the full 3D pore network. **(d)** Representative subvolume extracted from the volume-filtered label field and overlain on ortho slice 79; blue features are discrete fracture bodies, dark features in the greyscale background correspond to low-attenuation domains outside the Interactive Thresholding range. **(e)** Complete segmented pore network with halite matrix removed, showing the pervasive grain-boundary fracture system dominated by a single connected component accounting for 78.8% of the total segmented pore volume. Blue phase represents total CT-derived porosity, including both air-filled and brine-filled pore space.

3.1.4. Pre-exposure mercury intrusion porosity (MIP)

Pre-exposure MIP measurements on halite- and kainite-rich samples reveal generally low total intrusion porosity values (φ_Hg, cumulative volume injected up to 400 MPa), ranging from 1.18% (RS17) to 4.76% (RS13), with a dataset mean of 2.31% (Table 4), consistent with literature data for compact evaporitic lithologies (Brouard et al., 2001; Kolano et al., 2024) and confirming the inherently low pore connectivity expected for Messinian halite. Additional halite cores (RS2, RS12, RS15, RS17), for which only MIP data were acquired, are included in the pre-exposure dataset to extend the porosity baseline across the full stratigraphic range of the mine (Table 4; Figs. 7-8); their pore-size distributions are used in the classification below but are not discussed individually in the absence of supporting mineralogical or geochemical data and are not employed in cause-effect correlations with hydrogen exposure (post-batch analyses are reported only for cores with full mineralogical and petrographic characterisation: RS3, RS4 and KS5). Total porosity (Ø), modal pore diameter and total pore surface area (TPS) were derived from the intrusion curve, integrated up to the maximum applied pressure (400 MPa). The kainite-bearing samples (KS1-KS5) yield total porosities in the range 1.07-1.48% (mean 1.27 ± 0.17%), systematically lower than the RS-series mean and comparable to the most compact halite core in the dataset (RS17, 1.18%). Two distinct pore architectures are recognised: KS1 and KS3 are macropore-dominated, with modal diameters of 10.3 and 12.8 µm respectively, whereas KS2, KS4 and KS5 are sub-porosity-dominated, with modal diameters of 3.8, 6.9 and 5.5 nm. KS3 exhibits the highest total pore surface area of the KS dataset (2.45 m^2/g), indicating a well-developed internal surface despite low bulk porosity.

Table 4. Summary of pre-exposure MIP results. Ø = total porosity (%); Modal D = modal pore diameter (µm); TPS = total pore surface area ($m^2\ g^{-1}$). Pore class: macro (>8 µm), micro (1–8 µm), sub (<1 µm) (Chen et al., 2018).

Sample	Ø (%)	Modal D (µm)	TPS ($m^2\ g^{-1}$)	Dominant pore class
RS1	3.99	13.79	3.05	macro
RS2	2.58	0.007	1.98	sub
RS3	3.11	19.11	1.21	macro
RS4	4.66	0.005	2.327	sub
RS10	1.71	0.004	2.16	sub
RS12	2.02	0.004	2.35	sub
RS13	4.76	4.78	3.58	micro
RS14	2.49	0.005	1.97	sub
RS15	2.13	29.36	2.67	macro
RS17	1.18	0.011	2.48	sub
RS18	3.06	16.75	2.26	macro
KS1	1.46	10.30	1.24	macro
KS2	1.11	0.004	0.93	sub
KS3	1.48	12.77	2.45	macro
KS4	1.07	0.007	0.85	sub
KS5	1.22	0.006	1.91	sub

Pore-size distributions (PSDs; Figs. 7-8) permit classification of pore types into three domains (Chen et al., 2018): (i) sub-porosity (D < 1 µm), dominant in RS2, RS4, RS10, RS12, RS14, RS17, KS2, KS4 and KS5, with modal diameters of 0.004-0.011 µm; (ii) microporosity (1-8 µm), characterising RS13, with modal diameters of 4.5-5.8 µm; and (iii) macroporosity (D > 8 µm), present in RS1, RS3, RS15, RS18, KS1 and KS3. Total pore surface areas span 0.64 m²/g to 3.58 m²/g (RS13), consistent with the predominance of sub-micrometric pores, whose high surface-to-volume ratio disproportionately controls TPS even at low total porosity.

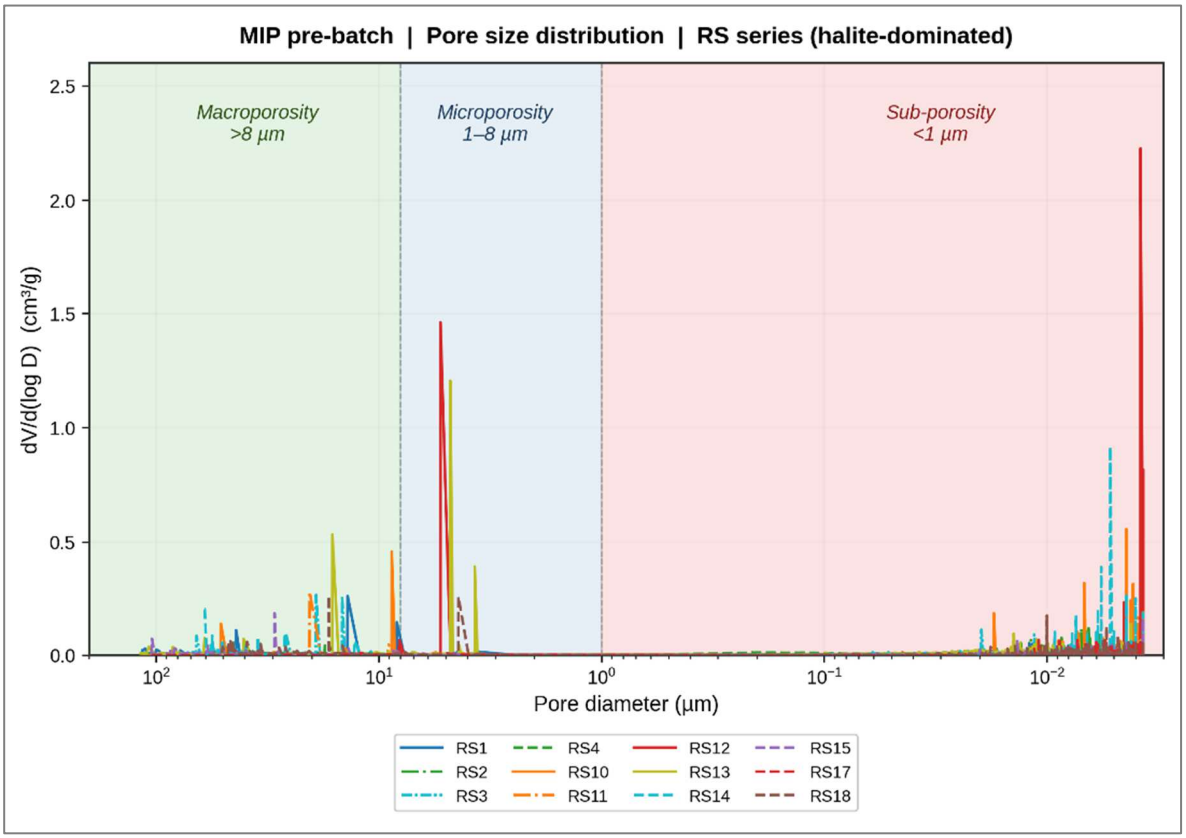

Fig. 7. Pore-size distribution (dV/d(log D) vs. pore diameter) of all pre-exposure halite-dominated samples (RS series) measured by MIP. The x-axis is plotted on a logarithmic scale with inverted direction (coarser pores on the left). Coloured background fields delineate the three pore-size domains of Chen et al. (2018). Dashed vertical lines mark class boundaries at D = 1 µm and D = 8 µm. Note the multimodal character of the dataset, reflecting inherent textural heterogeneity of the Messinian evaporitic succession.

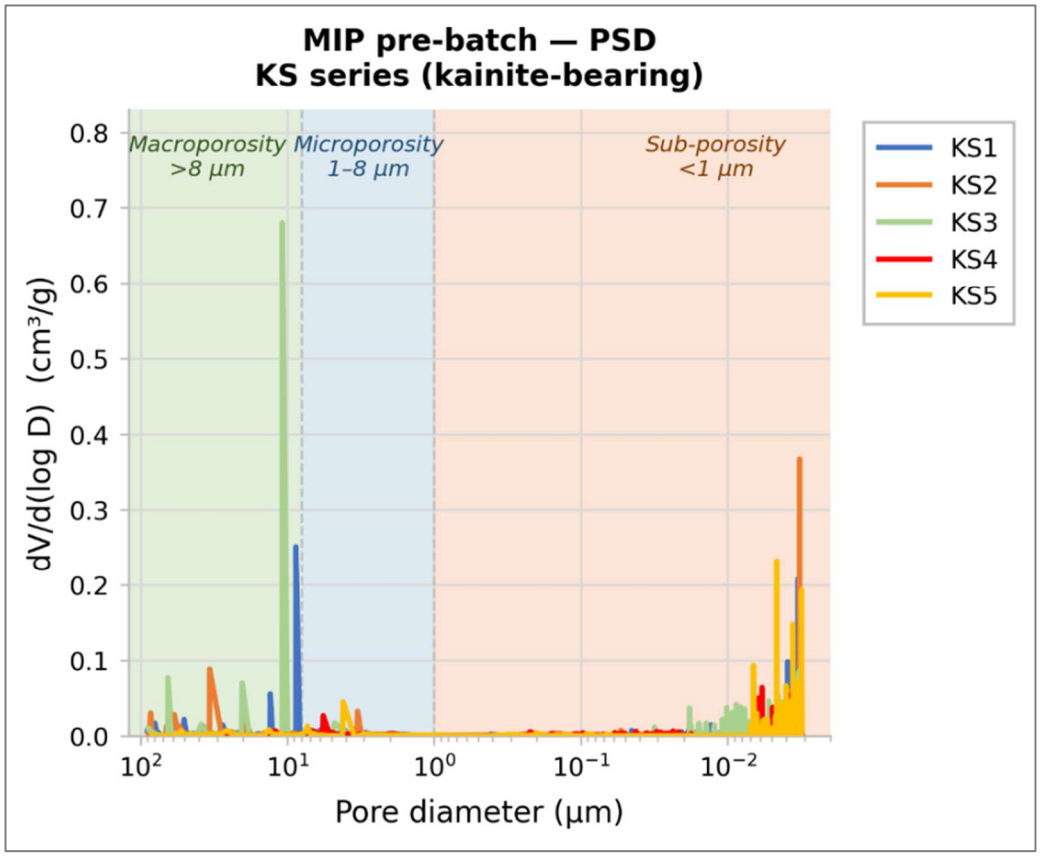

Fig. 8. Pore-size distribution of kainite-bearing pre-exposure samples (KS series). Layout and pore-class boundaries as in Fig. 7. KS5, the kainite-bearing sample subjected to hydrogen experiments, is characterised by a sub-porosity-dominated distribution (modal D~0.005 µm) and low total intrusion volume, consistent with the compact crystalline framework of kainite-halite intergrowths.

The highest pre-exposure porosities, RS13 (4.76%), RS4 (4.66%), RS1 (3.99%), RS3 (3.11%) and RS18 (3.06%), are associated with macropore-, micropore- or sub-porosity-dominated distributions and likely reflect localised micro-fracturing or enhanced pore connectivity related to depositional or early diagenetic processes. In RS4, the combination of high total porosity with a sub-porosity-dominated throat distribution (modal D = 0.004-0.011 µm, §3.1.4) indicates abundant fine, well-connected throats rather than macroscopic fracture features. In contrast, compact samples such as KS4 (1.07%), RS17 (1.18%) and KS5 (1.22%) exhibit narrow PSD peaks dominated by sub-porosity, indicative of a structurally closed, poorly interconnected pore network. These baseline differences in pore architecture are critical for interpreting the heterogeneous response of individual samples to subsequent hydrogen exposure.

3.2. Hydrogen exposure tests

3.2.1. Cyclic H_2 injection (sample KS5)

Sample KS5 was subjected to two cyclic H_2 pressure regimes at the University of Edinburgh: a seasonal cycle (2 h loading + 2 h unloading, 1 cycle) and a monthly cycle (17 min loading + 17 min unloading, 12 cycles), both at a mean H_2 injection pressure (P_1) of 7.89 bar. For both regimes, the final internal pressure (P_2) averaged 7.67 bar, yielding a consistent upstream-downstream pressure

drop ΔP~0.22 bar per cycle (Figs. 9-10). This reproducible pressure differential provides clear evidence of limited but measurable gas penetration through the rock matrix.

Permeability. Gas permeability was derived from the transient pressure-decay response using Darcy's law. The theoretical volumetric flow rate Q is of the order of 10^{-13}-10^{-12} m^3/s (≤0.2 picolitres/s), well below the detection limit of conventional flow meters; permeability was therefore calculated from the temporal pressure evolution rather than from direct flow measurement. Results are summarised in Table 5.

Table 5. Apparent and intrinsic (Klinkenberg-corrected) H_2 permeability of sample KS5 derived from cyclic injection tests. μ_{H_2} (20 °C) = 8.80×10^{-6} Pa·s.

Cycle	Duration (s)	Apparent K (m^2)	Intrinsic K (m^2)
Seasonal	7 200	3.48×10^{-21}	3.27×10^{-21}
Monthly	1 020	2.46×10^{-20}	2.31×10^{-20}

At the mean test pressure of 0.789 MPa, the Klinkenberg correction factor (1 + b/P) was estimated at 1.063 using a Klinkenberg coefficient b ~ 0.05 MPa, consistent with empirical correlations for low-permeability rocks of comparable permeability range and with Klinkenberg-effect observations reported for tight rock salt (Tanikawa & Shimamoto, 2009). Gas-slippage effects therefore account for less than 7% of the apparent permeability; apparent and intrinsic values are effectively equivalent. Both permeability values fall 3-4 orders of magnitude below published tightness thresholds for gas storage caprocks ($K \leq 10^{-17}$ m^2, Li et al., 2021; $K \leq 10^{-19}$ m^2, Nassan et al., 2025), confirming the extremely low gas transmissivity of the kainite-halite matrix.

The monthly-cycle permeability ($K = 2.46 \times 10^{-20}$ m^2) exceeds the seasonal value ($K = 3.48 \times 10^{-21}$ m^2) by approximately one order of magnitude. This discrepancy likely reflects a rate-dependent mechanical response of the rock, such as transient grain-boundary dilation or incomplete viscoplastic closure, under higher-frequency cycling, rather than a steady-state increase in intrinsic permeability. The effect is consistent with the known time-dependent rheology of rock salt and suggests that permeability estimates from short-duration cycles may represent upper bounds on the true matrix permeability. The effect represents a rate-dependent mechanical response rather than a stable permeability increase, and its implications for cyclic storage operations are discussed in Section 4.

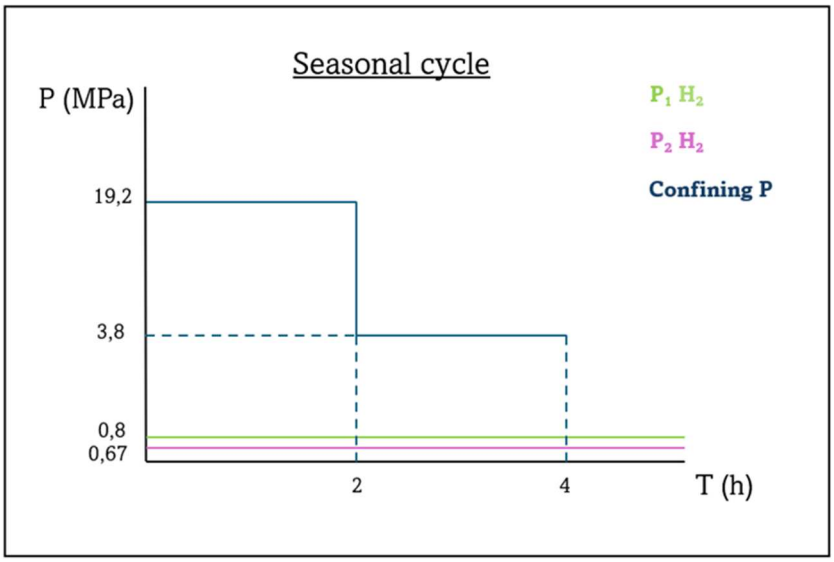

Fig. 9. Pressure-time record for the seasonal H_2 injection cycle (2 h loading + 2 h unloading) on sample KS5. P_1 = upstream injection pressure; P_2 = downstream equilibrium pressure. The consistent $\Delta P \sim 0.22$ bar indicates limited gas penetration through the kainite-halite matrix.

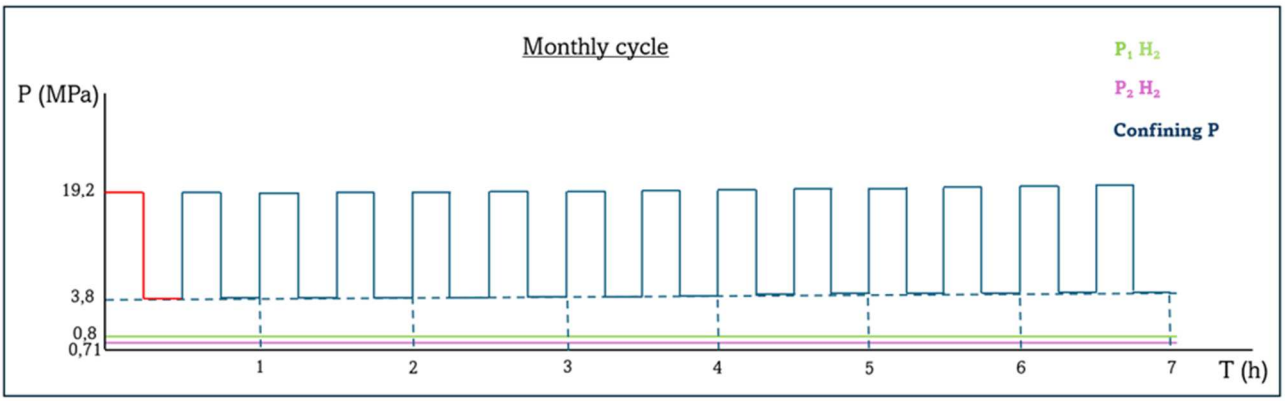

Fig. 10. Pressure-time record for the monthly H_2 injection cycles (12 cycles of 17 min loading + 17 min unloading) on sample KS5. The reproducible pressure response across successive cycles confirms that permeability remains stable under repeated loading.

Effective diffusivity. The effective H_2 hydraulic diffusivity (D_eff) was estimated from the Klinkenberg-corrected permeability using the standard pressure-pulse-decay relation for tight porous media ($D_{eff} = K \cdot P_{mean} / (\mu \cdot \varphi \cdot \tau)$; Hsieh et al., 1981; Cui et al., 2009), with $\varphi_{MIP} = 1.22\%$ and a tortuosity τ = 2-5 (typical range for compact salt rock). Results are presented in Table 6.

Table 6. Effective H_2 hydraulic diffusivity estimates for sample KS5, derived from Klinkenberg-corrected permeability via the pressure-pulse-decay relation (Hsieh et al., 1981; Cui et al., 2009). Literature values for comparison."

K input	τ	D_eff (m²/s)	Literature comparison	Reference
K_seasonal	2	1.28×10^{-8}	1.3×10^{-8}	Strauch et al. (2023)
K_seasonal	3	8.52×10^{-9}	$3.5–12 \times 10^{-10}$	Song et al. (2024)
K_monthly	3	6.03×10^{-8}	$10^{-10} – 10^{-9}$	Ghaedi & Gholami (2025)

At $\tau = 3$ (intermediate estimate), D_eff derived from K_seasonal is 8.5×10^{-9} m²/s, consistent with published values for micro-fractured halite (Strauch et al., 2023) and approximately one order of magnitude above data for pure halite cores from China (Song et al., 2024). The higher diffusivity relative to pure halite is consistent with the mineralogical complexity of KS5 (65.2% kainite, 28.8% halite, 3.8% carnallite, 2.2% leonite), which introduces a more developed grain-boundary network and sub-nanometre pore connectivity.

Under the Edinburgh test conditions (P_mean = 0.789 MPa), the Knudsen number is $Kn \approx 4.1$ for the KS5 modal pores (~5 nm) and Kn~0.002 for macropores (≥10 µm). The pore system therefore operates under a bimodal transport regime: transition Knudsen-viscous flow in sub-nanometre pores, and purely viscous (Darcian) flow in macropores. Both mechanisms coexist in parallel across the pore-size distribution, and the effective diffusivity reflects their combined contribution.

Following the cyclic injection test, sample KS5 was transferred to the static batch reactor for prolonged H_2 exposure under elevated pressure and temperature conditions, making it the only specimen in the dataset subjected to both dynamic and static hydrogen exposure. Post-exposure characterisation of this sample (hereafter KS5_batch) is reported alongside the other batch-reacted samples.

3.2.2. Static batch reaction

Three halite-dominated samples and the kainite-bearing sample KS5 were subjected to the static batch H_2 exposure protocol (10 MPa, 20 °C, 120 h) to evaluate potential mineralogical, geochemical and microstructural modifications induced by prolonged contact with hydrogen and brine. Post-exposure characterisation comprised MIP analysis on all seven batch-reacted samples, XRPD and SEM-EDS on selected specimens to assess mineral stability, and synchrotron µCT on sample KS5_batch to evaluate three-dimensional pore-structure evolution. Brine chemistry before and after the experiment was analysed for major cations and anions. Results are presented in the following subsections.

3.3 Post-batch petrographic and microstructural evolution

Post-treatment samples exhibit textural modifications relative to the pre-batch material, including changes in grain-boundary definition and fluid-inclusion distribution. Halite crystals exhibit blurred or indistinct boundaries, suggesting partial dissolution and reprecipitation, and fluid inclusions display increased connectivity (Fig. 11b). Indeed, although the samples retain a holocrystalline texture, halite crystals are subhedral and, in most cases, anhedral, locally, halite also forms cryptocrystalline aggregates (Fig. 11a) which are frequently associated with a clay phase or sulfate phases. The sulfates present, mostly anhydrite with subordinate amounts of polyhalite and kainite, appear locally reorganized, forming aggregates of elongated acicular or prismatic crystals along the boundaries or within domains of reprecipitated halite. Clay minerals are more widely dispersed along crystal contacts, suggesting partial mobilization during the cycles. Fluid inclusions and interstitial fluids also exhibit substantial textural differences compared to pre-batch samples. As shown in Figs. 11b and 11d, these fluids are no longer confined to interstitial spaces but also penetrate crystal interiors, forming complex networks of irregularly shaped inclusions. Fluid inclusions are generally large, consistently irregular in shape, and display cubic morphologies. These observations indicate localised microstructural reorganisation relative to the pre-batch samples, consistent with the pore-network modifications identified by µCT imaging and mercury intrusion porosimetry.

3.3.1 Kainite-bearing sample KS5

Sample KS5_batch, like the other batch samples, does not show mineralogical differences compared to its pre-batch counterpart, but it exhibits distinctive textural features. Kainite remains the dominant phase. The overall texture is comparable to that of the pre-batch sample, with alternating layers of large and small crystals; however, crystal size varies significantly (max~308 µm; min~100 µm). This narrowing of the crystal-size range relative to the pre-exposure sample (83-402 µm) is attributed to natural intra-sample variability and possible recrystallisation effects rather than to a systematic hydrogen-induced modification.

Kainite crystals exhibit blurred or indistinct boundaries, consistent with localised dissolution-reprecipitation textures. Moreover, the abundance of microcrystals decreases, and traces of recrystallization are visible in the larger kainite crystals (Figs. 11c). Halite continues to be the most abundant secondary mineral. Clay material is consistently present, particularly at the halite-kainite interfaces (Fig. 11d). As in the other samples, the most significant differences concern the texture of fluid inclusions and interstitial fluids. Interstitial fluids are concentrated at the interfaces between kainite and halite, extending along irregular, chaotic planes within the kainite crystals (Figs. 11c, 11d), forming extensive subcircular to irregular bodies. Fluid inclusions in halite are also present, mainly concentrated along crystal boundaries, where they typically exhibit cubic, though occasionally irregular, morphologies.

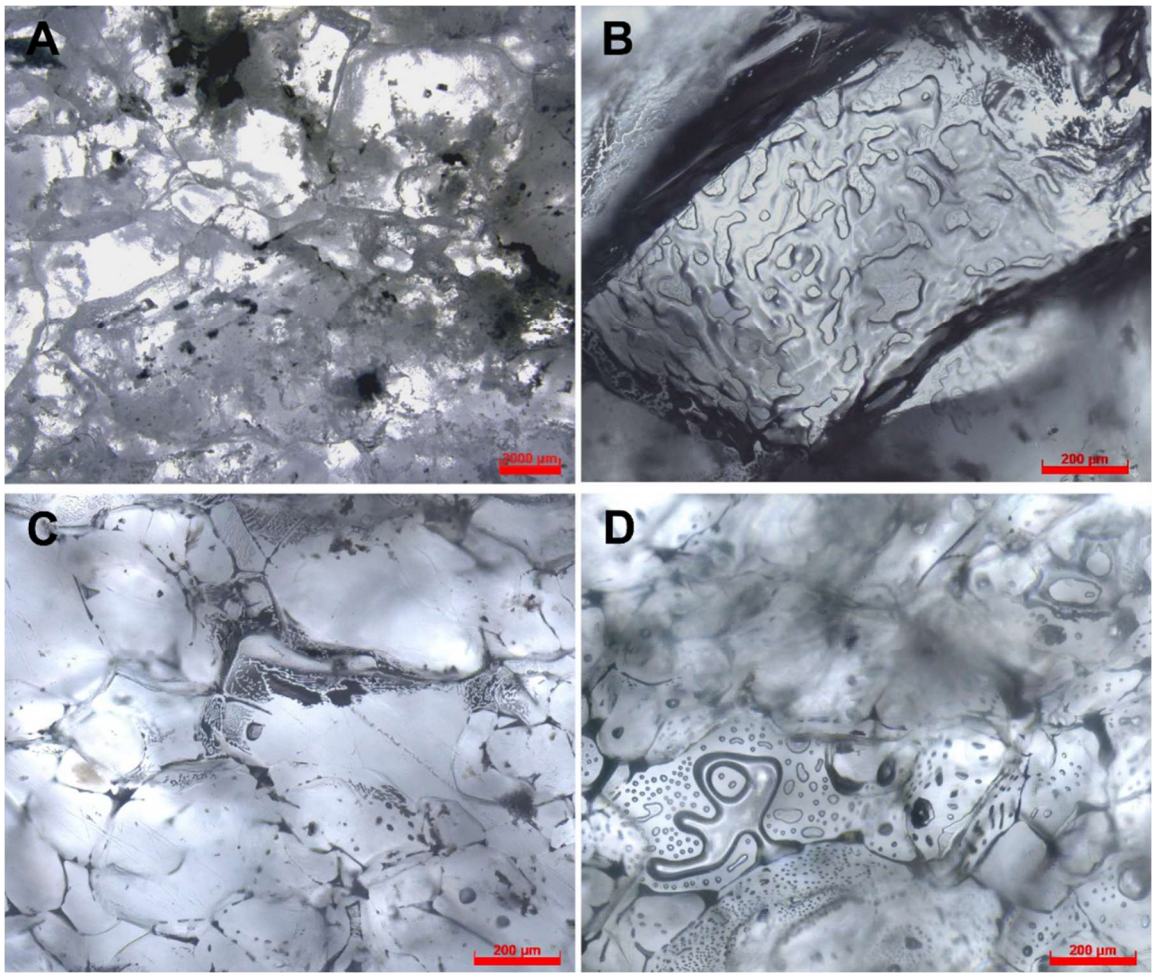

Fig.11 Post-exposure thin-section micrographs (transmitted light). (a) RS4_batch sample: halite crystals of variable size display partially resorbed margins. (b) RS3_batch: highly saline interstitial fluids extending from grain boundaries into crystal interiors and extend fluid inclusion in halite. (c) KS5_batch: Kainite crystals of variable size; smaller crystals are less abundant and display partially resorbed margins. (d) KS5_batch: Highly saline interstitial fluids extending from grain boundaries into crystal interiors.

3.3.2 Chemical and mineralogical composition (SEM-EDS, XRPD, post injection test)

Quantitative chemical analyzes for major, minor and trace elements confirm the mineralogical composition observed in the pre-batch samples, while revealing significant variability in the proportions of individual mineral phases at the quantitative level.
The clay fraction is always present. For sample KS5 batch, quantitative chemical analyses indicate 0.720% dolomite, 33.84% halite, 50.56% kainite, and 12.37% carnallite. Semi-quantitative X-ray powder diffraction analyses show that the RS_batch samples (RS3, RS4) are monomineralic, consisting of 100% halite, whereas KS5_batch is composed of 76.8% kainite and 23.2% halite. The discrepancy between analytical methods reflects the inherent compositional heterogeneity of the layered kainite-halite assemblage, combined with differences in sampling volume and analytical sensitivity. In particular, minor phases such as carnallite and leonite occur as spatially heterogeneous intergranular domains that may be over- or under-represented depending on the analytical technique and scale of measurement, rather than indicating hydrogen-induced mineralogical change.

3.3.3 Post-exposure µCT analysis of sample KS5_batch

Following cyclic hydrogen injection and withdrawal, sample KS5_batch was imaged by synchrotron µCT. The µCT-derived porosity of KS5_batch is substantially lower than that of RS1. Direct voxel counting in Avizo yields $\varphi\_CT = 0.057\%$; independent stereological point-counting returns a higher estimate of $0.106 \pm 0.032\%$ (95% CI), adopted as the reference value because it better captures partial-volume voxels at pore margins. Of the 15 683 labelled objects, 933 exceed eight voxels, with a median equivalent diameter of 70 µm, a mean anisotropy of 0.85 (88% exceeding 0.7) and a mean flatness of 0.41, indicating thin, planar, fracture-like features (Table 7).
The spatial distribution of porosity along the vertical sample axis is markedly heterogeneous and defines three distinct zones (Fig. 12a). The uppermost portion (approximately the first 2.6 mm) concentrates the majority of fracture-like objects, with a mean porosity of 0.24%. The central portion is largely intact ($\varphi \sim 0.07\%$), and the lowermost portion is the most consolidated ($\varphi \sim 0.03\%$). The dominant structural feature is a single fracture at Z~271, with an equivalent diameter of approximately 440 µm and an aspect ratio of 14.3. Critically, no pore object traverses the sample continuously along the main flow axis, confirming the absence of a through-going axial pathway. The median diameter corresponds to ~3.2 voxels at the 22.0 µm voxel size and therefore lies just above the partial-volume resolution limit identified in §2.4.2; the volumetric distribution is, however, dominated by larger features, in particular the 440 µm transgranular fracture at Z ~ 271 (~20 voxels), which are fully resolved.
Volumetric rendering of the segmented phases further reveals the crystalline fabric of the kainite-halite matrix. Grain-boundary discontinuities are visible as dark linear features on the reconstructed surface, delineating euhedral to sub-euhedral crystal domains of variable attenuation (Fig. 12b). A dense accessory phase occupies approximately 1.3% of the sample volume and occurs preferentially along grain boundaries.

Table 7. Summary of µCT-derived pore-structure parameters for samples RS1 (pre-exposure) and KS5_batch (post-exposure). Objects filtered to ≥ 8 voxels.

Parameter	RS1 (pre)	KS5_batch (post)
φ_CT (%)	2.13	0.106 ± 0.032
Total objects (≥ 8 voxels)	1 989	933
Median equiv. diameter (µm)	151	70
Mean anisotropy	0.86	0.85
Mean flatness	0.33	0.41
Largest object (% total pore vol.)	78.8	—
Objects touching boundary (%)	9.2	5.7
Through-going axial connectivity	Yes	No

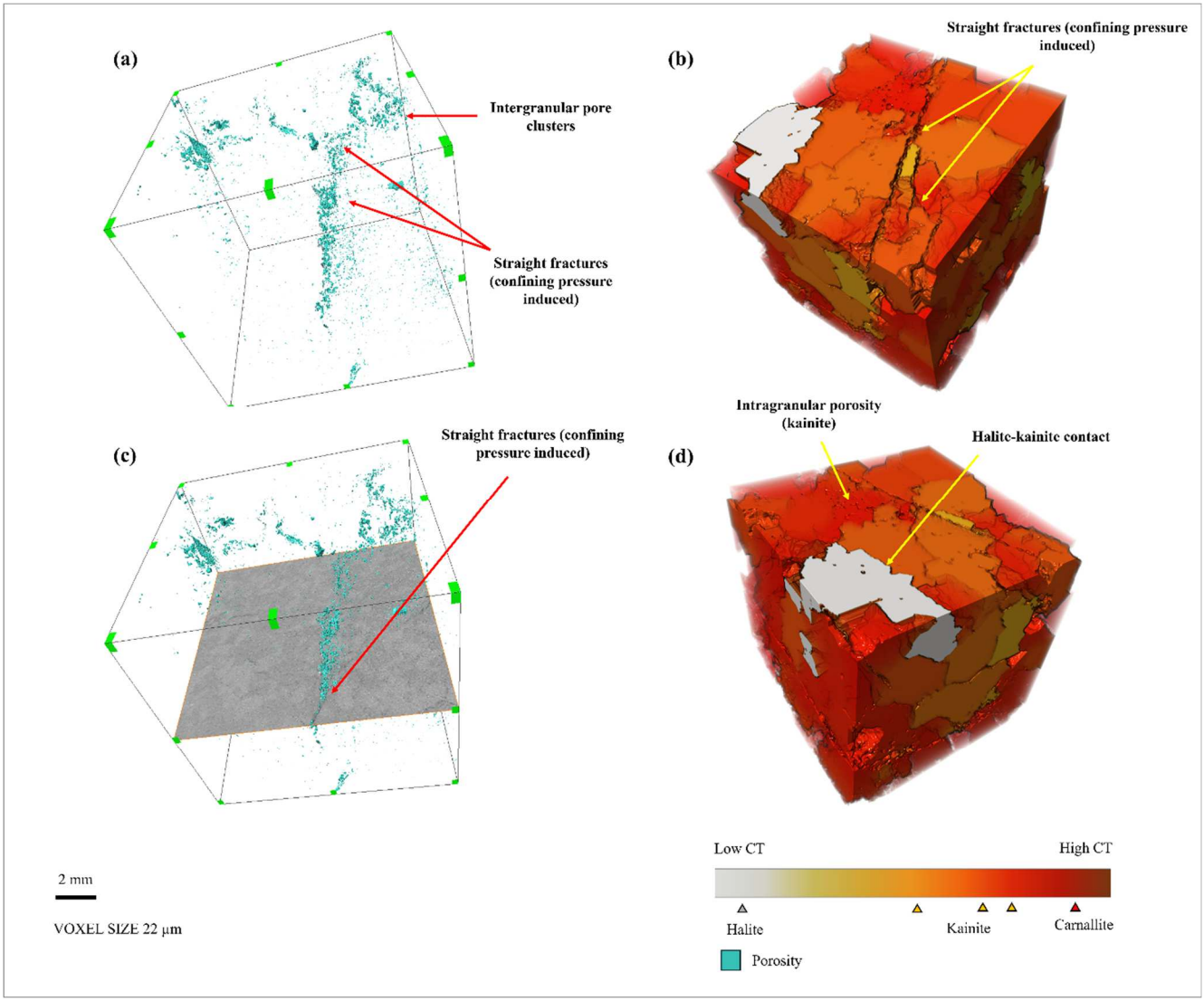

Fig.12. Three-dimensional µCT renderings of sample KS5_batch acquired at synchrotron after static H_2 exposure (10 MPa, 20 °C, 120 h; voxel size 22 µm). (a) Segmented porosity (cyan) within the bounding box; pore objects align along a sub-vertical discontinuity traversing the core. (b) Volume rendering with density-mapped colour scale: halite (white-grey), kainite-carnallite matrix (orange to dark red-brown); a prominent fracture crosscuts the core (arrow). (c) Orthoslice with porosity overlay confirming pore localisation along the fracture trace. (d) Alternative view highlighting the halite-kainite contacts and the textural heterogeneity of the polyphase matrix. φ_µCT = 0.106%; combined with the sub-µCT MIP contribution (§3.3.6), the total porosity estimate is approximately 1.26%, of which the µCT-resolved component represents ~8%.

3.3.4 Porosity evolution after hydrogen exposure: pre- vs. post-batch MIP

Post-batch MIP analyses were performed on three samples (RS3, RS4 and KS5) following the static hydrogen batch experiment (10 MPa, 20°C, 120 h). Comparative parameters are summarised in Table 8 and illustrated in Figs. 13-15, with the pre- vs. post-batch PSD shown in Fig. 13.
The dataset indicates a heterogeneous but internally coherent pattern of microstructural reorganisation. Three behavioural groups are identified on the basis of the combined evolution of Ø and TPS.

Table 8. Pre- vs. post-batch MIP comparison. Ø = total porosity; TPS = total pore surface area. Pore class shift: redistribution among sub (<1 µm), micro (1-8 µm) and macroporosity (>8 µm) domains.

Sample	Pre Ø (%)	Post Ø (%)	Pre TPS (m^2/g)	Post TPS (m^2/g)	ΔTPS (%)
KS5	1.22	1.27	1.906	1.234	–35
RS3	3.11	1.85	1.205	1.974	+64
RS4‡	4.66‡	2.93	2.327	1.859	–20

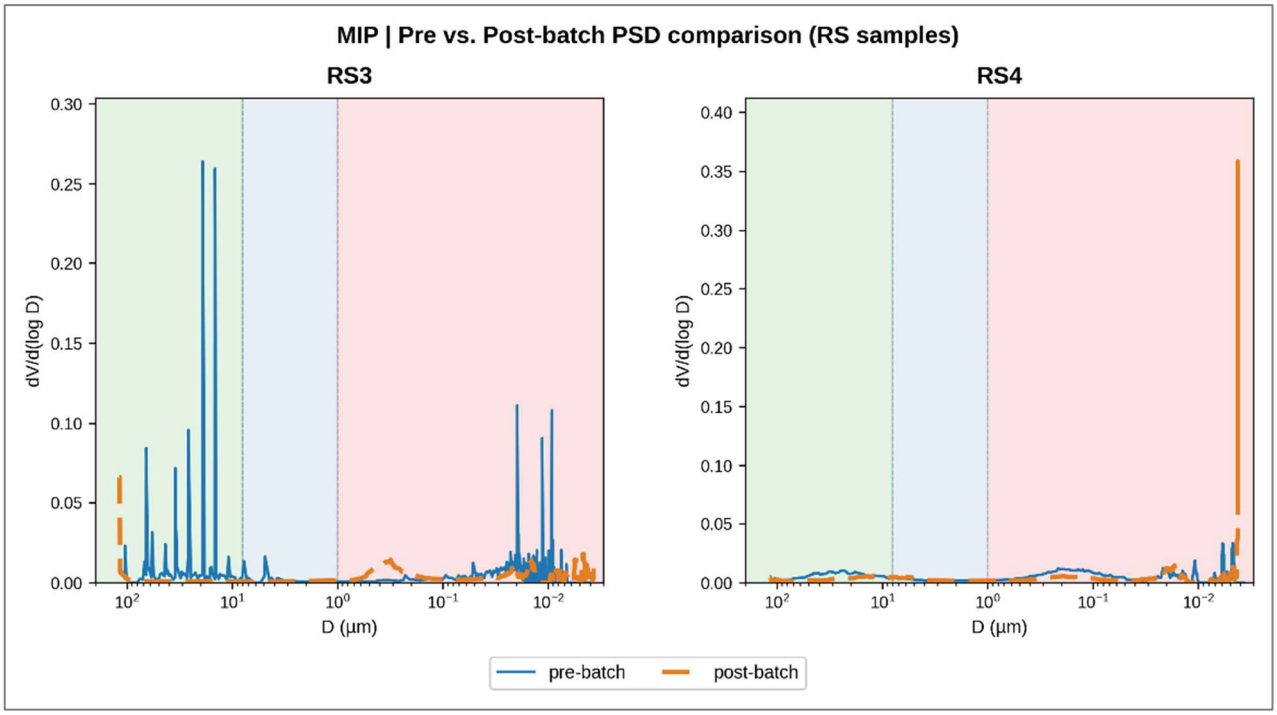

Fig. 13. Sample-by-sample comparison of pre-batch (solid blue line) and post-batch (dashed orange line) pore size distributions for RS samples with batch counterparts. RS3 displays pore refinement (Group C: modal shift to finer diameters). RS4 is subject to intra-core variability caveats (Group D).

Group A: Pore refinement (RS3)

RS3 shows a decrease in Ø (3.11% → 1.85%; ΔØ = -1.26%) (Figs. 13-14), coupled with an increase in TPS (1.205 → 1.974 m^2/g; +64%) and a reduction in modal pore diameter (~0.047 → ~0.026 µm). This combination, lower pore volume but higher surface area, indicates pore subdivision: larger pores are partially infilled or collapse, while finer pores develop at crystal contacts. The pre-batch PSD was

macropore-dominated (modal D = 19.11 µm), making the sample particularly sensitive to pore reorganisation during brine redistribution.

Group B: Intra-core variability (RS4)

RS4 exhibits a decrease in Ø from 4.66% (pre-batch aliquot) to 2.93% post-batch (ΔØ = -1.73%), accompanied by a moderate TPS reduction (2.327 → 1.859 m²/g; -20%) and a shift in modal pore diameter toward sub-porosity. However, pre- and post-batch analyses were conducted on different core portions, and the observed ΔØ likely reflects natural heterogeneity rather than a hydrogen-induced effect. This is consistent with µCT observations showing isolated sub-circular pores (60-200 µm) and partially sealed microfractures within an otherwise homogeneous halite matrix.

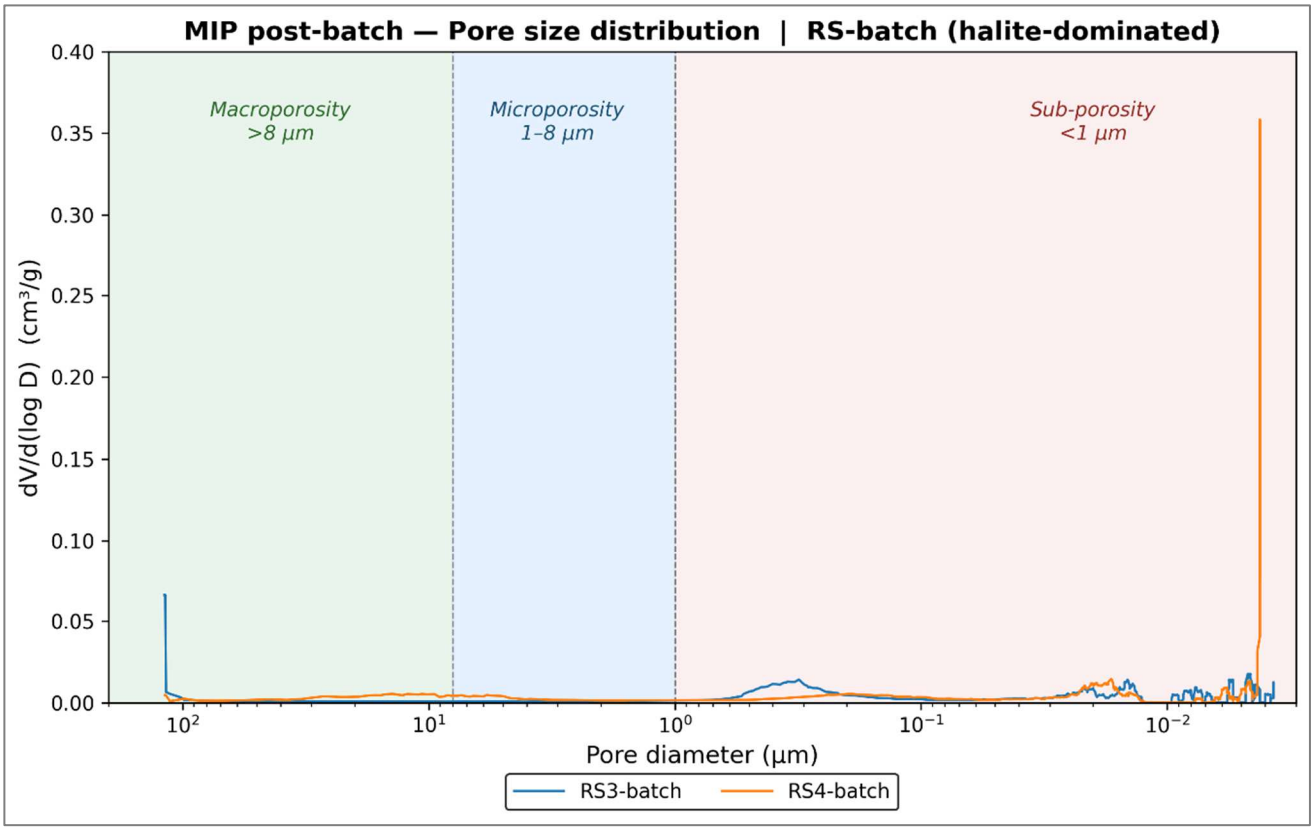

Fig.14. Pore size distribution of post-batch halite-dominated samples after static hydrogen exposure (10 MPa, 20°C, 120 h). Comparison with Fig. 13 reveals a general attenuation of individual PSD peaks, indicative of pore network homogenization.

Group C: Quasi-stable response (KS5)

The kainite-bearing sample KS5 shows the smallest absolute variation in total porosity (1.22% → 1.27%; ΔØ = +0.05%) and a significant TPS decrease (1.906 → 1.234 m²/g; ΔTPS = -35%). PSD analysis indicates a reduction in macro- and microporosity and a concurrent increase in sub-porosity (Fig. 15). This redistribution of porosity toward finer pore classes (<1 µm), at near-constant total porosity, is consistent with recrystallisation at kainite grain boundaries under static hydrogen pressure and with the development of sub-micrometric pores at crystal defects, in line with observations by Du et al. (2023) for halite under confinement. MIP-derived bulk-density values are not used in this

comparison: as they are obtained from the mercury-envelope volume of the individual fragment analysed, they are sensitive to fragment geometry and loaded mass and do not provide a reliable measure of pre- versus post-exposure densification. It should also be noted that KS5 was subjected to a dynamic injection test, so its response reflects combined chemical and mechanical effects; direct comparison with RS samples is therefore limited.

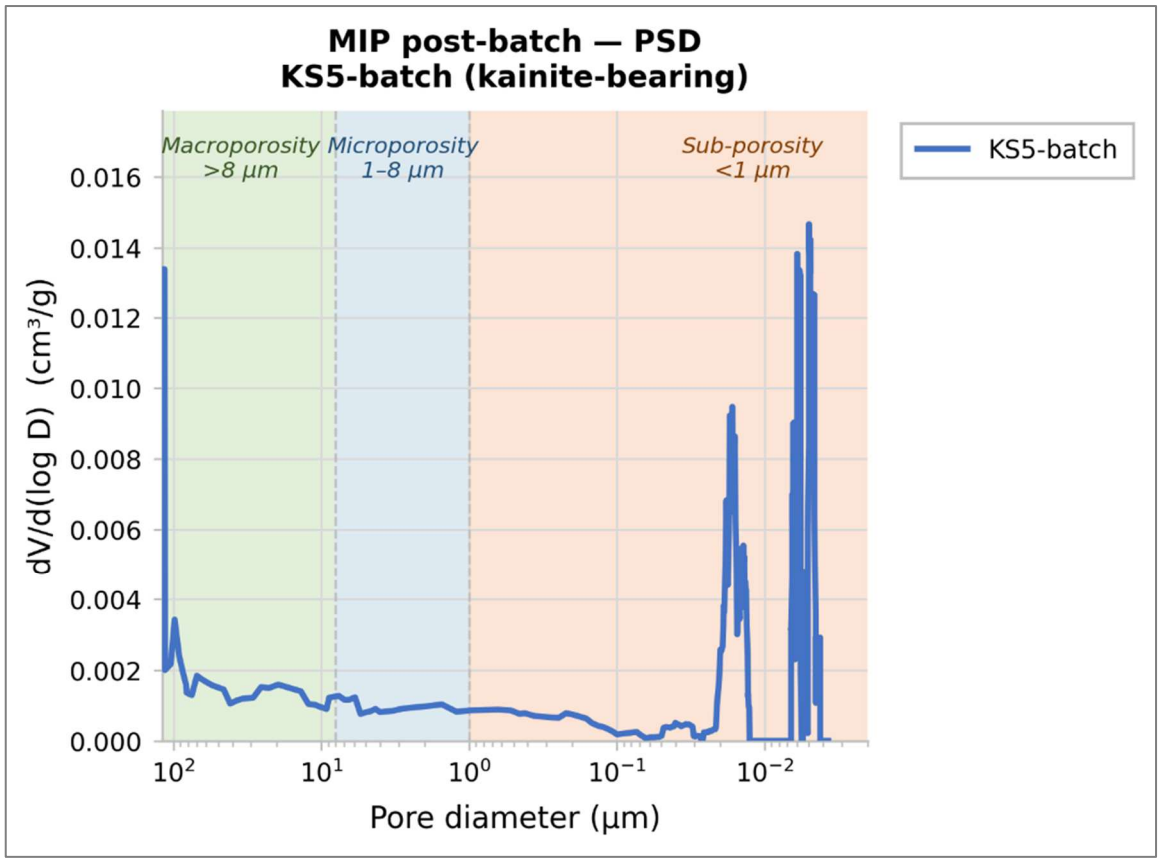

Fig.15 Post-batch PSD of sample KS5_batch (kainite-bearing; 10 MPa H_2, 20 °C, 120 h). The distribution is strongly dominated by sub-porosity (D < 1 µm), with a modal pore-throat diameter of approximately 5.5 nm and secondary peaks in the 0.02-0.05 µm range. A subordinate macroporosity component (D > 8 µm) is present but volumetrically minor. Background shading indicates the three pore-size domains after Chen et al. (2018). Total post-batch porosity is 1.27%, virtually unchanged from the pre-exposure value (1.22%).

3.3.5 Geochemical modelling (PHREEQC)

Thermodynamic equilibrium and kinetic simulations were performed using PHREEQC v.3.8.6 (Parkhurst and Appelo, 2013) to assess the stability of halite-kainite mineral assemblages in the presence of hydrogen and brine under conditions representative of subsurface storage caverns (90 °C, 8.9 MPa). These differ from the laboratory conditions (20 °C, 10 MPa) and were selected to reflect deeper subsurface environments. Input parameters and full outputs are provided in Supplementary Material S10.

Halite-brine-H_2 static system

A simplified equilibrium model including halite (NaCl), hydrogen gas and saturated brine shows that halite remains stable (SI = -0.0044), confirming brine saturation. No dissolution or precipitation

occurs. Hydrogen solubility is negligible (2.07×10^{-7} mol/kgw), with mildly reducing conditions (Eh = -0.371 V) and stable pH (6.3). No redox reactions or secondary mineral formation are observed. Overall, the system shows no significant geochemical evolution under static conditions.

Halite-kainite-brine-H_2 static system

Including kainite ($KMgClSO_4 \cdot 2.75H_2O$) does not significantly alter system behaviour. Halite and kainite remain near equilibrium (SI = 0.00 and –0.014), hydrogen solubility remains extremely low (1.42×10^{-7} mol/kgw), and redox and pH conditions are unchanged. Minor kainite dissolution releases Mg^{2+} and SO_4^{2-}, but no secondary minerals form. The system remains chemically stable.

Time-dependent evolution over one month

Kinetic modelling over 2.6×10^6 s confirms negligible mineral dissolution and stable fluid composition. Major ion concentrations remain constant, no new phases precipitate, and aqueous hydrogen remains unchanged (~1.40×10^{-7} mol/kgw). pH and Eh are stable, indicating no redox evolution (Supplementary Material S10, Table S5).
Overall, the simulations demonstrate that, over a one-month time frame, no detectable mineralogical or geochemical evolution occurs under the modelled storage conditions, and hydrogen remains geochemically inert in contact with both halite and kainite assemblages.

3.3.6 Multi-scale pore characterisation: µCT, MIP and mineralogical integration

µCT and MIP provide complementary views of the pore system. µCT resolves pores and fractures above the voxel size (22-31 µm), whereas MIP captures the connected pore-throat distribution down to ~4 nm but lacks spatial resolution. Integrating both datasets with petrographic and mineralogical observations allows a more complete characterisation of porosity and connectivity.

RS1 (pure halite). MIP yields a total connected porosity of 3.986% (Table 4), with a modal pore-throat diameter of 13.8 µm and a median of 0.068 µm. The µCT-derived porosity is 2.13%. The two techniques probe complementary aspects of the pore network across overlapping but distinct size domains: at the RS1 voxel size of 30.98 µm, µCT reliably resolves features above ~93 µm (3 voxels, accounting for partial-volume effects), whereas MIP records throats from ~4 nm up to ~300 µm. The MIP cumulative pore-size distribution shows that only 0.246% out of 3.986% total porosity is associated with throats ≥ 93 µm, meaning that 3.74% of the porosity is associated with throats finer than the µCT resolution. A more rigorous estimate of total porosity is therefore obtained by combining the µCT-visible porosity with the sub-µCT MIP contribution: $\varphi_{total} \sim \varphi_{\mu CT} + \varphi_{MIP}(D < 93\ \mu m) \sim 2.13\% + 3.74\% = 5.87\%$. This represents a lower-bound estimate of total porosity, as it does not account for disconnected porosity below the µCT resolution (inaccessible to mercury); the construction of the additive scheme, combining $\varphi_{\mu CT}$ with the strictly sub-µCT MIP fraction (D < 93 µm), excludes by definition any overlap in the throat-size domain between the two techniques. The relative weight of the two terms captures the dual architecture of RS1: a µCT-resolved fracture network at grain boundaries (78.8% of segmented pore volume; mean anisotropy 0.86) coexists with a finer, MIP-accessible throat system dominated by sub-micrometre features (median throat diameter 0.068 µm). Thin-section observations confirm abundant fluid inclusions and intergranular brine along halite grain boundaries, consistent with the unresolved nano-scale fraction. Anhydrite (3.8% by

XRPD), observed as acicular aggregates, shows no clear spatial correlation with the pore network and appears mechanically passive (Supplementary Material S5, Fig. S4).

KS5_batch (kainite-halite). MIP yields a total connected porosity of 1.22%, with a modal pore-throat diameter of 5.5 nm and dominance of sub-micrometre throats (58%). The µCT-derived porosity (0.106%) is an order of magnitude smaller. At the 22.0 µm voxel size, µCT resolves features above ~66 µm (3 voxels); the MIP cumulative distribution shows that only 0.064% of porosity is associated with throats ≥ 66 µm, meaning that more than 94% of connected porosity resides below the µCT resolution limit. Combining the µCT-visible porosity with the sub-µCT MIP contribution yields a total porosity estimate of φ_total ~ φ_µCT + φ_MIP(D < 66 µm) ~ 0.106% + 1.15% = 1.26%, with the µCT-resolved component representing only ~8% of total porosity. The pore system is therefore dominated by grain-boundary films and crystal defects at the nanometre scale, with localised µCT-visible features corresponding to fracture-like discontinuities within mechanically weaker zones.

Petrography confirms a layered kainite-halite fabric with intergranular brine and complex mineral interfaces (including carnallite and leonite). This mineralogical heterogeneity promotes a finer and more complex pore network compared to halite-dominated samples.

Post-exposure MIP data show negligible change in total porosity (1.22% → 1.27%), but a decrease in median pore size (1.71 → 0.57 µm) and TPS (-35%). These trends indicate selective closure of intermediate pores (1-8 µm) with preservation of fine-scale porosity below µCT resolution.

Table 9. MIP-derived porosity parameters before and after H_2 exposure. Since RS1 was not subjected to batch reaction, RS3_batch, a compositionally equivalent halite-dominated sample, is used as proxy for post-exposure comparison. TPS = total pore surface area.

Parameter	RS1 pre	Halite proxy post	KS5 pre	KS5_batch
φ_MIP (%)	3.99	3.11	1.22	1.27
Modal D (µm)	13.8	19.1	0.006	0.005
Median D (µm)	0.068	0.068	1.71	0.57
TPS ($m^2\ g^{-1}$)	3.05	—	1.91	1.23
ρ_bulk ($g\ cm^{-3}$)	2.132	2.180	1.935	2.127

4. Discussion

4.1. Mineralogical and microstructural controls on pore architecture

The multi-scale characterisation demonstrates a strong mineralogical control in the Realmonte evaporites, particularly within the halite-kainite layering. This control is evident across the entire analytical range, from micro-CT imaging to the nanometre-scale pore throats resolved by MIP.
In the pure halite sample (RS1), micro-CT imaging shows that 78.8% of the segmented pore volume occurs within a single connected fracture network aligned along grain boundaries (Fig. 6). The pore population is dominated by highly anisotropic planar objects, consistent with sub-planar fractures propagating along halite contacts. As detailed in §3.3.6, the two techniques resolve complementary domains of the pore network: µCT captures the connected fracture system above its resolution limit, while MIP additionally accesses the sub-resolution throat population dominated by submicrometre

features. The combined estimate shows that the µCT-resolved fracture network accounts for only a third of the total porosity, the remaining two-thirds residing in the unresolved grain-boundary domain documented petrographically. This dual partitioning is fundamental for the transport interpretation: while the connected fracture network defines the µCT-visible pathways, the sub-resolution throat system controls the effective gas transport regime (see §4.3). Petrography shows two-phase fluid inclusions and intergranular brine along grain boundaries, indicating that the fracture network is sustained by residual fluids at crystal contacts, consistent with brine-assisted deformation in halite (e.g. Urai et al., 1986; Desbois et al., 2012).

The kainite-bearing sample KS5_batch exhibits a fundamentally different pore architecture. As detailed in §3.3.6, the combined µCT + MIP analysis yields a total porosity estimate of approximately 1.26%, of which the µCT-resolved component represents only ~8%. More than 94% of the connected porosity resides below the µCT resolution limit, with throats dominated by sub-micrometre features (modal diameter 5.5 nm). Micro-CT reveals vertical heterogeneity, with porosity decreasing from 0.24% in the upper portion of the sample to 0.03% at its base. The decrease in the µCT-resolved fraction ($\varphi_{\mu CT}/\varphi_{total}$ ~ 0.08 in KS5 versus 0.36 in RS1) reflects a systematic shift toward finer, grain-boundary-controlled pore systems with increasing mineralogical complexity. Petrographic data indicate microstructural modification at the crystal scale. In pre-exposure samples, kainite crystals range from 83 to 402 µm, whereas post-exposure crystals range from 100 to 308 µm. This narrowing of the crystal-size distribution is consistent with recrystallisation driven by pressure-solution processes and brine redistribution during pressurised hydrogen exposure conditions.

4.2. Geochemical stability of halite and kainite under hydrogen exposure

Mineralogical, geochemical and thermodynamic evidence indicates that neither halite nor kainite undergoes measurable reactions with molecular hydrogen under the experimental conditions tested (10 MPa H_2, 120 h, ambient temperature), within the resolution of the applied methods. XRPD patterns of post-batch samples are indistinguishable from those of the original material, ICP-OES elemental balances show only minor variations attributable to natural heterogeneity, and no dissolution-precipitation of new phases is observed. PHREEQC simulations confirm that hydrogen remains essentially inert in the highly saline brines characteristic of the Realmonte evaporites: halite and kainite saturation indices remain near equilibrium and redox conditions are only minimally affected by dissolved H_2.

These results align with previous studies. No mineralogical alteration has been reported in halite or anhydrite exposed to hydrogen at elevated pressure and temperature (Fatah et al., 2024), only minor recrystallisation in rock salt (Kovács et al., 2025), and no abiotic redox reactions in Zechstein halite (Emmel et al., 2025). Hydrogen loss in impure salts is also predicted to be minimal over long timescales (Yuan et al., 2025a, b). While no mineralogical or chemical reactions are detected, petrographic and porosimetric data indicate localised dissolution-reprecipitation processes mediated by brine redistribution, suggesting that hydrogen exposure may indirectly influence microstructural evolution through fluid mobilisation rather than direct mineral-gas reactions.

This study extends those findings to kainite-bearing systems. Kainite, a hydrated sulphate-chloride double salt with a monoclinic structure, differs fundamentally from halite and cannot be assumed to behave similarly. Here, it remains stable under hydrogen exposure, with no evidence of dissolution, dehydration or phase transformation. This fills a key gap in the experimental database.

This stability has direct implications for storage: chemically inert wall rock minimises both gas contamination and mechanical weakening. Although kainite remained geochemically stable in the

intact rock matrix under the tested conditions, its behaviour during the solution-mining phase warrants consideration. Kainite dissolution during cavern creation would release Mg^{2+}, SO_4^{2-} and K^+ into the sump brine, providing substrates for potential microbial sulphate reduction even in the absence of discrete sulphate interbeds (Hemme and van Berk, 2018; Dopffel et al., 2021; Minougou et al., 2024). In the intact wall rock, however, the common-ion effect (Cl^- shared between halite and kainite) and the low permeability of the interlocking kainite-halite matrix effectively suppress kainite dissolution, consistent with the near-equilibrium saturation index returned by PHREEQC modelling (SI = -0.014). The geochemical consequences of sulphate supply from kainite for long-term gas purity were not addressed in the present abiotic experiments and require investigation under biotic conditions. Diffusive transport modelling of H_2S generation at the gas-brine interface (Minougou et al., 2024) suggests that microbial sulphate reduction can become significant over operational time scales when sulphate availability and microbial activity coincide, an important consideration for kainite-bearing storage formations.

4.3. Pore network reorganisation and permeability behaviour under hydrogen cycling

Pre- and post-batch MIP data shows that exposure under pressurised hydrogen conditions modifies the pore size distribution, while leaving bulk porosity largely unchanged. Petrography suggests a mechanism consistent with brine redistribution. Under pressure, interstitial brines migrate along grain boundaries and into crystals, consistent with local dissolution. During pressure release, supersaturation leads to halite reprecipitation, often as cryptocrystalline aggregates that partially obscure original grain boundaries. This dissolution-reprecipitation cycle redistributes pore space and provides a plausible explanation for the observed pore network evolution. The absence of any mineralogical or geochemical difference between pre- and post-exposure samples, documented by XRPD, ICP-OES and SEM-EDS, indicates that the observed microstructural reorganisation is primarily driven by pressure-mediated brine redistribution rather than by chemical interactions specific to molecular hydrogen. Hydrogen itself does not cause mineral reactions under the tested conditions; the injection pressure mobilises interstitial fluids and triggers localised dissolution-reprecipitation, with cycling enhancing the effect through transient grain-boundary dilation and viscoplastic recovery.

In the kainite-bearing sample KS5, the response differs markedly. Bulk porosity remains nearly constant (1.22-1.27%), and the modal pore diameter remains ~5 nm, but the median pore diameter decreases from 1.71 µm to 0.57 µm. Total pore surface area decreases by 35% (1.91 → 1.23 $m^2\ g^{-1}$). These changes indicate selective closure of intermediate-sized pores (1-8 µm) accompanied by preservation of the finest grain-boundary porosity. Mechanically, this behaviour reflects creep-driven reorganisation of the grain-boundary network under confining pressure, consistent with the well-known self-healing capacity of rock salt.

Hydrogen injection experiments provide direct constraints on permeability. Under seasonal cycling conditions permeability is $K = 3.48 \times 10^{-21}$ m^2, increasing to $K = 2.46 \times 10^{-20}$ m^2 during rapid monthly cycling. Both values fall within or slightly above the range reported for intact rock salt and remain several orders of magnitude below the permeability threshold proposed to limit hydrogen losses below 1%. The ~7-fold increase during rapid cycling reflects the balance between transient damage (grain-boundary dilation) and viscoplastic healing. Short loading intervals temporarily enhance permeability, but creep rapidly restores sealing capacity. The presence of kainite may locally increase stress concentrations, explaining slightly higher permeability relative to halite-dominated samples

(RS-series) without compromising overall sealing behaviour. The absence of a through-going pathway at the µCT scale indicates that flow is controlled by sub-resolution grain-boundary networks, consistent with the low but measurable permeability derived from pressure-decay analysis.

4.4. Implications for underground hydrogen storage in heterogeneous Messinian formations

The combined datasets, from micro-CT imaging, MIP analysis, batch reaction experiments, thermodynamic modelling and cyclic injection provide a consistent assessment of the Realmonte evaporites as hydrogen storage hosts.

First, both halite and kainite remain geochemically stable under hydrogen exposure. No mineral-gas reactions are detected, within the resolution of the applied methods under reservoir conditions, and thermodynamic modelling suggests that this stability may persist across a range of conditions. This is particularly significant for kainite, given its hydrated sulphate-chloride structure.

Second, permeability measurements on the kainite-bearing lithology (3.48×10^{-21} to 2.46×10^{-20} m²) indicate sealing properties comparable to those of halite-dominated rock salt reported in the literature even under cyclic loading conditions representative of hydrogen storage operations. Synchrotron micro-CT imaging of the post-injection KS5 sample further confirms that hydrogen-induced microstructural modifications remain spatially confined and do not generate connected pathways.

Third, kainite-bearing evaporites are characterised by low porosity (<1.5%) and low total pore surface area, indicating a compact, poorly connected pore system. These properties suggests that KS5 is representative of the lithology rather than anomalously tight. Demonstrating stability, low permeability and nanometre-scale porosity without macroscopic connectivity extends the range of evaporite formations suitable for hydrogen storage. Halite-dominated samples provide the reference framework against which the kainite-bearing system can be evaluated.

Several limitations remain. Experiments were abiotic and do not address microbial sulphate reduction (cf. §4.2); systematic biotic experiments under realistic temperature and salinity conditions are a priority for future studies. The cyclic hydrogen injection test was performed on a single representative kainite-bearing sample (KS5). Although no evidence of geochemical reactivity was observed, further tests on additional samples are required to robustly constrain the variability of the kainite-bearing lithology in the mine. X-ray CT cannot resolve the nanometre-scale porosity controlling transport in kainite-bearing samples; higher-resolution techniques (e.g. cryo-FIB-SEM) are required. Finally, long-term creep behaviour under cyclic loading at in situ temperatures remains to be quantified.

Despite the above limitations the integration of mineralogical, petrophysical and experimental datasets provides a consistent framework for evaluating the behaviour of kainite-bearing evaporites under hydrogen exposure. As observed on other impure halite samples (Fatah et al. 2024, Kovács et al. 2025 and Emmel et al. 2025) across all analyses, no measurable mineral-gas reactions are detected within the resolution of the applied methods, indicating geochemical stability of both halite and kainite under the tested abiotic conditions. However, microstructural and porosimetric data reveal localised pore-network reorganisation consistent with brine redistribution and dissolution-reprecipitation processes at grain boundaries. These observations indicate that system behaviour is governed primarily by fluid-mediated processes under pressure, rather than by direct hydrogen-mineral interactions. The combined µCT and MIP datasets further demonstrate that pore connectivity is dominated by sub-resolution grain-boundary networks, reconciling the absence of through-going pathways at the imaging scale with the low but measurable permeability observed during cyclic injection tests. Taken together, these results provide the first experimental evidence supporting the suitability of heterogeneous Messinian evaporites, including kainite-bearing units, as potential host

formations for underground hydrogen storage, while highlighting the importance of multi-technique characterisation in resolving their transport behaviour.

5. Conclusions

This study presents the first integrated, multi-scale characterisation of Messinian evaporites from the Realmonte Mine (Sicily) in the context of underground hydrogen storage. By combining µCT imaging, mercury intrusion porosimetry, X-ray powder diffraction, petrography, whole-rock and trace-element geochemistry, batch experiments under H_2 pressure, PHREEQC modelling, and cyclic injection tests, it systematically evaluates the mineralogical, geochemical, microstructural and petrophysical behaviour of a heterogeneous halite-kainite succession.

The main conclusions are:

- *Halite and kainite exhibit geochemical stability under the tested abiotic hydrogen exposure conditions.* Batch experiments (10 MPa H_2, 120 h) show no mineralogical alteration, no secondary phase formation, and no significant changes in bulk composition. PHREEQC modelling indicates that both minerals remain near equilibrium across realistic brine compositions and hydrogen pressures, with negligible redox effects. These results are consistent with previous studies on rock salt and extend them to kainite, for which no prior H_2 interaction data existed.
- *Exposure under pressurised hydrogen conditions induces physical reorganisation of the pore network rather than chemical transformation.* Post-batch MIP data show systematic shifts in pore-size distributions. In RS3, the pre-batch pore-size distribution was macropore-dominated (modal D = 19.1 µm) and shifts post-batch toward sub-porosity (modal D ~0.026 µm), with a concurrent reduction in total porosity (3.11% → 1.85%), indicating redistribution toward finer pore throats. In KS5_batch, intermediate pores (1-8 µm) close selectively while nanometre-scale porosity is preserved; total pore surface area decreases by 35% (1.91 → 1.23 $m^2\ g^{-1}$), consistent with creep-driven reorganisation of the grain-boundary network.
  Petrography confirms that these changes result from pressure-driven brine redistribution and recrystallisation, not from H_2- mineral reactions.
- *The kainite-halite assemblage maintains very low permeability under cyclic hydrogen injection.* Permeability values of 3.48×10^{-21} m^2 (seasonal cycling) and 2.46×10^{-20} m^2 (monthly cycling) fall within or slightly above the range for intact rock salt and remain several orders of magnitude below thresholds for significant gas loss. The ~7-fold increase under rapid cycling reflects transient grain-boundary dilation during frequent pressure changes, followed by viscoplastic healing. Synchrotron µCT confirms that microstructural modifications remain localised and do not generate connected flow pathways.
- *Heterogeneous Messinian evaporites, including kainite-bearing units, provide a viable host lithology for underground hydrogen storage.* This study provides the first experimental constraints on kainite in a storage context, addressing a major gap in the literature. Despite its distinct mineralogy, kainite does not appear to introduce substantially different behaviour relative to halite: it remains chemically stable, hosts a tight nanometre-scale pore system, and does not develop macroscopic connectivity under hydrogen cycling. Given that the Realmonte Messinian succession contains kainite interbeds up to 18 m thick, these results provide the

first experimental evidence that heterogeneous Messinian evaporites, including kainite-bearing units, can be considered as potential host formations for underground hydrogen storage.

Acknowledgements:

The authors gratefully acknowledge ITALKALI for providing access to the geological and mining data of the Realmonte mine. Special thanks are due to Eng. Cristian Sabatino (Director of the Realmonte Mine) and Eng. Michele Simili for their continuous support, open collaboration, and availability throughout all phases of this research. The authors are grateful to Prof. Kate Dobson (University of Strathclyde, Glasgow) for acquiring the synchrotron X-CT data on sample KS5_batch at the Diamond-Manchester Imaging Branchline (Diamond Light Source, Harwell), as received. The authors also thank Schlumberger for providing an academic license for Petrel software. This research was supported by the Italian National Operational Programme (PON) "Research and Innovation" 2014-2020, Action IV "Doctorates on Green Topics" (CUP E65F21003740003). Additional support for this work was provided through the Research Agreement between DiSTAR and the Regional Park Authority "Riviera di Ulisse" (CUP J66C22000610006). The authors further acknowledge the Gustavus E. Archie Memorial Grant.

References

AbuAisha, M., & Billiotte, J. (2021). A discussion on hydrogen migration in rock salt for tight underground storage with an insight into a laboratory setup. Journal of Energy Storage, 38, 102589. https://doi.org/10.1016/j.est.2021.102589

Altomare, A., Corriero, N., Cuocci, C., Falcicchio, A., Moliterni, A. and Rizzi, R. (2015) QUALX2.0: qualitative phase analysis software using the freely available database POW_COD. Journal of AppliedCrystallography, 48, 598-603. https://doi.org/10.1107/S1600576715002319

Bérest, P., & Brouard, B. (2003). Safety of salt caverns used for underground storage. Oil & Gas Science and Technology, 58(3), 361–384. https://doi.org/10.2516/ogst:2003023

Blancone, D., Ruiz Maraggi, L. M., Cardozo, N., Moscardelli, L., & Escalona, A. (2025). Assessing hydrogen storage potential in Zechstein salt caverns of the Norwegian North Sea. Journal of Energy Storage, 128, 117032. https://doi.org/10.1016/j.est.2025.117032

Blunt, M. J., Bijeljic, B., Dong, H., Gharbi, O., Iglauer, S., Mostaghimi, P., Paluszny, A., & Pentland, C. (2013). Pore-scale imaging and modelling. Advances in Water Resources, 51, 197-216. https://doi.org/10.1016/j.advwatres.2012.03.003

Borisov, A. S., Siidra, O. I., Ugolkov, V. L., Kuznetsov, A. N., Firsova, V. A., Charkin, D. O., Pekov, I. V. (2022). Complex hydrogen bonding and thermal behaviour over a wide temperature range of kainite KMg(SO4)Cl·2.75H2O. Mineralogical Magazine, 86(1), 37-48. doi:10.1180/mgm.2021.101

Brouard, B., Bérest, P., & Karimi-Jafari, M. (2001). Permeability of rock salt from short-duration and long-duration cavern tests. In Proceedings of the SMRI Fall Technical Conference, Albuquerque, NM.

Butler, R.W.H., Maniscalco, R., Sturiale, G. & Grasso, M. (2014). Stratigraphic variations control deformation patterns in evaporite basins: Messinian examples, onshore and offshore Sicily (Italy). Journal of the Geological Society doi:10.1144/jgs2014-024.

Caglayan, D. G., Weber, N., Heinrichs, H. U., Linßen, J., Robinius, M., Kukla, P. A., & Stolten, D. (2020). Technical potential of salt caverns for hydrogen storage in Europe. *International Journal of Hydrogen Energy*, *45*(11), 6793–6805. https://doi.org/10.1016/j.ijhydene.2019.12.161

Chen, J., Li, E., & Luo, J. (2018). Characterization of microscopic pore structures of rock salt through mercury injection and nitrogen absorption tests. Geofluids, 2018, Article 9427361. https://doi.org/10.1155/2018/9427361

Cipriani, M., Costanzo, A., Feely, M., Guido, A., D'Antonio, M., Vespasiano, G., Donato, S., Cianflone, G., Maruca, G., Apollaro, C., Alessandro, F., Perri, F., & Dominici, R. (2026). The Messinian halite facies: Insights into halite crystallisation and depositional environments using geochemical, petrographic and fluid inclusion studies. Geoscience Frontiers, 17, 102207. https://doi.org/10.1016/j.gsf.2025.102207

Cosenza, P., Ghoreychi, M., Bazargan-Sabet, B., & de Marsily, G. (1999). In situ rock salt permeability measurement for long term safety assessment of storage. International Journal of Rock Mechanics and Mining Sciences, 36(4), 509-526. https://doi.org/10.1016/S0148-9062(99)00017-0

Crotogino, F., Schneider, G.-S., & Evans, D. J. (2018). Renewable energy storage in geological formations. Proceedings of the Institution of Mechanical Engineers, Part A: Journal of Power and Energy, 232(1), 100–114. https://doi.org/10.1177/0957650917731181

Cui, X., Bustin, A. M. M., & Bustin, R. M. (2009). Measurements of gas permeability and diffusivity of tight reservoir rocks: different approaches and their applications. Geofluids, 9(3), 208-223. https://doi.org/10.1111/j.1468-8123.2009.00244.x

Cyran, K. (2021). The influence of impurities and fabrics on mechanical properties of rock salt for underground storage in salt caverns. A review. *Archives of Mining Sciences*, *66*(2), 155–179. https://doi.org/10.24425/ams.2021.137454

Decima, A., & Wezel, F. C. (1971). Osservazioni sulle evaporiti messiniane della Sicilia centro-meridionale. Rivista Mineraria Siciliana, 130–132, 172-187.

Desbois, G., Urai, J. L., Burkhardt, C., Drury, M. R., & Hayles, M. (2008). Cryogenic vitrification and 3D serial sectioning using high resolution cryo-FIB SEM technology for brine-filled grain boundaries in halite: First results. Geofluids, 8(1), 60-72. https://doi.org/10.1111/j.1468-8123.2007.00205.x

Desbois, G., Urai, J. L., & de Bresser, J. H. P. (2012a). Fluid distribution in grain boundaries of natural fine-grained rock salt deformed at low differential stress (Qom Kuh salt fountain, central Iran): Implications for rheology and transport properties. Journal of Structural Geology, 43, 128-143. https://doi.org/10.1016/j.jsg.2012.07.006

Desbois, G., Urai, J. L., Kukla, P. A., Konstanty, J., & Baerle, C. (2012b). Distribution of brine in grain boundaries during static recrystallization in wet, synthetic halite: Insight from broad ion beam sectioning and SEM observation at cryogenic temperature. Contributions to Mineralogy and Petrology, 163, 19–31. https://doi.org/10.1007/s00410-011-0656-x

Dopffel, N., Jansen, S., & Wildschut, J. (2021). Microbial side effects of underground hydrogen storage. Knowledge gaps, risks and opportunities for successful implementation. International Journal of Hydrogen Energy, 46(12), 8594-8606. https://doi.org/10.1016/j.ijhydene.2020.12.058

Du, N., Bornert, M., & Dimanov, A. (2023). 3D microscale investigation of active deformation mechanisms of halite under conditions representative of underground hydrogen storage. Proceedings of the SEG Annual Meeting 2023. https://doi.org/10.59490/seg.2023.636

Edlmann, K., Bensabat, J., Niemi, A., Haszeldine, R. S., & McDermott, C. I. (2016). Lessons learned from using expert elicitation to identify, assess and rank the potential leakage scenarios at the Heletz pilot CO2 injection site. International Journal of Greenhouse Gas Control, 49, 473–487. https://doi.org/10.1016/j.ijggc.2016.02.018

El Tabakh, M., Utha-Aroon, C., & Schreiber, B. C. (1999). Sedimentology of the Cretaceous Maha Sarakham evaporites in the Khorat Plateau of northeastern Thailand. Sedimentary Geology, 123, 31–62. https://doi.org/10.1016/S0037-0738(98)00083-9

Emmel, B., Cardozo, N., Soustelle, V., Zimmermann, U., Gawel, K., & Røyne, F. (2025). Zechstein halite behavior under hydrogen exposure: Implications for underground hydrogen storage in salt caverns. Energy & Fuels, 39(41), 19937-19949. https://doi.org/10.1021/acs.energyfuels.5c02535

Fatah, A., Bennour, Z., Ben Mahmud, H., Gholami, R., & Hossain, M. M. (2024). Surface reactivity and geological storage of hydrogen in depleted reservoirs: A comprehensive assessment of minerals. Fuel, 371, 131857. https://doi.org/10.1016/j.fuel.2024.131857

Grgic, D., Al Sahyouni, F., Golfier, F., Moumni, M., & Schoumacker, L. (2022). Evolution of gas permeability of rock salt under different loading conditions and implications on the underground hydrogen storage in salt caverns. Rock Mechanics and Rock Engineering, 55, 691–714. https://doi.org/10.1007/s00603-021-02681-y

Heinemann, N., Alcalde, J., Miocic, J. M., Hangx, S. J. T., Kallmeyer, J., Ostertag-Henning, C., … Strobel, G. (2021). Enabling large-scale hydrogen storage in porous media. The scientific challenges. Energy & Environmental Science, 14, 853-864. https://doi.org/10.1039/D0EE03536J

Hemme, C., & van Berk, W. (2018). Hydrogeochemical modeling to identify potential risks of underground hydrogen storage in depleted gas fields. Applied Sciences, 8(11), 2282. https://doi.org/10.3390/app8112282

Hsieh, P. A., Tracy, J. V., Neuzil, C. E., Bredehoeft, J. D., & Silliman, S. E. (1981). A transient laboratory method for determining the hydraulic properties of 'tight' rocks-I. Theory. International Journal of Rock Mechanics and Mining Sciences & Geomechanics Abstracts, 18(3), 245-252. https://doi.org/10.1016/0148-9062(81)90979-7

Isaji, Y., Yoshimura, T., Kuroda, J., Tamenori, Y., Jiménez-Espejo, F. J., Lugli, S., Manzi, V., Roveri, M., Kawahata, H., & Ohkouchi, N. (2019). Biomarker records and mineral compositions of the Messinian halite and K–Mg salts from Sicily. Progress in Earth and Planetary Science, 6, 60. https://doi.org/10.1186/s40645-019-0306-x

Kemp, S. J., Smith, F. W., Wagner, D., Mounteney, I., Bell, C. P., Sherlock, S. C., Sherwood, B. P., Sherrington, M. J., & Sherring, D. A. (2016). An improved approach to characterize potash-bearing evaporite deposits, evidenced in North Yorkshire, United Kingdom. Economic Geology, 111(3), 719-742. https://doi.org/10.2113/econgeo.111.3.719

Kolano, M., Szewczyk, J., & Jarzyna, J. A. (2024). Estimation of rock salt geomechanical parameters from well logs for underground hydrogen storage. Geoenergy Science and Engineering, 233, 212562.

Kovács, T., Cornejo, N. H., Macías, P. J. C., Bozal, C. P., & Alcalde, J. (2025). Preliminary laboratory studies on hydrogen storage in a salt cavern of the Eocene Barbastro Formation, Southern Pyrenees, Spain. Advances in Geosciences, 67, 15–24. https://doi.org/10.5194/adgeo-67-15-2025

Laban, M. (2020). Hydrogen storage in salt caverns: Chemical modelling and analysis of large-scale hydrogen storage in underground salt caverns [Master's thesis, Delft University of Technology].

Li, H., Ma, H., Zhao, K., Zhu, S., Liang, X., & Yang, C. (2021). Tightness assessment for underground gas storage caverns. Journal of Natural Gas Science and Engineering, 91, 103954. https://doi.org/10.1016/j.jngse.2021.103954

Lin, Q., Al-Khulaifi, Y., Blunt, M. J., & Bijeljic, B. (2016). Quantification of sub-resolution porosity in carbonate rocks by applying high-salinity contrast brine using X-ray microtomography differential imaging. Advances in Water Resources, 96, 306–322.

Lowenstein, T. K. (1988). Origin of depositional cycles in a Permian "saline giant": The Salado (McNutt Zone) evaporites of New Mexico and Texas. Geological Society of America Bulletin, 100, 592–608.

Luangthip, A., Jongpradist, P., Walsri, C., & Fuenkajorn, K. (2017). Effects of carnallite content on mechanical properties of Maha Sarakham rock salt. Arabian Journal of Geosciences, 10, 149. https://doi.org/10.1007/s12517-017-2945-9

Lugli, S., Schreiber, B. C., & Triberti, B. (1999). Giant polygons in the Realmonte Mine (Agrigento, Sicily): Evidence for the desiccation of a Messinian halite basin. Journal of Sedimentary Research, 69(3), 764–771. https://doi.org/10.2110/jsr.69.764

Lugli, S., Schreiber, B. C., & Triberti, B. (2002). Messinian halite and residual facies in the Caltanissetta Basin, Sicily. In B. C. Schreiber & M. El Tabakh (Eds.), Evaporites through space and time. Geological Society, London, Special Publications, 285, 43-63.

Macente, A., Vanorio, T., Miller, K. J., Fusseis, F., & Butler, I. B. (2019). Dynamic evolution of permeability in response to chemo-mechanical compaction. Journal of Geophysical Research: Solid Earth, 124(11), 11204–11218. https://doi.org/10.1029/2019JB017750

Martin-Clave, C., Ougier-Simonin, A., & Vanissorn, G. (2021). Impact of second phase content on rock salt rheological behavior under cyclic mechanical conditions. Rock Mechanics and Rock Engineering, 54, 5245–5267. https://doi.org/10.1007/s00603-021-02449-4

Minougou, J. D., Gholami, R., & Poirier, S. (2024). A one-dimensional diffusive transport model to evaluate H_2S generation in salt caverns hydrogen storage sites. *Gas Science and Engineering*, *126*, 205336. https://doi.org/10.1016/j.jgsce.2024.205336

Nassan, T., Minkley, W., & Staudtmeister, K. (2025). Underground hydrogen storage in salt caverns: Laboratory experiments to determine integrity of rock salt and wellbore through effective permeability measurements. International Journal of Hydrogen Energy, 99, 619-631. https://doi.org/10.1016/j.ijhydene.2024.10.088

Parkhurst, D. L., & Appelo, C. A. J. (2013). Description of input and examples for PHREEQC Version 3: A computer program for speciation, batch-reaction, one-dimensional transport, and inverse geochemical calculations (Techniques and Methods 6-A43). U.S. Geological Survey. https://doi.org/10.3133/tm6A43

Pichat, A., Célini, N., & Kergaravat, C. (2025). K-Mg salt distribution in the Zechstein Group of the Northern Permian Basin (UK and Norway). Interplays with the Southern Permian Basin and implications for salt cavern development. Geosphere, 21(1), 28-48. https://doi.org/10.1130/GES02785.1

Popp, T., Kern, H., & Schulze, O. (2001). Evolution of dilatancy and permeability in rock salt during hydrostatic compaction and triaxial deformation. Journal of Geophysical Research: Solid Earth, 106(B3), 4061–4078. https://doi.org/10.1029/2000JB900381.

Reedy, C. L., & Reedy, P. B. (2022). High-resolution micro-CT with 3D image analysis for porosity characterization of historic bricks. Heritage Science, 10, 83. https://doi.org/10.1186/s40494-022-00723-4

Roveri, M., Lugli, S., Manzi, V., & Schreiber, B. C. (2008). The Messinian salinity crisis: A sequence-stratigraphic approach. GeoActa, Special Publication, 1, 117-138.

Saxena, N., Hofmann, R., Alpak, F. O., Berg, S., Dietderich, J., Aber, U., & Hows, A. (2019a). References and benchmarks for pore-scale flow simulated using micro-CT images of porous media and digital rocks. Advances in Water Resources, 109, 211-235.

Saxena, N., Hows, A., Hofmann, R., Alpak, F. O., Freeman, J., Hunter, S., & Appel, M. (2019b). Imaging and computational considerations for image computed permeability: Operating envelope of Digital Rock Physics. Transport in Porous Media, 129, 403-412.

Schreiber, B. C., & Hsü, K. J. (1980). Evaporites. In G. D. Hobson (Ed.), Developments in petroleum geology (Vol. 2, pp. 87–138). Applied Science Publishers.

Schreiber, B. C., & Lugli, S. (2019). Messinian evaporites. In R. Ferretti (Ed.), Encyclopedia of ocean sciences (3rd ed., pp. 598–608). Academic Press.

Son, E., Sim, Y., & Kim, K. Y. (2024). Hydrogen diffusion through rock salt: Experimental measurements and numerical simulation. Journal of Rock Mechanics and Geotechnical Engineering, 16(10), 4108–4119.

Song, R., Song, Y., Liu, J., & Yang, C. (2024). Multiscale experimental and numerical study on hydrogen diffusivity in salt rocks and interlayers of salt cavern hydrogen storage. International Journal of Hydrogen Energy, 79, 319–334. https://doi.org/10.1016/j.ijhydene.2024.07.037

Speranza, G., Viti, C., Ferrini, V., Mazzoli, C., & Lugli, S. (2019). Estimation of the physical, petrophysical and mineralogical properties of Messinian salt rocks, Sicily: Implications for multidisciplinary applications. Marine and Petroleum Geology, 110, 104038. https://doi.org/10.1016/j.marpetgeo.2019.104038

Stormont, J. C. (1997). In situ gas permeability measurements to delineate damage in rock salt. International Journal of Rock Mechanics and Mining Sciences, 34(3-4), 527-536.

Strauch, B., Zimmer, M., Zirkler, A., Hölzner, C. P., & Campana, B. (2023). Hydrogen diffusion through intact and fractured rock salt. International Journal of Hydrogen Energy, 48(51), 19449-19457.

Szatmari, P., Tibana, P., & Simões, I. A. (2021). Petrography, geochemistry and origin of South Atlantic evaporites: The Brazilian side. Marine and Petroleum Geology, 127, 104805. https://doi.org/10.1016/j.marpetgeo.2020.104805

Tackie-Otoo, B. N., & Haq, M. B. (2024). Underground hydrogen storage in salt caverns: Recent advances, modeling approaches, barriers, and future outlook. Journal of Energy Storage, 102, 114005. https://doi.org/10.1016/j.est.2024.114005

Tanikawa, W., & Shimamoto, T. (2009). Comparison of Klinkenberg-corrected gas permeability and water permeability in sedimentary rocks. International Journal of Rock Mechanics and Mining Sciences, 46(2), 229-238. https://doi.org/10.1016/j.ijrmms.2008.03.004

Talbot, C. J., Aftabi, P., & Chemia, Z. (2009). Potash in a salt mushroom at Hormoz Island, Hormoz Strait, Iran. Ore Geology Reviews, 35, 317–332. https://doi.org/10.1016/j.oregeorev.2008.11.005

Tarkowski, R. (2019). Underground hydrogen storage: Characteristics and prospects. Renewable and Sustainable Energy Reviews, 105, 86–94. https://doi.org/10.1016/j.rser.2019.01.051

Thommes, M., Kaneko, K., Neimark, A. V., Olivier, J. P., Rodriguez-Reinoso, F., Rouquerol, J., & Sing, K. S. W. (2015). Physisorption of gases, with special reference to the evaluation of surface area and pore size distribution (IUPAC Technical Report). *Pure and Applied Chemistry, 87*(9–10), 1051–1069. https://doi.org/10.1515/pac-2014-1117

Tsang, C.-F., Bernier, F., & Davies, C. (2005). Geohydromechanical processes in the excavation damaged zone in crystalline rock, rock salt, and indurated and plastic clays. International Journal of Rock Mechanics and Mining Sciences, 42(1), 109–125. https://doi.org/10.1016/j.ijrmms.2004.08.003

Urai, J. L., Spiers, C. J., Zwart, H. J., & Lister, G. S. (1986). Weakening of rock salt by water during long-term creep. Nature, 324, 554–557. https://doi.org/10.1038/324554a0

Urai, J. L., & Spiers, C. J. (2007). The effect of grain boundary water on deformation mechanisms and rheology of rocksalt during long-term deformation. In The Mechanical Behavior of Salt (Saltmech6) (pp. 149-158). Hannover, Germany.

Wang, J., Zhang, Q., Song, Z., Liu, X., & Wang, Y. (2022). Microstructural variations and damage evolvement of salt rock under cyclic loading. International Journal of Rock Mechanics and Mining Sciences, 152, 105078. https://doi.org/10.1016/j.ijrmms.2022.105078

Wardlaw, N. C. (1968). Carnallite-sylvite relationships in the Middle Devonian Prairie Evaporite Formation, Saskatchewan. GSA Bulletin, 79(10), 1273-1294. https://doi.org/10.1130/0016-7606(1968)79[1273:CRITMD]2.0.CO;2

Yoshimura, T., Kuroda, J., Lugli, S., Tamenori, Y., Ogawa, N., Jiménez-Espejo, F., Isaji, Y., Roveri, M., Manzi, V., Kawahata, H., & Ohkouchi, N. (2016). An X-ray spectroscopic perspective on Messinian evaporite from Sicily: Sedimentary fabrics, element distributions, and chemical environments of S and Mg. Geochemistry, Geophysics, Geosystems, 17(7), 2942-2960. https://doi.org/10.1002/2015GC006233

Yuan, L., Dehghanpour, H., & Najafimarghmaleki, A. (2025a). Underground hydrogen storage in salt caverns: Assessment of kinetic geochemical reactions. Energy & Fuels, 39(31), 15133–15149. https://doi.org/10.1021/acs.energyfuels.5c00642

Yuan, L., Najafimarghmaleki, A., & Dehghanpour, H. (2025b). Hydrogen storage in impure salt formations: Batch experiments on Lotsberg salt. Energy & Fuels, 39(6), 3140-3156. https://doi.org/10.1021/acs.energyfuels.4c04506

Supplementary Materials

This document provides supplementary data, figures and tables supporting the main text. Sections are numbered S1- S10 and cross-referenced from the corresponding main-text sections.

S1. Micro-CT segmentation parameters

Table S1 summarises the grey-value thresholds and phase-assignment criteria adopted for each of the two micro-CT volumes. Because mineralogical composition and histogram morphology differ among samples, segmentation schemes were tailored individually. For RS1, a single pore-threshold range captures the air and brine phases against a uniform halite matrix. For KS5_batch, the pore-threshold upper limit was defined statistically as μ-3σ of the matrix grey-value distribution (28500 GV), corresponding to the lower 0.15th percentile of the matrix population, thereby minimising false-positive pore assignments from partial-volume effects at grain boundaries.

Parameter	RS1 (lab μCT)	KS5_batch (synchrotron)
Source / Instrument	Zeiss Xradia 520 Versa	DLS beamline I13-2
Voxel size (μm)	30.98	22.0
Bit depth	16-bit unsigned	16-bit unsigned
Total GV range	0-65528	0-65528
Segmentation thresholds		
Pore segmentation range (GV)	**18000-28000**	**< 28500**
Histogram peak: pores/brine	GV ~ 21 000	No discrete peak (unimodal matrix)
Threshold selection criterion	Valley between background and halite peaks; iterative visual assessment on ortho slice overlays	μ − 3σ of matrix GV distribution (0.15th percentile)
Background + air (GV)	0~11000	Included in pore range (< 28500)
Brine + partial-volume (GV)	~11000-18000	Included in pore range (< 28500)
Matrix (GV)	Halite: ~35000-55000	Kainite: ~28500-45000 Halite: ~4500-60000
Histogram peak: matrix	GV ~ 39000 (halite)	Single composite peak (kainite + halite; ρ ~ 2.13-2.16 g cm⁻³)
Dense accessory phases (GV)	Anhydrite: ~55000-65528	Carnallite/anhydrite: > 60000
Histogram peak: dense phases	GV ~ 64000	Minor shoulder at GV > 60000
Object size thresholds		
Minimum object size retained	8 voxels (~ 2.38×10^5 μm³)	8 voxels (~ 8.53×10^4 μm³)
Visualisation filter (figures only)	100 voxels (~ 2.97×10^6 μm³)	—
φ_CT	2.13%	0.057% (Avizo) / 0.106% (stereological)

Table S1. Grey-value segmentation thresholds for micro-CT volumes. GV = grey value (16-bit unsigned). PVE = partial-volume effect. — = not applicable. For RS1, the pore segmentation range (18 000-28 000 GV) captures both air-filled and brine-filled porosity indiscriminately; the grey-value histogram exhibits no resolvable minimum separating the two fluid populations (see Fig. S4). For KS5_batch, the pore-threshold upper limit (28 500 GV) was defined statistically as μ − 3σ of the matrix grey-value distribution, corresponding to the lower 0.15th percentile, minimising false-positive pore assignments from partial-volume effects at grain boundaries. The kainite and halite matrix phases form a single composite histogram peak owing to their near-identical densities (ρ_kainite = 2.13 g cm⁻³; ρ_halite = 2.16 g cm⁻³). The visualisation filter (100 voxels) applied to RS1 was used exclusively for publication figures; all quantitative measurements were derived from the unfiltered segmentation (≥ 8 voxels).

S2. Label Analysis shape-descriptor statistics

Table S2 presents the full shape-descriptor statistics from the Avizo Label Analysis for each sample, filtered to objects of eight or more voxels. Anisotropy, elongation and flatness are computed from the eigenvalues of the inertia tensor of each labelled object.

Descriptor	RS1 (n = 1,989)	KS5-B (n = 933)
Mean equiv. diameter (µm)	187.7	81.2
Median equiv. diameter (µm)	151.3	70.2
Mean anisotropy	0.855	0.849
Mean elongation	0.372	—
Mean flatness	0.326	0.410
High-anisotropy objects (>0.7)	82.0%	88.3%
Largest object (% pore vol.)	78.8%	8.2%
Border-touching objects	9.2%	5.7%

Table S2. Shape-descriptor statistics (objects ≥ 8 voxels). Referenced in Section 3 (Results).

S3. CT-MIP scale-bridging analysis

The ratio φ_CT/φ_MIP quantifies the fraction of total connected porosity resolved by micro-CT imaging. For RS1, the ratio is 0.53, indicating that approximately half of the pore volume consists of openings wider than 31 µm. For KS5-B, the ratio drops to 0.09, confirming that more than 90% of the pore volume in the kainite-halite assemblage is sub-resolution, even at synchrotron resolution (22 µm). These ratios underscore the complementarity of the two techniques and demonstrate that reliance on micro-CT alone would severely underestimate the total pore volume of these evaporitic lithologies.

Figure S1 illustrates the detection ranges of the two characterisation techniques employed in this study and locates the modal pore diameters and CT-derived porosity values of each sample within these ranges. Figure S2 presents the detailed MIP cumulative porosity curve, pore-size distribution and CT-detectability partition for sample RS1.

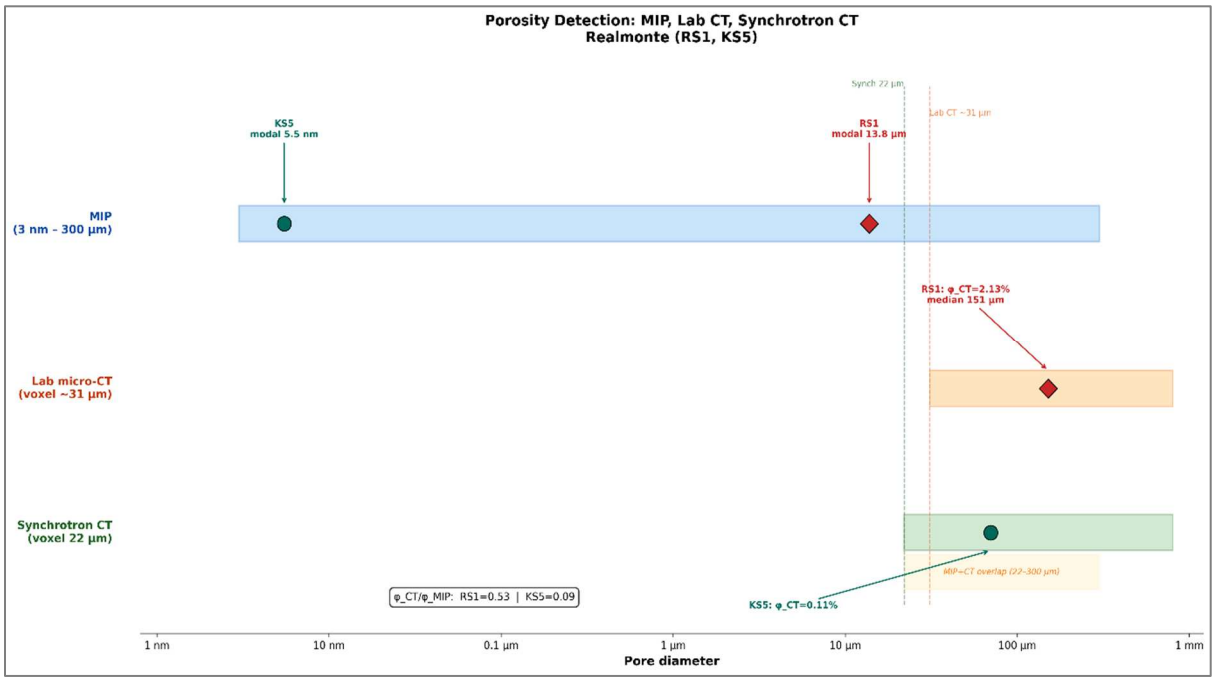

Figure S1. Porosity detection ranges of the three characterisation techniques employed in this study. Horizontal bars indicate the pore-diameter window accessible to each method: mercury intrusion porosimetry (MIP, 3 nm – 300 µm), laboratory micro-CT (voxel size 31–34 µm) and synchrotron micro-CT (voxel size 22 µm). Symbols mark the modal MIP pore diameter and CT-derived median equivalent diameter for each sample. The φ_CT/φ_MIP ratios (0.53, 0.50, 0.09) quantify the fraction of total porosity resolved by CT imaging. The shaded area denotes the overlap zone where both MIP and CT provide complementary constraints. Referenced in Section 4.1 (Discussion).

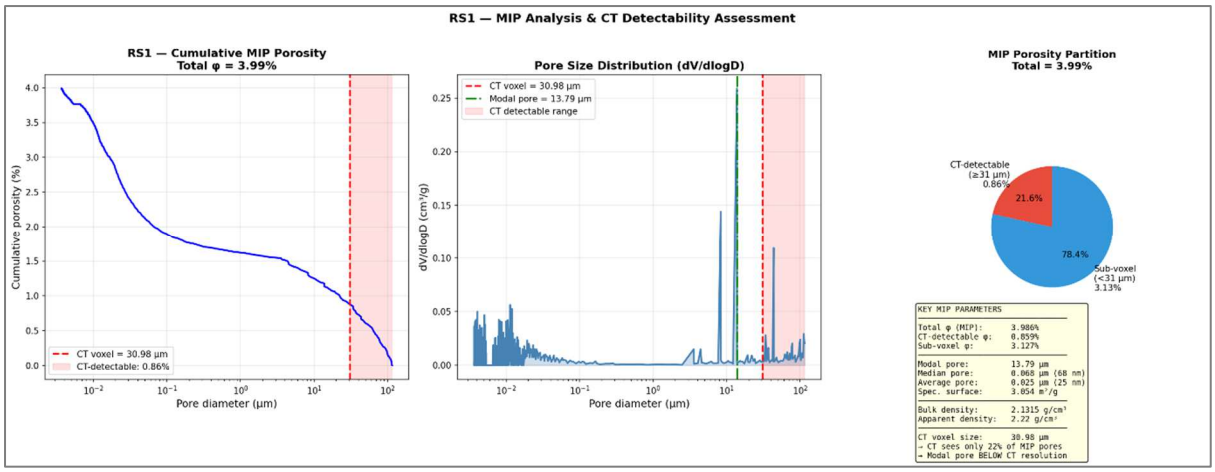

Figure S2. MIP analysis and CT detectability assessment for sample RS1. Left: cumulative porosity curve (φ_MIP = 3.99%). Centre: pore-size distribution (dV/dlogD) with modal pore diameter at 13.79 µm; the CT voxel size (30.98 µm, red dashed line) separates the CT-detectable (pink shading) from the sub-voxel fraction. Right: porosity partition showing that 78.4% of the MIP-measured pore volume resides below CT resolution. Referenced in Section 3 (Results).

S4. Synchrotron micro-CT acquisition and phase segmentation (KS5)

Sample KS5_batch was imaged at the Diamond Light Source (UK) on beamline I13-2, using a parallel monochromatic beam at 105 kV, 172 µA, with a 0.5 mm Cu filter and 3 142 projections over 180° rotation. The reconstructed volume comprises 499 slices of 500 × 500 pixels at a voxel size of 22 µm (field of view 11.0 × 11.0 × 11.0 mm). The acquisition quality was assessed as excellent (SNR=16:1, no beam hardening detected, slice-to-slice consistency σ mean) = 5.3 GV, <0.1%).
Phase segmentation was performed on the 16-bit grey-value histogram. The dominant peak corresponds to the kainite + halite matrix (density 2.13-2.16 g cm^{-3}), which forms a single composite population owing to the near-identical densities of the two mineral phases. Pores and fractures were segmented at GV < 28500, a threshold defined statistically as µ − 3σ of the matrix grey-value distribution (see Table S1). A minor dense phase (GV > 60000) was attributed to anhydrite and silicate inclusions. The resulting CT-derived porosity is 0.057% (Avizo label analysis, 933 objects ≥ 8 voxels), validated independently by stereological point-counting on 30 distributed cross-sections (φ=0.106%) and by three-dimensional connected-component analysis on a representative sub-volume (φ=0.069%) (see Section 3.3.3 for interpretation).

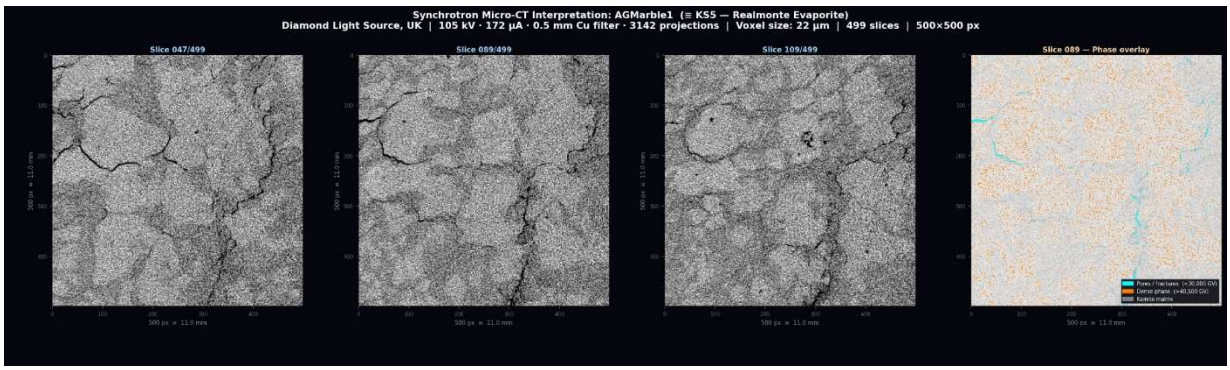

Figure S3a. Synchrotron micro-CT greyscale slices (047, 089, 109/499) and mineral phase overlay of sample KS5_batch. Acquisition: Diamond Light Source, 105 kV, 22 µm voxel, 499 slices. Phase segmentation: cyan = pores/fractures (<30000 GV), orange = dense phase (>40500 GV), white = kainite-halite matrix.

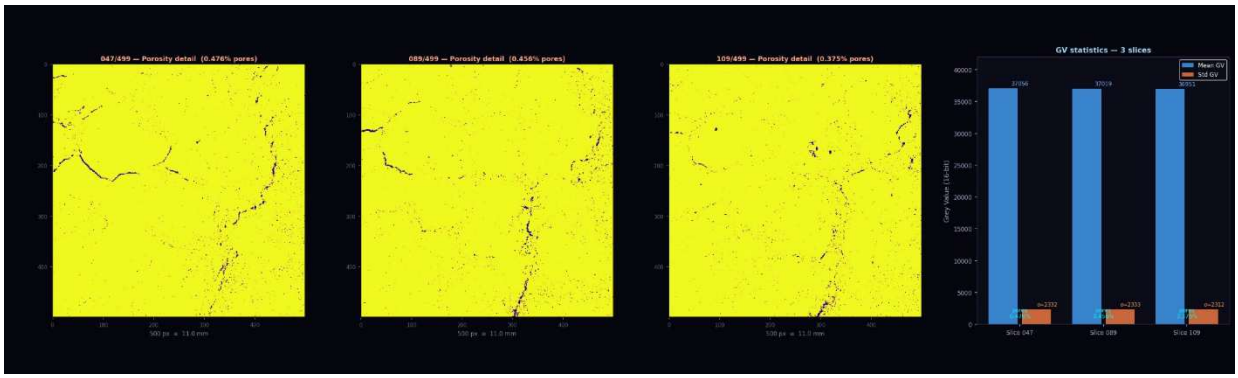

Figure S3b. Porosity detail maps (segmented at <30000 GV) for three representative slices, showing the spatial distribution and progressive decrease of CT-visible porosity with depth (0.476% → 0.375%). The GV statistics bar chart confirms consistent mean grey values (~37000 GV) across slices.

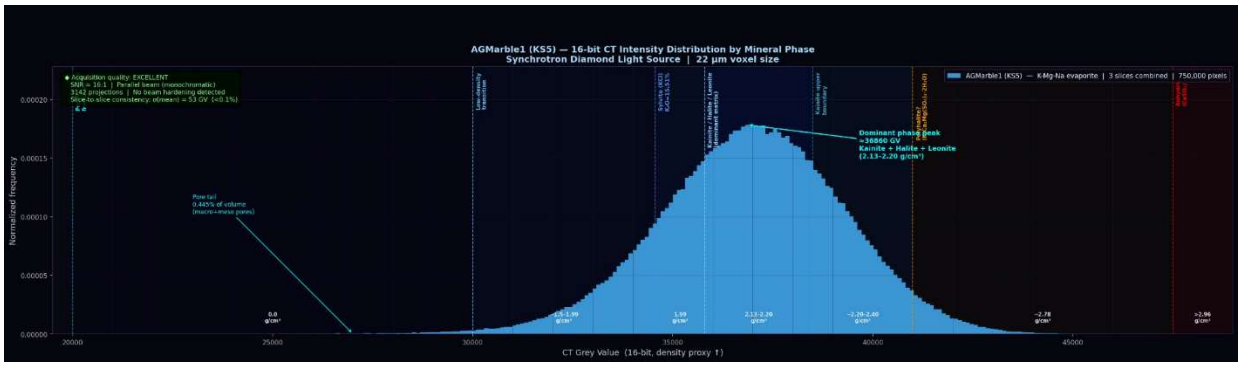

Figure S3c. 16-bit CT intensity distribution by mineral phase for sample KS5_batch (3 slices combined, 750000 pixels). The dominant peak at ~36800 GV corresponds to the kainite + halite + leonite matrix. The pore tail (<30000 GV) accounts for 0.44% of the volume. Density calibration markers are indicated along the x-axis. Referenced in Section 3 (Results).

S5. Grey-value distribution and fluid-phase discrimination limitations in sample RS1

The grey-value distribution of the RS1 masked volume was examined in detail to evaluate whether air-filled and brine-filled pore populations could be discriminated on the basis of X-ray attenuation contrast. The full histogram (Fig. S4a) displays four identifiable populations corresponding to background and air (GV~ 0), an intermediate-density pore and brine population (GV~21000), the halite matrix (GV~39000), and anhydrite plus dense accessory phases (GV~64000). The pore segmentation was performed using an Interactive Thresholding range of 18000-28000 GV, selected to capture the full intermediate-attenuation population between the background and the halite peak (Saxena et al., 2019a-b; Reedy et al., 2022).

Inspection of the 5000-35000 GV range (Fig. S4b) reveals a continuous distribution with no resolvable local minimum between the air-filled pore tail and the brine-filled pore shoulder. This absence of bimodal separation reflects three compounding effects: (i) partial-volume averaging, whereby voxels at pore-matrix interfaces contain sub-voxel mixtures of solid, air and brine producing intermediate grey values; (ii) the presence of thin brine films at grain boundaries (Urai et al., 1986; Desbois et al., 2012) that occupy a fraction of the voxel volume without forming discrete resolvable peaks; and (iii) the limited attenuation contrast between air and NaCl-saturated brine at the polychromatic X-ray energies of the Zeiss Xradia 520 Versa source. Differential imaging approaches

using high-salinity contrast brines (e.g. Lin et al., 2016) or higher-resolution synchrotron imaging would be required to achieve a quantitative fluid-phase separation. Consequently, the CT-derived porosity (φ_CT = 2.13%) reported for RS1 represents total porosity, encompassing both air-filled and brine-filled pore space, and should be interpreted accordingly when compared with MIP-derived values (see Section 4.1).

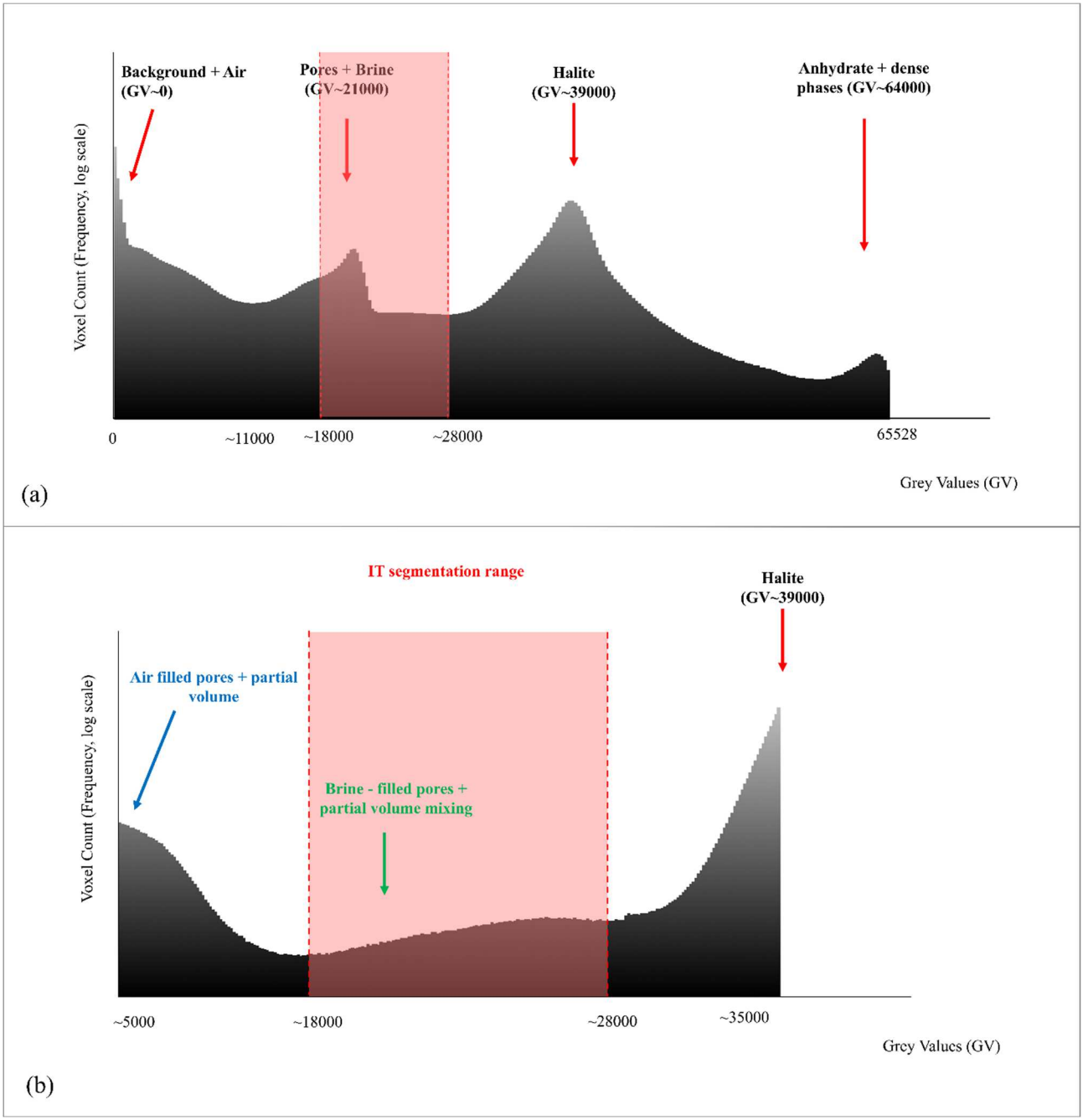

Fig. S4 Grey-value histogram of sample RS1 (masked volume, 318 slices, voxel size 30.98 µm). Vertical axis in logarithmic scale. (a) Full histogram (0-65528 GV) showing four principal populations: background and air-filled pores (GV~0), pores and brine (GV~21000), halite matrix (GV~39000), and anhydrite plus dense accessory phases (GV~64000). The pink-shaded area marks the Interactive Thresholding (IT) segmentation range (18000-28000 GV) applied for pore-space extraction. (b) Detail of the 5000-35000 GV range, showing the continuous, monotonically varying distribution between the air-filled pore population and the halite matrix peak. No discrete local minimum separates the air-filled and brine-filled pore populations, precluding fluid-phase discrimination by single-scan grey-value thresholding at the current voxel resolution.

S6. Spatial distribution of segmented porosity in sample RS1

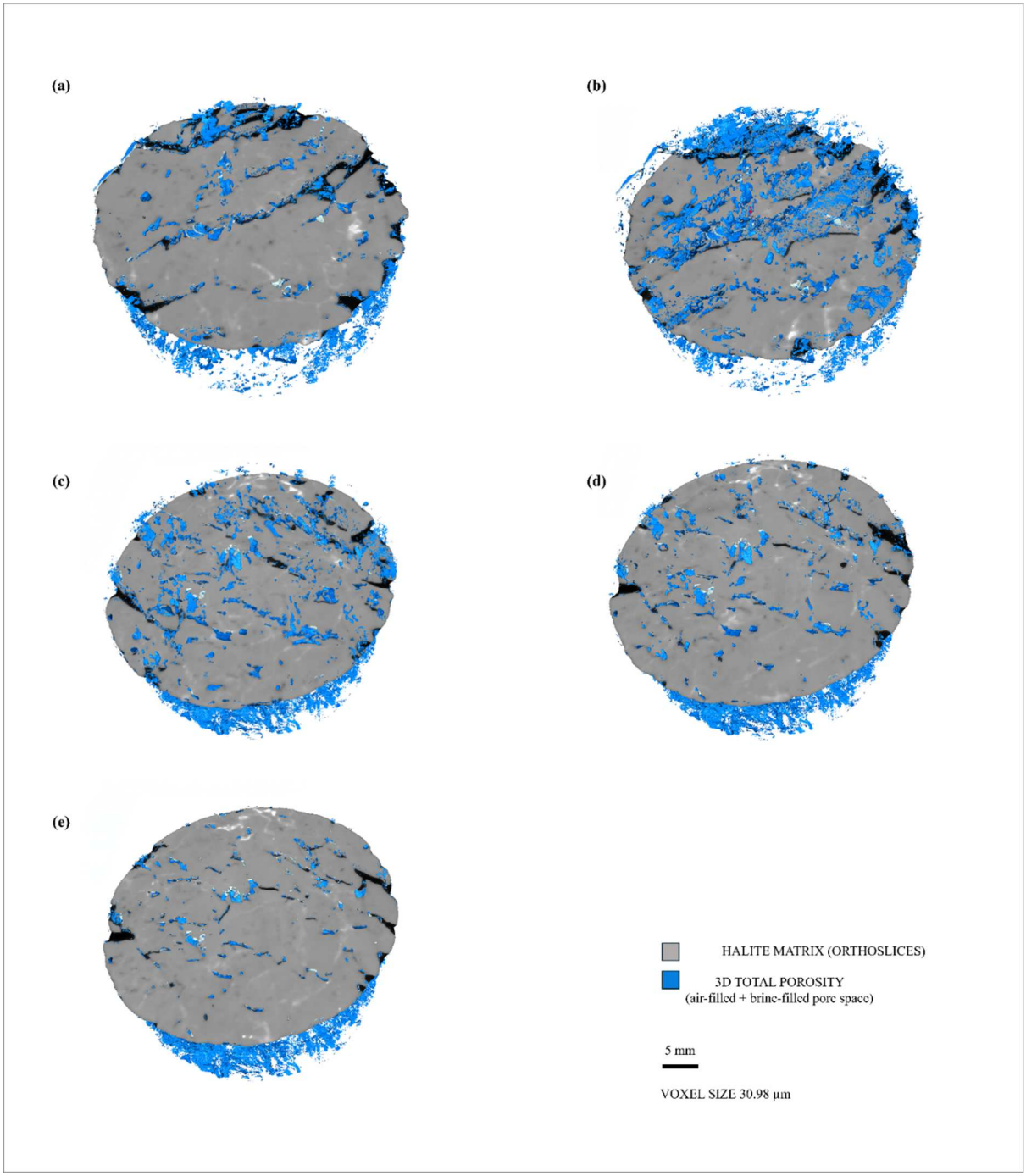

Figure S5. Spatial distribution of segmented porosity across the full RS1 µCT volume (318 slices; voxel size 30.98 µm). Each panel shows the complete 3D segmented pore network (blue; unfiltered, all objects ≥ 8 voxels) intersected by a single ortho slice (greyscale) at different positions along the vertical (Z) axis: (a) slice 23, (b) slice 77, (c) slice 270, (d) slice 293, (e) slice 307. The greyscale background displays the original reconstructed attenuation data, where dark features correspond to low-density domains (pores, fractures and grain-boundary fluids). The spatial correspondence between blue segmented objects and dark features in the ortho slices confirms the fidelity of the Interactive Thresholding segmentation (IT range 18000-28000 GV). Porosity is heterogeneously distributed: sub-planar fractures concentrated along grain boundaries are more prominent in the upper and lower portions of the sample, while the central region exhibits comparatively fewer CT-resolvable features. Blue phase represents total CT-derived porosity (air-filled + brine-filled pore space).

S7. Supplementary petrography

S7.1. Pre-exposure thin sections

Figures S6-S15 present transmitted-light and SEM-BSE micrographs of samples not illustrated in the main text, documenting the full range of textural and mineralogical features observed in the Realmonte evaporite suite prior to hydrogen exposure. These include: euhedral anhydrite inclusions (RS4, RS14), fibro-radiated sulphate aggregates (RS14), two- and three-phase fluid inclusions (RS10), clay-hosted anhydrite growth (RS14), carnallite and/or leonite within kainite (KS5), fluid inclusions in halite (KS3), clay fraction associated with carnallite (KS5), and celestine microcrystals in anhydrite (BSE images).

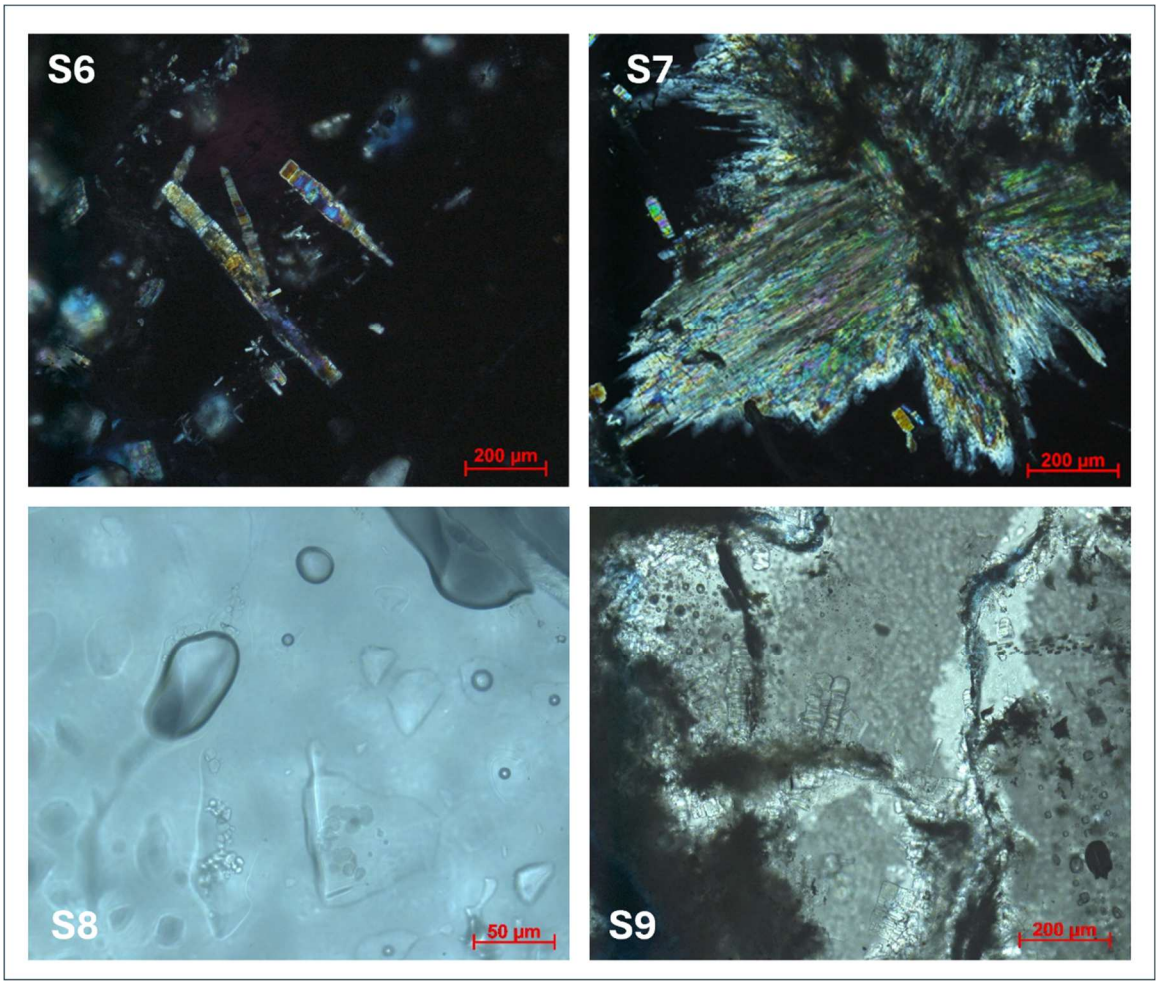

Figs S6-S9. S6: RS4, elongated euhedral minerals, crossed polars. S7: RS14, fibro-radiated sulphate aggregate. S8: RS10, two- and three-phase fluid inclusions. S9: RS14, clay material with anhydrite growth. Referenced in Section 3 (Results).

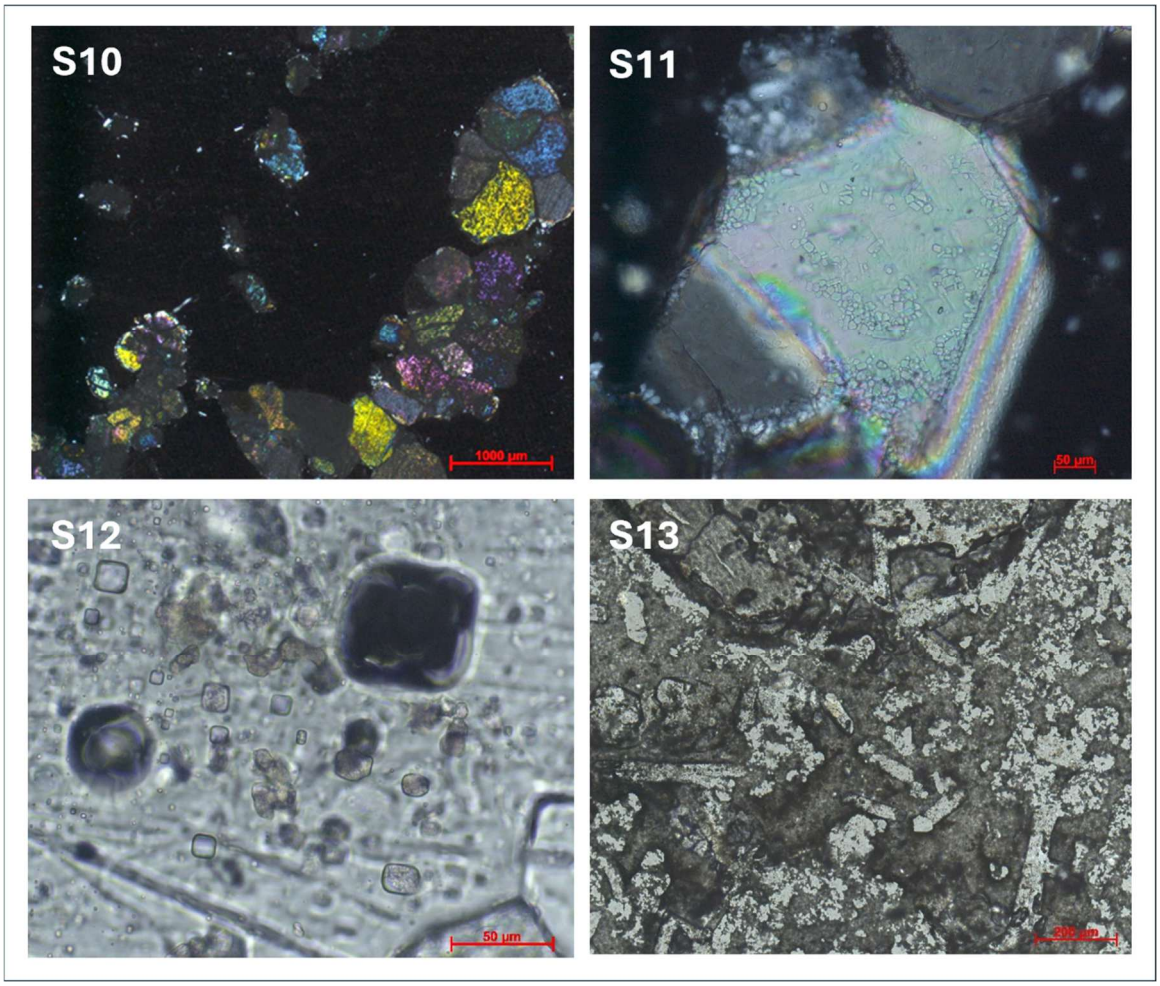

Figs S10-S13. S10: KS3, general texture. S11: KS5, carnallite/leonite within kainite. S12: KS3, fluid inclusions in halite. S13: KS5, clay fraction with carnallite. Referenced in Section 3 (Results).

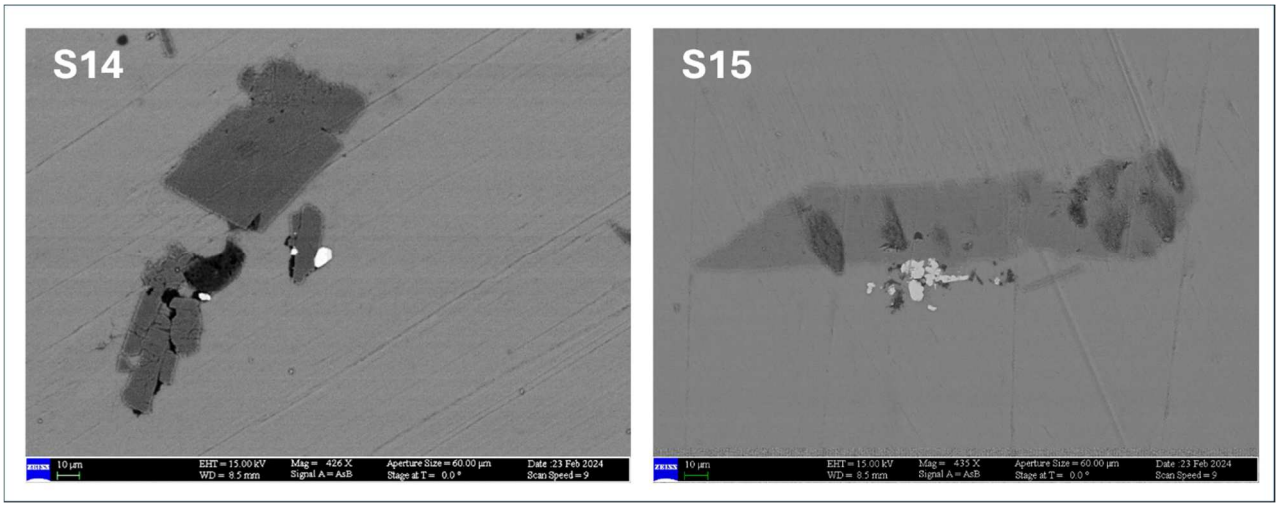

Figs S14-S15. S14. Sample RS1. BSE image showing euhedral to subeuhedral anhydrite crystals (dark grey) with celestine microcrystals (light gray). S15. Sample RS10. BSE image showing a euhedral anhydrite crystal (dark grey) with celestine microcrystals (light gray). Referenced in Section 3 (Results).

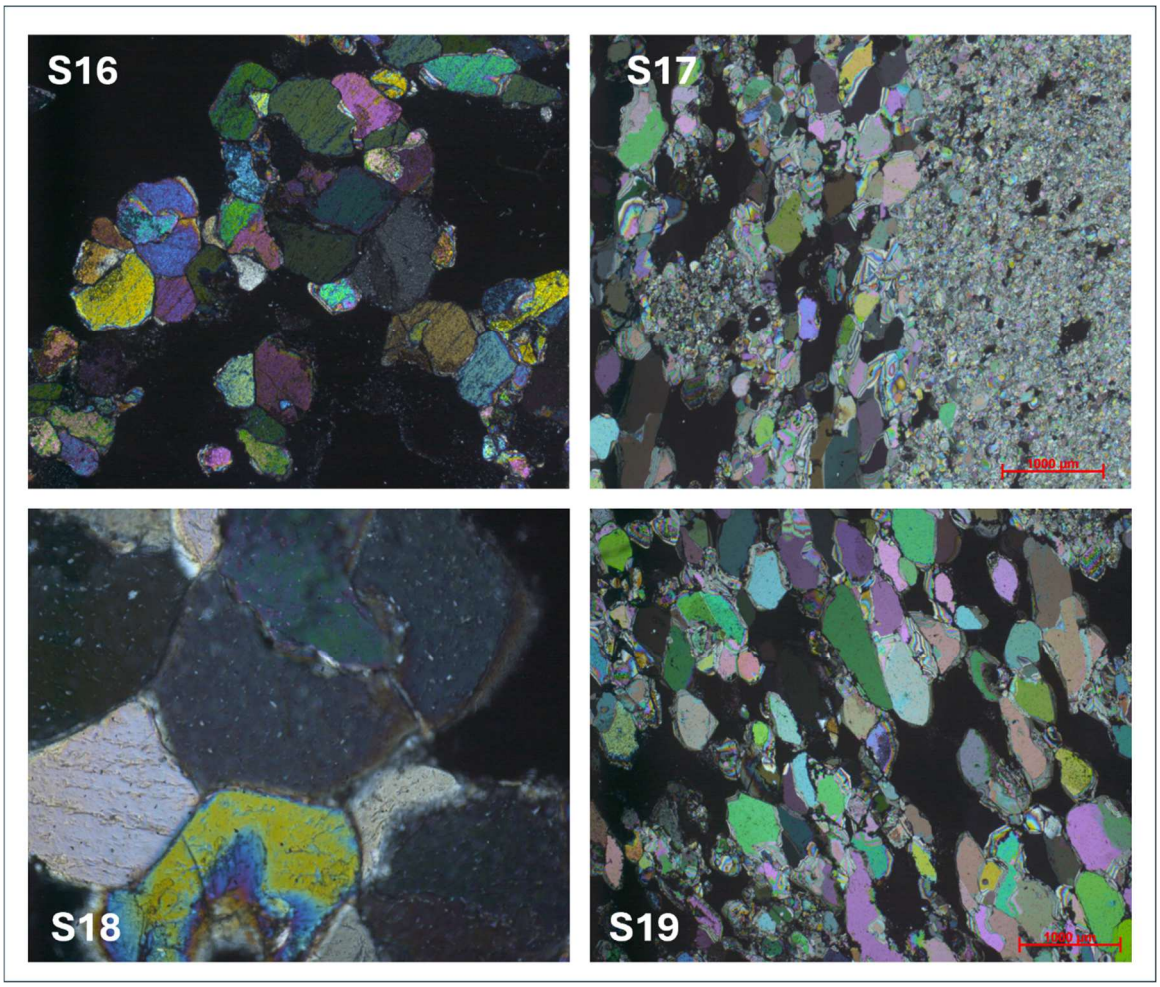

Figs. S16-S19**.** S16: KS3, cluster of euhedral to sub-euhedral kainite macrocrystals (~300-500 µm) displaying vivid first- and second-order interference colours characteristic of the monoclinic kainite structure (Borisov et al., 2022). Isotropic (black) intergranular domains correspond to anhedral halite infill. S17:KS2, overview showing the characteristic layered texture with a macrocrystalline kainite domain (left; crystals ~300-400 µm with vivid interference colours) transitioning into a fine-grained microcrystalline domain (right; aggregates ~60-100 µm). Halite occupies intergranular positions as isotropic (black) anhedral infill. Visual estimation of the mineral proportions indicates approximately 60-70% kainite and 20-25% halite by area, broadly consistent with the XRPD-derived composition of KS5 (65.2% kainite, 28.8% halite). S18: KS3, detail of kainite macrocrystals exhibiting complex twinning. Crystal sizes reach ~500 µm. Dark interstitial material at grain boundaries could be consistent with organically enriched hypersaline brine. S19: KS2, overview of the macrocrystalline domain showing elongated, sub-euhedral to euhedral kainite crystals (~200–400 µm) with a preferred orientation, separated by isotropic halite and dark intergranular fluids.

S7.2. Post-exposure thin sections

Figures S20-S22 present micrographs of samples after hydrogen exposure (10 MPa, 120 h). No new mineral phases were observed. Textural features include calcium sulphate fibrated aggregates, macro- and microcrystals with equidimensional to anhedral habit (KS5), and persistent clay material at halite-kainite boundaries.

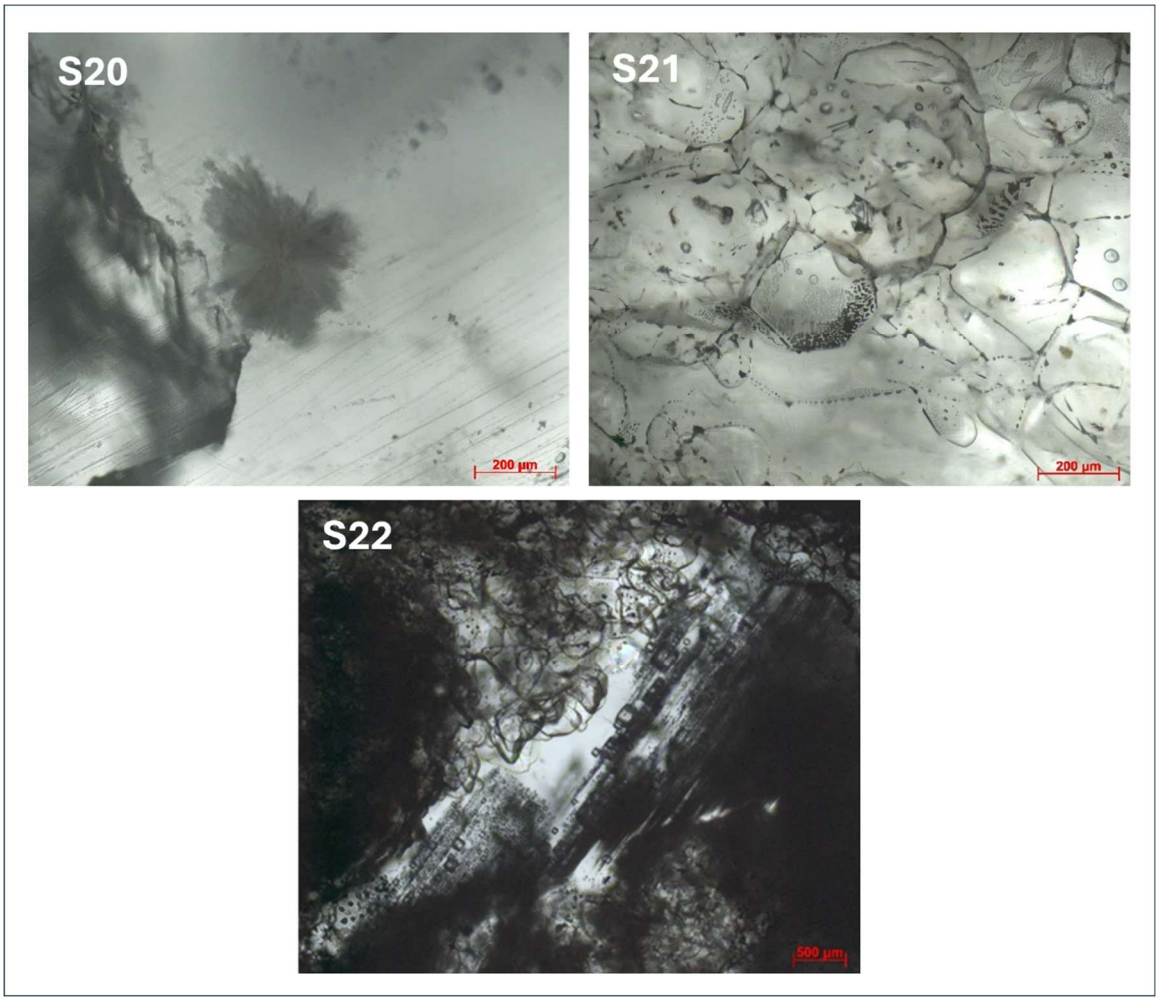

Figures S20-S22. Transmitted-light micrographs of post-exposure samples. S20: calcium sulphate fibrated aggregate, S21: KS5, equidimensional to anhedral microcrystals. S22: clay material at halite-kainite boundaries. Referenced in Section 3 (Results).

S8. XRPD diffractograms

S8.1. Pre-exposure diffractograms

Figures S23-S27 present the X-ray powder diffraction patterns of all samples prior to hydrogen exposure.

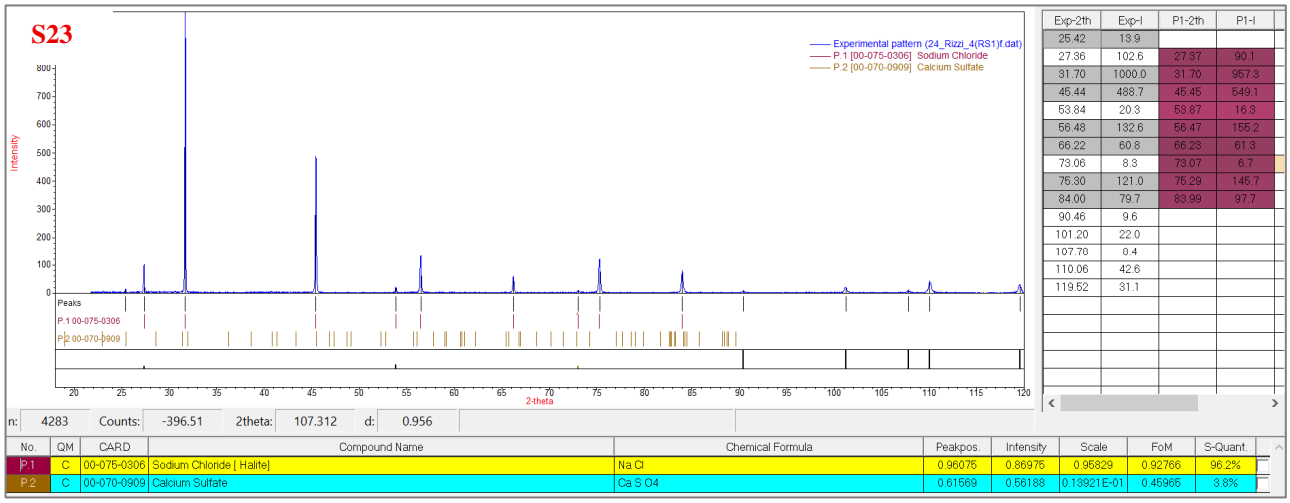

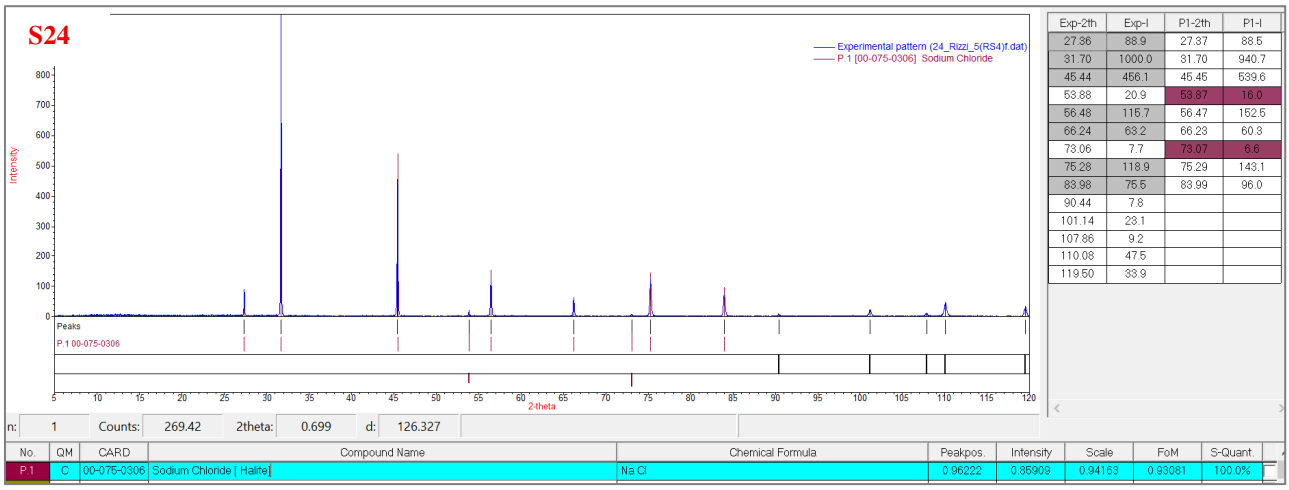

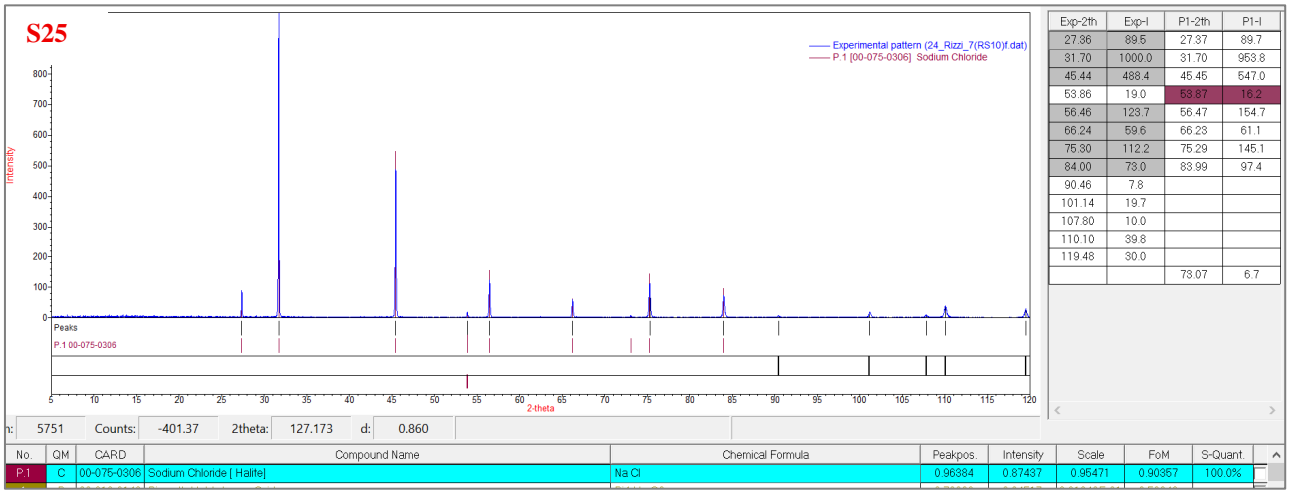

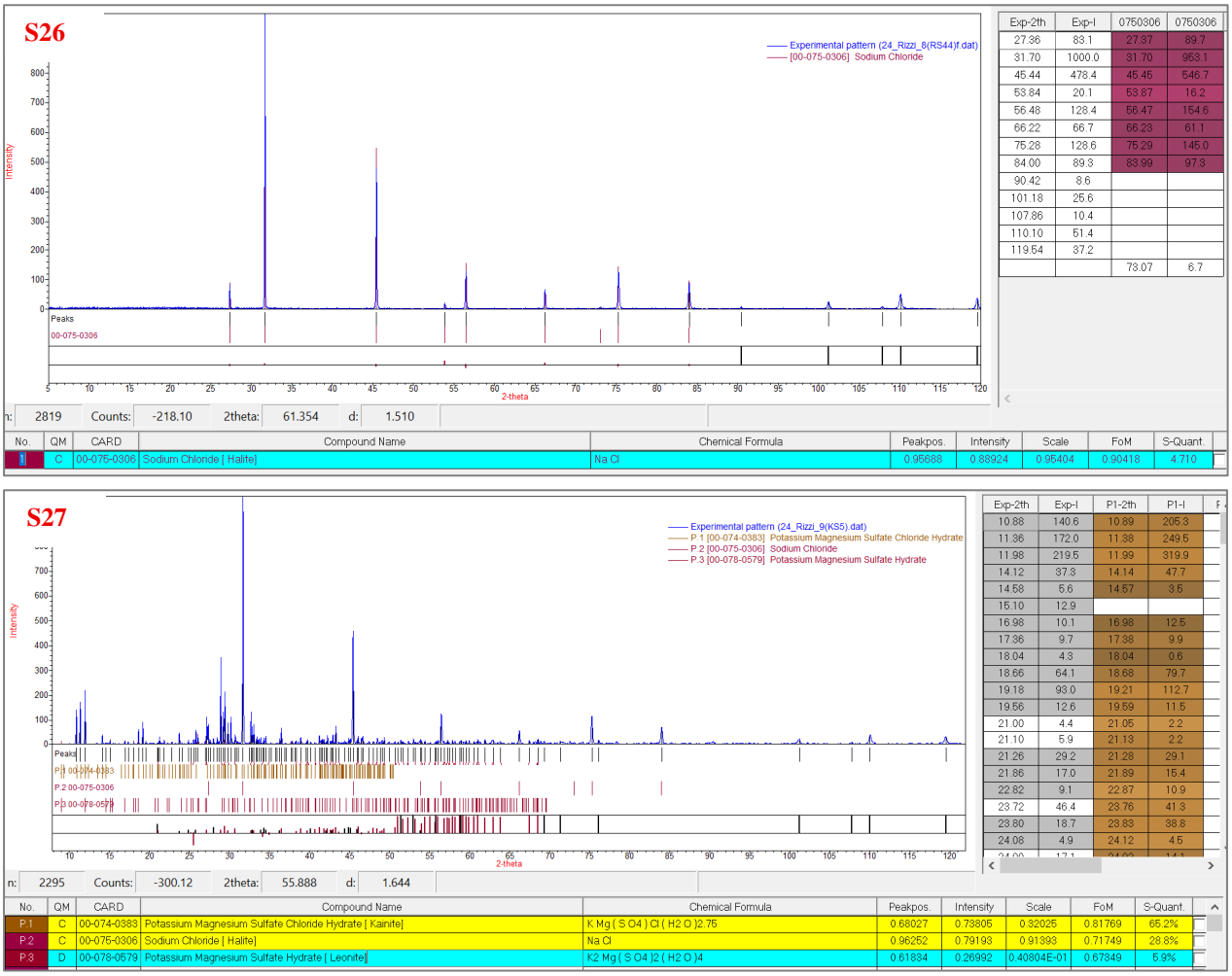

Figures S23-S27. Qualitative and semi-quantitative results by QUALX2.0 software. Vertical tick marks indicate the 2θ positions of the experimental peaks (black). The reference peak positions of the phases identified by qualitative analysis are shown below, each phase on a separate line. Details are provided in Section 2 (Materials and Methods) and Section 3 (Results). S23: RS1 (NaCl: 96.2%, CaSO4: 3.8%). S24: RS4 (halite 100%). S25: RS10 (halite 100%). S26: RS14 (halite 100%). S27: KS5 (kainite: 65.2%, halite: 28.8%, leonite: 5.9%).

S8.2. Post-exposure diffractograms

Figures S28-S30 present the XRPD patterns of all samples after hydrogen exposure. No new peaks appeared and all pre-existing phases were retained, confirming the mineralogical stability of both halite and kainite under hydrogen at storage-relevant pressures.

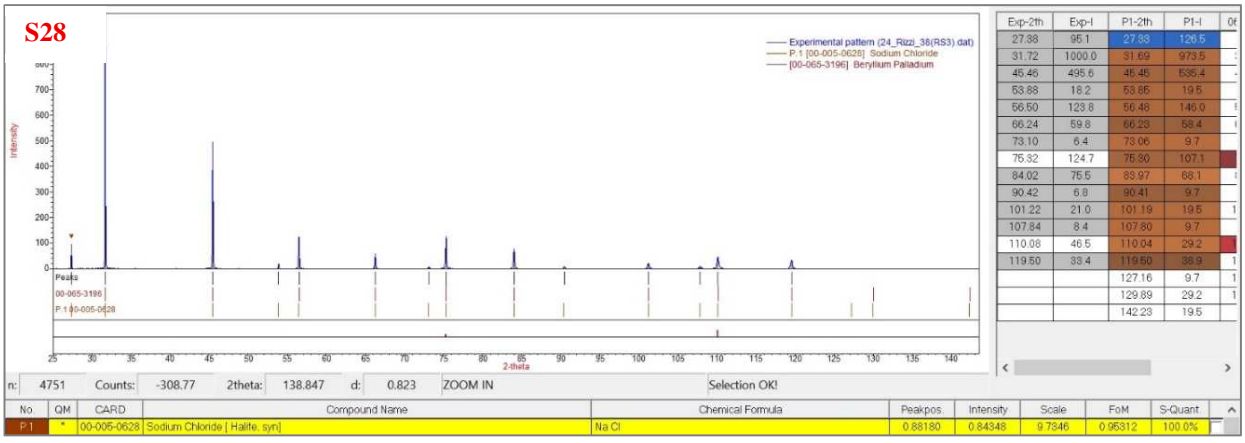

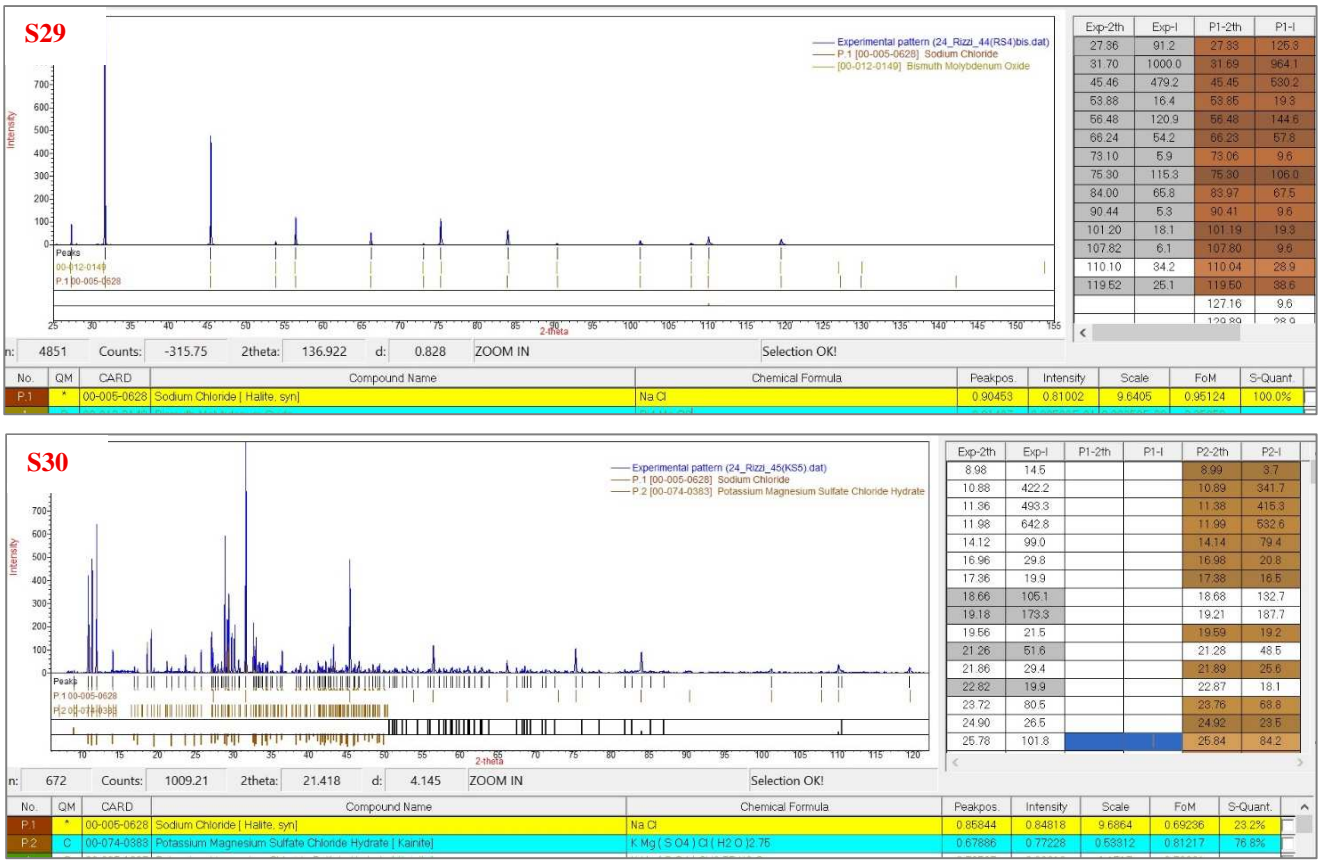

Figures S28-S30. XRPD patterns of post-exposure samples. Phase identification is consistent with the pre-exposure patterns. Details are provided in Section 3 (Results). S28: RS3_batch. S29: RS4_batch. NaCl. 100%. S30: KS5_batch (kainite: 76.8%, halite: 23.2%).

S9. SEM-EDS quantitative mineral chemistry

Table S3 reports the electron microprobe (SEM-EDS) analyses of individual mineral phases identified in the Realmonte samples. Structural formulae are calculated on the basis of the appropriate number of oxygens for each mineral species. These data confirm the stoichiometric purity of anhydrite ($CaSO_4$), celestine ($SrSO_4$), polyhalite ($K_2Ca_2Mg(SO_4)_4 \cdot 2H_2O$), kainite ($KMg(SO_4)Cl \cdot 3H_2O$).

	Anhydrite			Celestine		Polyhalite	Kainite	Leonite
Sample	**RS1**	**RS14**	**RS10**	**RS1**	**RS10**	**KS5**		
FeO_{tot}		0.01						
MgO	0.11	0.21				6.79	16.21	10.89
CaO	40.64	39.98	41.75	0.85		18.61		0.11
Na_2O	0.05	0.10						
K_2O	0.15	0.01				15.51	18.93	25.73
SrO				55.13	56.75			
SO_3	58.17	58.79	58.59	43.17	42.99	53.49	31.90	44.09
Cl							14.27	
Tot.	99.12	99.09	100.34	99.15	99.74	94.40	81.31	80.82
(F.Cl)/O	0.00	0.00	0.00	0.00	0.00	0.00	3.22	0.00
Tot.	99.12	99.09	100.34	99.15	99.74	94.40	78.09	80.82
O by formula	4					16	5	8
Fe^{2+}	0.00	0.00	0.00	0.00	0.00	0.00	0.00	0.00
Mg	0.00	0.01	0.00	0.00	0.00	1.01	0.91	0.98
Ca	0.99	0.97	1.01	0.03	0.00	1.98	0.00	0.01
Na	0.00	0.00	0.00	0.00	0.00	0.00	0.00	0.00
K	0.00	0.00	0.00	0.00	0.00	1.97	1.01	1.99
Sr	0.00	0.00	0.00	0.98	1.01	0.00	0.00	0.00
S	1.00	1.01	1.00	1.00	1.00	4.01	0.91	2.00
Cl	0.00	0.00	0.00	0.00	0.00	0.00	0.91	0.00

Table S3. SEM-EDS oxide weight percentages and structural formulae for mineral phases in Realmonte samples. Referenced in Section 3.

S10. PHREEQC thermodynamic modelling

Table S5 summarises the input parameters for the PHREEQC equilibrium simulations (static and time-dependent) used to assess the thermodynamic stability of halite and kainite under hydrogen-saturated brine conditions representative of a salt cavern environment. Table S6 reports the output equilibrium concentrations and saturation indices for relevant mineral phases.

Parameter	Value
Temperature	90 °C
Pressure	8.9 MPa
Brine composition (mol/kgw)	$Na^+ \approx 6$; $Cl^- \approx 6$; [K^+, Mg^{2+}, SO_4^{2-}] variable depending on simulation
Halite	Present (equilibrium phase)
Kainite	Present in Simulations 2 and 3
H_2 gas	Partial pressure ~133 atm; 70% molar fraction
Simulation type	Sim 1 & 2: Static equilibriumSim 3: Kinetic run (30 days)
Kainite rate constant	1×10^{-12} mol/kgw/s (Simulation 3 only)

Parameter	Value
Temperature	90 °C
Pressure	8.9 MPa
Halite Saturation Index	−0.0044
pH	6.30
Eh	−0.371 V
H2 in solution	$2.07\cdot10^{-7}$ mol/kgw

Tables S4-S5. PHREEQC thermodynamic modelling parameters and outputs. S5: input parameters (temperature, pressure, brine composition, gas phase). S6: equilibrium output values for static and time-dependent simulations. Referenced in Section 3 (Results) and Section 4.2 (Discussion).